Microfluidics for Bacterial Chemotaxis
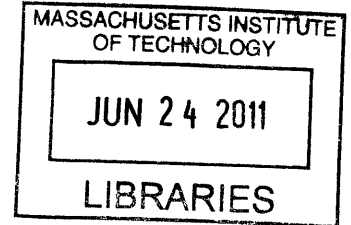
by

Tanvir Ahmed

B.Sc. Civil Engineering

Bangladesh University of Engineering and Technology, 2003

and

M.Sc. Civil and Environmental Engineering

Bangladesh University of Engineering and Technology, 2005

Submitted to the Department of Civil and Environmental Engineering

in partial fulfillment of the requirements for the degree of

Doctor of Philosophy

at the

MASSACHUSETTS INSTITUTE OF TECHNOLOGY

June 2011

Author..
Department of Civil and Environmental Engineering

April 19, 2011

Certified by..

Roman Stocker

Associate Professor of Civil and Environmental Engineering

Thesis Supervisor

Accepted by..

Heidi M. Nepf

Chair, Departmental Committee for Graduate Students

Microfluidics for Bacterial Chemotaxis

by

Tanvir Ahmed

Submitted to the Department of Civil and Environmental Engineering
on April 19, 2011, in partial fulfillment of the requirements for the degree of
Doctor of Philosophy in Civil and Environmental Engineering

ABSTRACT

Bacterial chemotaxis, a remarkable behavioral trait which allows bacteria to sense and respond to chemical gradients in the environment, has implications in a broad range of fields including but not limited to disease pathogenesis, in-situ bioremediation and marine biogeochemistry. And therefore, studying bacterial chemotaxis is of significant importance to scientists and engineers alike. Microfluidics has revolutionized the way we study the motile behavior of cells by enabling observations at high spatial and temporal resolution in carefully controlled microenvironments. This thesis aims to explore the potential of microfluidic technology in studying bacterial behavior by investigating different aspects of bacterial chemotaxis on a microfluidic platform.

We quantified population-scale transport parameters of bacteria using videomicroscopy and cell tracking in controlled chemoattractant gradients. Previously, transport parameters have been derived theoretically from single-cell swimming behavior using probabilistic models, but the mechanistic foundations of this up-scaling process have not been proven experimentally. The parameter estimates computed directly from single-cell swimming information showed good agreement with literature values providing the experimental verification of the upscaling from single cells to population-scale models.

Furthermore, we also developed a diffusion-based microfluidic device to generate steady, arbitrarily shaped chemical gradients. Steady gradients, linear or nonlinear, are often a useful model of the bacterial microenvironment to study chemotaxis in the limit of slow patch diffusion or fast motility of free swimming bacterial cells. Observed cell distribution along the gradients showed good agreement with predictions from the bacterial transport equation, providing the first quantification of chemotaxis in steady nonlinear gradients.

Also, by observing the time series of the bacterial distributions in different scaled gradients (both steady and unsteady) generated using microfluidic devices, the bacterial response was found to be invariant up to an 87-fold change in ambient chemoattractant concentration. These observations provide an explanation for the ability of bacteria to cope with a broad range of chemical concentrations and gradients in the environment, by means of a flexible sensing network that allows them to rescale their response to take maximum advantage of signals, while discounting less-informative background information.

Finally, a microfluidic lattice habitat was developed to study the fate of a chemotactic bacterial population under the pressure of predation. It was observed that the demographic and spatial

organization of the bacterial prey population depended on the predator-to-prey ratio as well as on the degree of heterogeneity of the habitat structure. These results represent a first step towards predator-prey microcosms and pave the way for future predator-prey metapopulation studies.

Thesis Supervisor: Roman Stocker
Title: Associate Professor

ACKNOWLEDGEMENTS

First and foremost, I would like to thank my thesis supervisor, Roman Stocker, for his support and guidance. His enthusiasm and dedication towards research are almost contagious and it was my absolute privilege to work with him for the past five and a half years.

I would like to thank my thesis committee members, Profs. Martin Polz, Roger Kamm and Daniel Irimia for their constructive insights throughout the committee meetings. Daniel Irimia has also been a 'microfluidics mentor' for me outside the formal committee meetings and I am grateful to him and Octavio Hurtado for arranging and conducting my training in microfabrication at the BIOMEMS Resources Center at MGH.

I would like to extend my appreciation to Justin Seymour for his guidance and help in microbiological methods as well as his friendship. In the lab, we shared many funny moments as well as stimulating scientific discussions. Tom Shimizu has been instrumental in developing my understanding of the bacterial chemotaxis system and collaboration with him was a very rewarding experience.

I thank my lab group members Mack Durham, Marcos, Hongchul Jang, Michael Barry, Mitul Luhar, Steven Smriga, Jeff Guasto, Roberto Rusconi and Maria Remirez for keeping the most friendliest atmosphere in the lab and often catering to my most untimely requests to switch the microscope reservation. Profs. Heidi Nepf and Eric Adams provided valuable inputs during group meeting presentations. The Polz, Chisholm, DeLong and Alm labs were great resources, in sharing equipments and ideas. I am thankful to Michael Cutler for keeping a close eye on me while accessing lab tools and guiding me through various safety regulations while working the lab.

I like to thank my friends at MIT, Sujan Kabir, Noreen Zaman, Naushad Hossain and Charisma Choudhury for sharing enjoyable times together.

I cherish the unconditional support of my parents, who have kept their faith in me. I am thankful to my baby daughter Nameera, who filled my life with joy and happiness for the last one and a half years. I render my heartiest gratitude to my beloved wife, Nehreen Majed for her support, and encouragement. It seems only a miracle to me that after all the support she has given me along with the effort of raising a baby, she somehow managed to do a Ph.D. herself as well.

Finally, thanks to Almighty God for giving me the strength to carry me through this intellectual journey.

TABLE OF CONTENTS

LIST OF FIGURES

LIST OF TABLES

Chapter 1

Introduction[a]

1.1 Bacterial chemotaxis and its implications

Chemotaxis is the ability of organisms to sense their chemical environment and adjust their motile behavior accordingly. Bacteria are often able to measure chemical gradients and migrate towards higher concentrations of a favorable chemical or lower concentration of an unfavorable one. An early report of such behavior is aerotaxis, discovered by Engelmann in 1881. While pursuing experiments on photosynthesis, he observed bacteria actively migrating towards regions of higher oxygen concentration generated by algal cells [2]. Bacterial chemotaxis has been the subject of increasing scientific interest in the past five decades, ever since systematic and quantitative methods of studying chemotaxis were introduced, beginning in the 1960s. On the one hand, it has received much attention as a biological sensory system that is tractable at the molecular level in genetically well-defined and manipulatable model organisms (see next section). On the other hand, its study has found far-reaching implications in a wide range of fields, as mentioned below.

In pathogenesis, many bacteria use chemotaxis to find suitable colonization sites. For example, chemotaxis can guide *Helicobacter pylori* (the primary causative agent of chronic gastric diseases) to the mucus lining of the human stomach [3], *Campylobacter jejuni* (one of the major factors in food-borne diseases) towards bile and mucin in the human gallbladder and intestinal tract [4], *Vibrio cholerae* towards the intestinal mucosa [5], pathogenic enterohemorrhagic *Escherichia coli* to epithelial cells in the human gastrointestinal tract [6], free-living *Vibrio anguillarium* from seawater to the skin of fish [7] and *Agrobacterium tumefaciens* towards plant wounds [8]. In many of these cases, chemotaxis can result in increased rates of host infection.

In the wider natural environment, chemotaxis affects the processing and cycling of elements by guiding bacteria towards and away from chemicals in diverse settings. Around plant roots, chemotaxis can guide free-living soil bacteria, for example those belonging to the Rhizobium species, to legume root hairs, favoring nitrogen fixation [9]. In the subsurface, chemotaxis can guide *Pseudomonas putida* and other species towards harmful organic compounds, favoring the bioremediation of contaminated sites [10]. In the ocean, chemotaxis allows bacteria to effectively utilize ephemeral resource hotspots, increasing the rate at which limiting elements are recycled

16

and contributing to shape trophic interactions [11-14], thereby potentially enhancing biogeochemical fluxes [15-17].
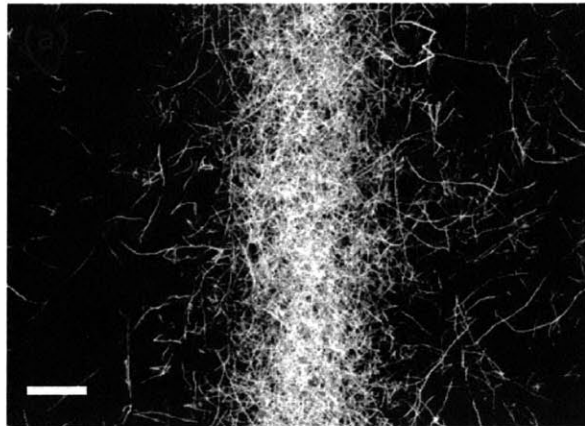
Figure 1.1 Marine bacteria *Pseudoalteromonas haloplanktis* responding to *Dunaliela tertiolecta* exudates. Using a microfluidic device, a diffusing band (vertically oriented in the figure) of *D. tertiolecta* exudates was generated while a 12.5 s movie of swimming *P.haloplanktis* cells was recorded at 30 frames/s. The collection of trajectories (white lines) obtained from the movie show intense aggregation of the bacteria in the exudate band. The scale bar indicates 300 μm. Rapid chemotaxis of marine bacteria enables them to utilize ephemeral resource hotspots in the ocean. Reproduced from Seymour *et al* 2008 with permission. Copyright 2008 American Society for Limnology and Oceanography.

Chemotaxis provides bacteria with the ability to actively navigate through a non-mixed environment (that is, in the presence of gradients) and search for an optimal growth environment. This can results in significant growth advantage [18] and can also play a crucial role in microbial population dynamics [19].

1.2 Strategies for bacterial chemotaxis

At the cellular level, bacterial chemotaxis can be understood as a biased random walk in three-dimensional space [20]. Motile cells constantly sample their local environment by propelling themselves using one or more helical flagella in a direction that is determined by chance. In an isotropic environment, this random motility allows cells to explore space much more efficiently than they would if they were to spread by Brownian motion alone. In the presence of a spatial gradient of chemoeffectors, a sensory system imposes a bias on this random behavior in a manner that yields net migration in a favorable direction, i.e. either towards higher concentrations of attractants [Fig. 1.2(b)] or lower concentrations of repellents. The details of the machinery for both motility and sensing are as diverse as the species that demonstrate these

behaviors and their respective habitats – chemotaxis is observed throughout all major prokaryotic lineages, including the archea – but there are also highly conserved design features at the molecular level [21, 22]. The basic paradigm established in studies of the model organism *Escherichia coli* [23] serves as a guide for exploring the plethora of possible variations on this theme.
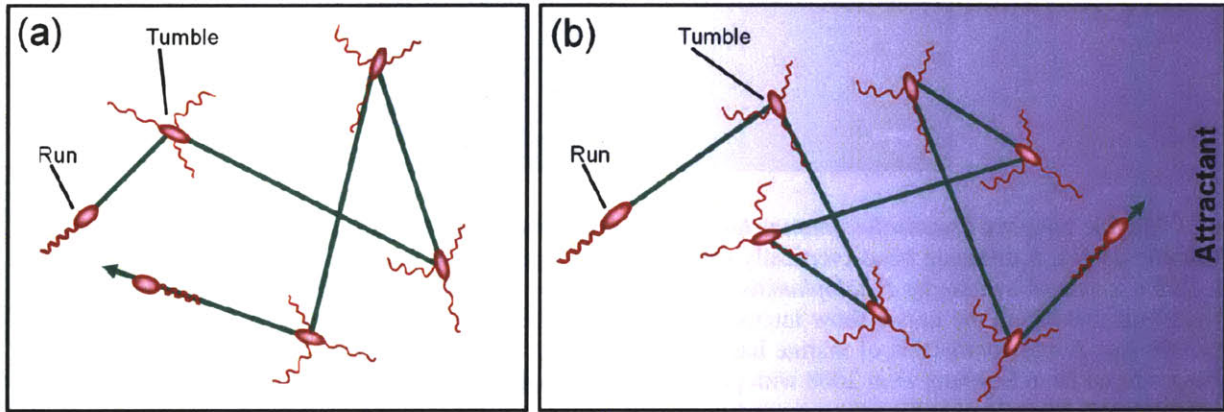
Figure 1.2 Schematic representation of random motility and chemotaxis. (a) In the absence of attractant gradients, bacterial motility can be characterized by a random walk consisting of "runs" interrupted by "tumbles", which cause a random change in direction. **(b)** In the presence of a chemoattractant gradient, this random walk becomes biased, resulting in longer runs in the direction of the gradient. The effect of this behavior is the net migration of a cell, and thus of a population, towards higher attractant concentrations.

E. coli propels itself by rotating multiple helical filaments, which are anchored to the cell wall by ion-driven molecular motors. When all motors rotate counterclockwise (looking from the distal end of the filament, toward the cell), the left-handed helical filaments coalesce into a coherent bundle yielding relatively straight trajectories, called "runs", that last ~1 s [Fig. 1.2(a)]. When one or more of the motors reverse direction (i.e. rotate clockwise), the bundle is disrupted, yielding a brief, erratic reorientation called a "tumble", which lasts ~0.1 s [20] [Fig. 1.2(a)]. Thus, the random-walk behavior of each cell can be described as a two-state sequence, consisting of runs and tumbles. The sensory system controlling this behavior responds to chemical cues by modulating the duration of runs. In the presence of an attractant gradient, tumbles are suppressed and runs are extended. This results in a biased random walk and causes a net migration of a bacterial population up the attractant gradient [Fig. 1.2(b)].
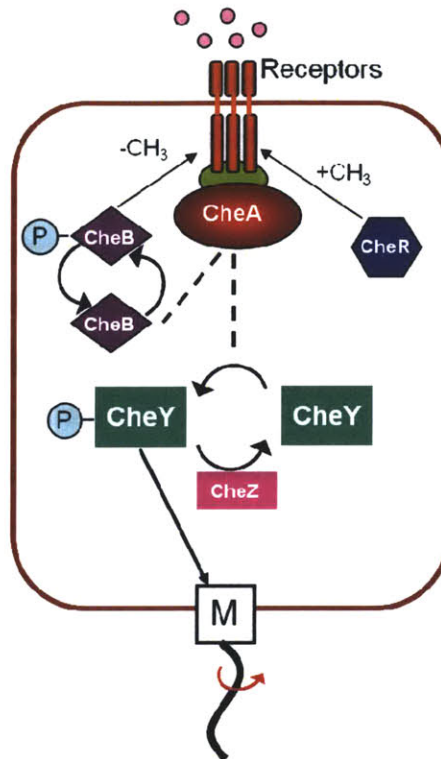
Figure 1.3 Molecular composition of the chemotaxis signaling pathway in bacteria. Receptors form stable complexes with the cytoplasmic histidine kinase CheA. CheA transfers phosphate group to response regulator CheY which controls the flagellar motor. CheZ, the phosphatase for CheY-P, decreases the signal lifetime and accelerates the excitatory response. Methyltransferase CheR and methylesterase CheB promote adaptation through covalent modification of receptors. This process compensates for chemoeffector binding on the receptors and resets its activity level.

The dynamics of the chemosensory system that controls runs and tumbles is crucial for effective chemotaxis. At the molecular level, the dynamics is governed by a regulated phosphotransfer between a histidine kinase and a response regulator. The histidine kinase CheA together with an adaptor protein CheW associates with membrane-spanning receptors to form receptor-kinase complexes. When receptors at the cell surface bind chemoeffector molecules, the CheA phosphoryl group is transferred to the response regulator CheY to form CheY-P, which then diffuses through the cytoplasm and binds to FliM, a component of the switch complex of the flagellar motor, and modulates the direction of motor rotation. The phosphatase CheZ binds to CheY-P and promotes its dephosphorylation. The binding of CheY-P to the motors enhances the probability of clockwise rotation of the flagella and tumbles are suppressed. The time-scale for this network of chemical reactions that result in a motor response is in the order of a few hundred milliseconds [24, 25] which is much shorter than the average duration of runs (~1 s). But gradient sensing is achieved by temporal comparisons, in which the level of stimulation by a

chemoeffector in the recent past is compared to that of 1-2 s earlier [26, 27]. Therefore, in addition to a sub-second time-scale excitatory response mechanism, the sensory system has to possess a short-term chemical "memory" and at the same time the capability to refresh this memory as it moves up or down a gradient. At the molecular level, this is done by methylation and demethylation of receptors by the methyltransferase CheR and the methylesterase CheB, respectively, which counteract the effect of bound chemoeffectors. Bound chemoeffectors change the autophosphorylation activity level of receptor-complexes (attractants decrease activity while repellents increase activity) and the covalent modification of receptors by CheR and CheB resets the pathway activity, i.e. promotes adaptation to changing ligand concentrations. However, kinetics of methylation/demethylation are relatively slow and adaptation can take tens or hundreds of seconds depending on the initial stimulation level [27]. This adaptation time scale roughly matches the average time over which swimming directions are decorrelated during runs (although swimming trajectories during runs are smooth, they are never perfectly straight, due to Brownian rotational diffusion, which induces a random component to the swimming direction) [20]. The steepness of the gradients that can be sensed is thus determined by the swimming speed (~30 μm/s in *E. coli*), which converts the spatial gradient into a temporal one, and the time scales of the chemical reactions underlying this sensory response.

Because of its relative simplicity, this signal transduction pathway is among the best characterized signaling systems in biology. Much recent work has focused on how this pathway achieves important physiological functions, such as precise adaptation [28, 29], signal amplification [30, 31] and temporal gradient sensing [32, 33], but many open questions remain in how these properties combine as a control strategy for migrating cell populations, as highlighted by a series of theoretical studies [34-41]. Following a decade of relative silence after the earlier theoretical work [34, 35], recent years have seen a spur of papers addressing questions of how intracellular signaling can affect the behavior of migrating cells and populations [34-41].

While *E. coli* represents the best-studied model system of bacterial motility and chemotaxis, a wide range of other motility strategies exists among bacteria. Two widely studied species that have a motility pattern closely related to that of *E. coli* are *Bacillus subtilis* and *Salmonella typhimurium*, both peritrichously flagellated (i.e. flagella projecting all around the cell body)

bacteria that swim in a run and tumble fashion. The former swims at ~30 μm/s [42], the latter at 29-55 μm/s [43]. Similar speeds (22-33 μm s^{-1}) [44] are also exhibited by *Helicobacter pylori*, which uses 2-6 unipolar flagella to swim and chemotax in the human stomach.

On the other hand, considerably larger speeds and markedly different swimming strategies compared to *E. coli* have been frequently reported. For example, monotrichous (i.e. having a single polar flagellum) bacteria such as *Shewanella putrefaciens*, *Deleya marina* and many other marine isolates swim using a 'run and reverse' strategy [45, 46], where the counterclockwise and clockwise rotation of their flagella imparts a forward and backward thrust respectively allowing them to make 180° reversals. Very recently, it has been discovered that another monotrichous bacterium *Vibrio alginolyticus*, native to both aquatic and marine environments, executes a cyclic three step motion: forward, reverse and flick [47] where the flick induces a fast reorientation of the cell and randomizes swimming direction [48]. Most of the marine bacteria have an average swimming speed of 144 μm/s with the maximum individual burst velocity exceeding 400 μm/s [49] while *V. alginolyticus* can swim at speeds of 77–116 μm/s [43]. All of these swimming speeds are considerably higher than that of *E. coli* although their body sizes are comparable to *E. coli*. The speed record, however, belongs to marine bacteria isolated from the water-sediment interface, where Candidatus *Ovibacter propellens* swims at up to 1000 μm/s [50]. The difference in swimming speed also suggests a difference in the signal processing time by their sensory system while reacting to gradients. Segall *et al.* [24] reported that a response time of 200 ms is sufficient for *E. coli* to react to sensed gradients before being reoriented by Brownian rotational diffusion. But Mitchell *et al.* [49] suggested that this was not a universal lower limit for the response time scale, and bacteria that can swim at a speed ~400 μm/s could possess a sensory system which would be capable of responding within a few milliseconds.

Bacteria from the sediment-water interface are often considerably larger than *E. coli*. For example, *Thiovulum majus* is up to 20 μm in size and because Brownian rotational diffusion scales with the inverse of the cube of bacterial size, these larger bacteria are considerably more effective at determining their swimming direction and their motility pattern has been denoted as 'steering' [51]. Yet other species swim in a run and stop mode (e.g. *Rhodobacter sphaeroides*

[52]). In many cases, very little or no information is available on the chemotactic preferences and the chemotactic pathways of these organisms.

1.3 Traditional chemotaxis assays

Chemotaxis assays have been used for more than four decades to quantify the preference of bacteria for a given chemical and the rates of their chemotactic motility in chemical gradients. The first quantitative bacterial chemotaxis assay was the capillary assay, developed by Julius Adler in the 1960s [53]. Several other assays have been developed since, including stopped-flow diffusion chambers (SFDC) [54], continuous-flow capillary assays [55], two-chamber glass capillary arrays [56], swarm plate assays [57], tethered cell assays [58], and automated tracking of swimming cells [20]. Excellent reviews of most of these assays can be found in Jain *et al.* [59] and Englert *et al.* [60] Here the salient features of some of these techniques are briefly discussed.

The basic operation of the capillary assay involves immersing a chemoeffector-filled capillary tube in a bacterial suspension and allowing the bacteria to sense and respond to the chemical gradient that forms near the mouth of the capillary by swimming into the capillary, as the chemical diffuses into the suspension [53]. The quantification of the bacterial response occurs by counting bacteria in the capillary after serial dilution and plating.

Exposure of a bacterial population to a transient, diffusing chemoeffector gradient is also the operating principle behind several subsequent assays. SFDC assays rely on suddenly stopping two impinging streams of a bacterial suspension that differ only in chemoeffector concentration [54, 61]. The distribution of bacteria along the evolving gradient is measured by light-scattering techniques, bypassing the need for the time-consuming plate counting characteristic of capillary assays, but still limiting resolution to population-scale measurements.

Swarm plate assays are based on inoculating a bacterial population on a semisolid agar plate made with metabolizable chemoattractant [57]. As bacteria gradually metabolize the chemoattractant, they create radial chemoattractant gradients that trigger their outward migration in characteristic rings. The rate at which the diameter of this ring increases provides a (rather coarse) measure of chemotaxis, and swarm plate assays are used primarily at a qualitative level.

Considerably more detailed information is provided by single-cell approaches, such as the temporal stimulation of tethered cells [58] and the three-dimensional tracking of individual bacteria in chemoeffector gradients [20]. These techniques are among the most sophisticated approaches, and in several aspects (e.g. the 3D tracking) remain largely unparalleled even by more modern methods. They have revealed fundamental mechanistic aspects of chemotaxis, enabling the quantification of run lengths, tumble frequencies and adaptation responses that paved the way for formulating theoretical models of bacterial chemotaxis.

All of these assays, developed before microfluidic technology, have yielded invaluable information on bacterial chemotaxis. There is little doubt that some of these techniques will continue to be used in many laboratories, whether it be for historical reasons, or because of the simplicity and/or convenience of the setup (e.g. capillary assays, swarm plates). Quantitative and rigorous characterization of bacterial motility is difficult to achieve with many of these techniques, however, and those that are amenable to quantitative analysis tend to be more difficult to implement, or laborious. Perhaps the most important and general difficulty in these bacterial chemotaxis assays that predate microfluidics arises when accurate characterization of chemoeffector gradients is desired. Both capillary assays and SFDCs have largely relied on mathematical modeling, rather than direct observation, to quantify chemoeffector gradients, but even small disturbances can significantly perturb or entirely disrupt gradients [62]. Furthermore, while some techniques provide single-cell observations (see above), many (e.g. capillary assays, swarm plates) measure the bacterial response only at the population level, with considerable uncertainty due to measurement techniques. Microfluidic technology offers the possibility to overcome these limitations by enabling generation of highly controlled chemical gradients and measurements of the bacterial response at high spatiotemporal resolution.

1.4 Advantages of a microfluidic approach to study bacterial chemotaxis

Microfluidics has become an important platform for biological research in a wide range of fields, spanning from cell biology to disease diagnostics and microbial community dynamics [63, 64] owing to the unprecedented degree of control it offers over the chemical and physical environments of cells at the microscale. Its advantages are essentially two-fold. Firstly, the

accurate control over channel geometries and fluid flow, combined with significant levels of automation in operation, provide an appealing strategy for controlling experiments involving gradients on a scale suitable for bacterial studies. Because of the low Reynolds number of most microfluidic flows, turbulence is absent and chemical gradients are smooth, straightforward to predict mathematically from the solution of the advection-diffusion equation. Therefore, microfluidics enables one to generate precise concentration gradients and systematically explore a wide range of parameters. Secondly, the size and transparency of microchannels are ideally suited for accurately measuring the concentration gradients as well as observing the bacterial response to the gradients by microscopy. Automated cell-counting by videomicroscopy and image analysis ensure excellent statistics on cell distributions. Furthermore, bacterial chemotaxis can be observed directly at the scale of the individual organism, by tracking single cells over time in well-defined chemoeffector gradients. Coupled with computer-controlled microscopy, this makes for a versatile platform to acquire data of unprecedented quality and quantity in experiments on bacterial chemotaxis.

Chemoeffector concentration profiles can be conveniently quantified by using tracer dyes. Use of fluorescent tracer dyes enables one to simultaneously visualize the chemoeffector concentration field and the bacteria (e.g. by imaging unlabeled bacteria in phase contrast, or fluorescently labeled bacteria at a different wavelength). Commonly used tracer dyes include fluorescein, carboxyfluorescein and red rhodamine. Fluorescein has been shown not to adversely affect the chemotactic response of bacteria [14], though this needs to be tested on a species-by-species basis for each dye. These dyes are useful as tracers because their diffusivities (e.g. 4.3×10^{-10} m^2 s^{-1} for fluorescein and rhodamine B at 25 °C [65]) are close to those of many low-molecular-weight solutes (e.g. 5.5×10^{-10} m^2 s^{-1} for α-methylaspartate [66]), hence their concentration field can be taken to represent that of the solute. Other dyes would have to be sought to represent concentration fields of chemoeffectors with significantly lower or higher diffusivity. Furthermore, the correspondence between dye and chemoeffector concentration breaks down in the case of metabolizable chemoeffectors, when bacteria consume a significant fraction of the chemoeffector over the course of the experiment. This effect can be minimized by working at low bacterial concentrations. Finally, non-fluorescent dyes such as trypan blue and food dyes are also commonly used and do not require a fluorescence detection setup for visualization. They are

best used to quantify gradients separately from the chemotaxis experiments, since their use can interfere with the visualization of bacteria.

Data acquisition is typically achieved by videomicroscopy using a digital camera, with a microscope configured for phase-contrast imaging, fluorescence imaging, or both. Phase contrast imaging has the advantage that it can be applied to any bacterial species and it is often used in microfluidic applications. It is particularly useful for studies of natural bacterial assemblages, where culturing is difficult and fluorescent tagging can be hard or undesirable. This can be a key benefit of the microfluidic approach in the near future, as environmental microbiologists are increasingly shifting focus from model organisms to natural assemblages.

1.5 Organization of the thesis

As is common in pioneering applications of novel technologies, many microfluidic studies of bacterial chemotaxis to date have placed a dominant focus on technical innovations. However, recent trends in the field seem to signal an exciting turning point, where novel and outstanding scientific questions are being addressed at an accelerating pace. Ability to track individual cells in controlled gradients provided the demonstration of logarithmic sensing of bacteria at the population-scale [67] and showed the effect of chemoreceptor ratio to cellular response within competing gradients [68]. Recent applications of microfluidic devices have also addressed bacterial chemotaxis in an artificial porous medium [69] and in transient nutrient patches or plumes in the ocean [14], not only indicating the versatility of these devices to mimic microenvironments, but also delivering valuable information on microbial processes at scales relevant to the native habitat of bacteria. As a continuation of this recent trend, this thesis aims to seek a fruitful integration between technology and biology by applying microfluidic tools to gain a broader understanding in problems pertaining to bacterial chemotaxis through four chapters which form the core of the thesis.

One of the key questions of systems biology is the influence of microscopic information of an individual cell on the behavior of the cell population. In bacterial chemotaxis, such a question can be formulated regarding the effect of single-cell swimming information on the population-scale chemotactic transport parameters. Previously, transport parameters have been derived

theoretically from single-cell swimming behavior using probabilistic models, yet the mechanistic foundations of this upscaling process have not been verified experimentally. In Chapter 2, novel microfluidic experiments are presented to quantify population-scale transport parameters (chemotactic sensitivity χ_0 and random motility μ) of a population of bacteria. A microfluidic capillary assay has been designed to generate and accurately measure gradients of chemoattractant (α-methylaspartate) while simultaneously capturing the swimming trajectories of individual *E. coli* bacteria using videomicroscopy and cell tracking. Measurement of swimming speed and bias in swimming direction enabled direct computation of chemotactic velocity V_C and the associated chemotactic sensitivity χ_0. The material of this chapter has been published in the paper titled *Experimental verification of the behavioral foundation of bacterial transport parameters using microfluidics* in the *Biophysical Journal* [70].

Most chemical gradients that bacteria experience in nature are essentially nonlinear. (e.g. concentration gradients of exudates generated by a leaky algae or an algal burst). Many traditional laboratory techniques to probe bacterial chemotaxis are based on generating nonlinear chemoattractant profiles (e.g. capillary assays, swarm plate assays). Although nonlinear gradients in the environment or in the laboratory are inherently unsteady, a steady nonlinear gradient scenario can represent a useful model in the limit of slow patch diffusion (e.g. high molecular weight compounds) or fast motility of bacteria. Steady nonlinear profiles can also be advantageous in investigating specific gradient sensing mechanisms for bacteria (i.e. logarithmic sensing in exponential gradients). Diffusion-based microfluidic devices can generate steady, arbitrarily shaped chemical gradients without requiring fluid flow and are ideal for studying chemotaxis of free-swimming cells such as bacteria. However, if microfluidic gradient generators are to be used to systematically study bacterial chemotaxis, it is critical to evaluate their performance with actual quantitative chemotaxis tests. In Chapter 3, three diffusion-based gradient generators have been characterized by confocal microscopy and numerical simulations to select an optimal design and apply it to chemotaxis experiments with *E. coli* in both linear and nonlinear gradients. Observed cell distributions along the gradients are compared with predictions from an established mathematical model, resulting in the first quantification of chemotaxis of free-swimming cells in steady nonlinear gradients. The material of this chapter

has been published in the paper titled *Bacterial chemotaxis in steady linear and nonlinear microfluidic gradients* in *Nano Letters* [71].

Recent theoretical developments in our understanding of the *E. coli* chemosensory network indicate that the chemotactic response can display a property called Fold Change Detection (FCD) over a wide range of background chemoeffector concentrations, if the magnitude of the stimuli is rescaled proportionately with the background [72]. Although the FCD property has been demonstrated in mammalian sensory systems (e.g. ambient light multiplying the contrast field in vision, protein concentrations multiplying the output in cellular signaling systems), its experimental validation for bacterial chemotaxis system is yet to be done. *In vivo* fluorescence resonance energy transfer (FRET) measurements for tethered cells, using time-varying stimuli, show that the FCD property holds in two adjacent but distinct regimes, spanning a ~500 fold range in background concentration. To determine whether FCD extends to freely swimming populations, an apparatus is required in which the behavior of individual cells can be observed in a highly controllable and manipulatable chemical environment. In Chapter 4, a previously developed steady linear gradient generator was used to test the FCD property in swimming bacteria. The spatial gradients are scaled with ambient concentrations and the evolution of bacterial distribution over time is recorded. Similar experiments were also performed for unsteady nonlinear gradients using a microfluidic injector channel developed by Seymour *et al.* [73] The results for the chemotactic response in linear gradients have been submitted for publication in a paper titled *Response rescaling in bacterial chemotaxis* in collaboration with Thomas Shimizu, Domenico Bellomo and Milena Lazova.

Chemotaxis is the ability of consumers to direct their movement toward regions of high resource concentration. A direct consequence of chemotactic migration is the formation of regions of high bacterial concentration, which become potential hotspots for predation by larger organisms such as protists. Since planktonic microbes in the microbial loop play an important role in energy flow in biogeochemical cycles [11, 12, 15, 74], investigating the foraging abilities of microbes is crucial to quantify their effects on trophic transfer and biogeochemical rates in the environment. Furthermore, the environment harboring the microbes can have complex spatial configurations (e.g. pores in subsurface environments or within marine snow particles in the ocean). In Chapter

5, using a steady linear gradient of chemoattractants, a heterogeneous prey (bacteria) distribution triggered by chemotaxis was generated to investigate the effect of predation by a predator (protist). By measuring the temporal spatial distribution of bacteria and analyzing the movement behavior of the protists, the rate of predation and its effect on bacterial demographics were determined. The effects of predation on landscapes with varying spatial complexities were also explored.

Chapter 6 presents conclusions and recommendations for future work.

Chapter 2

Experimental verification of the behavioral foundation of bacterial transport parameters using microfluidics[a]

2.1 Introduction

To predict the ability of a bacterial population to disperse and migrate in the presence of chemical gradients it is essential to quantify chemotactic motility. Observation of microscopic 'run and tumble' phenomena of bacterial motility revealed that when bacteria experience favorable chemical gradients, tumbles are suppressed [26, 75], resulting in increased run-lengths towards the attractant gradient, the manifestation of which in the population-scale is a net chemotactic drift with velocity V_C towards an attractant, or away from a repellent. At the population scale, this behavior has been characterized by a phenomenological model for the flux of cells J proposed by Keller and Segel [76], which in one dimension (x) reads

$$J = -\mu \frac{\partial B}{\partial x} + V_c B \,. \tag{2.1}$$

Here, $B(x,t)$ is the concentration of bacteria, t is time and μ is the random motility coefficient, measuring the diffusivity of a population of bacteria resulting from their random walk behavior. Coupled with the conservation equation $\partial B/\partial t = -\partial J/\partial x$, Eq. 2.1 gives an advection-diffusion equation for the bacterial population, known as bacterial transport equation:

$$\frac{\partial B}{\partial t} = \frac{\partial}{\partial x}\left(\mu \frac{\partial B}{\partial x}\right) - \frac{\partial}{\partial x}\left(V_c B\right). \tag{2.2}$$

In the absence of chemoattractants, $V_C = 0$ and Eq. 2.2 reduces to the diffusion equation. When a chemoattractant is present, the chemotactic velocity V_C depends on the chemoattractant concentration gradient, hence is not an intrinsic property of a bacterium-chemoattractant pair. Instead, such a role is played by the chemotactic sensitivity coefficient χ_0, expressing the strength of attraction of a population to a given chemical. The relation between V_C and χ_0 is discussed below. It follows from Eq. 2.2 that knowledge of μ and χ_0 enables one to predict bacterial transport in any given concentration field. Conversely, observed bacterial distributions can be used to determine μ and χ_0 by fitting Eq. 2.2.

A wide range of chemotaxis assays has been developed to measure the strength of attraction of a bacterial population to a given chemical (see Chapter 1). The classic 'capillary assay' [77] is the

most widespread, due to its simplicity. However, capillary assays are not conducive to the measurement of transport parameters [78, 79], as chemoattractant gradients are exceedingly difficult to quantify and can be easily perturbed even by minor residual flows [62]. Furthermore, the need for plate-counting considerably increases processing time and reduces accuracy. Quantification of transport parameters has typically relied on more controlled gradient-generation devices, like the stopped-flow diffusion chamber (SFDC) [54], coupled with direct measurement of $B(x,t)$ using light scattering or related techniques [54, 80, 81]. These studies all have employed a population-scale approach, requiring a rather complex procedure to determine μ and χ_0 based on seeking time-dependent, numerical solutions of Eq. 2.2 for the particular geometry at hand and fitting them to the observed bacterial distribution $B(x,t)$. Furthermore, most studies have relied on theoretical predictions of the chemoattractant concentration instead of measurements [55, 61, 82], considerably increasing uncertainty in light of the extreme sensitivity of the concentration field to perturbations. Here a direct approach is presented to compute bacterial transport parameters from single-cell swimming information and direct measurements of the concentration field, thus bypassing the need to solve the bacterial transport equation.

The theoretical link between population-scale transport and single-cell chemotactic motility behavior has been derived by Rivero et al. [83] based on a previous model by Othmer et al. [84] Farell et al. [82] verified Rivero's model experimentally for surface-attached leukocytes. For free-swimming bacteria, the mechanistic foundation of a population-scale transport formulation has to date gone untested, partly due to the experimental difficulty of obtaining single-cell data of freely-swimming organisms in a controlled concentration field. Besides, the chemotactic response of bacteria differs fundamentally from that of leukocytes: leukocytes bias the direction of their movement [83] while bacteria modulate run lengths [20]. Here Rivero's model is experimentally tested by tracking individual E. coli bacteria exposed to a range of well defined chemoattractant gradients, generated using microfluidic devices.

Microfluidic devices consist of μm to mm-sized flow channels that can be fabricated rapidly and precisely [64, 85] and have extensively been used to generate accurate chemical gradients [86-91]. In the context of chemotaxis, these devices have been designed and applied primarily to

study chemotaxis of surface-attached cells [86, 88, 90, 92]. Microfluidic investigations of chemotaxis of free-swimming microorganisms have been more limited [89, 93-95], neither attempting to compute chemotaxis parameters nor investigating the bacterial response at the single-cell level. Here it is shown that microfluidics optimally lends itself to quantitative chemotaxis assays to determine population-scale transport parameters directly from single-cell trajectories.

2.2 Theoretical Background

Rivero *et al.* [83] present a mathematical model that links single-cell and population-scale descriptions of chemotaxis for bacteria swimming in a one-dimensional (1D) domain (x) at speed v_{1D}, with a chemoattractant gradient along x. Bacteria are modeled as two subpopulations of concentrations n^+ and n^-, swimming in opposite directions (+x and –x, respectively). Cell conservation dictates:

$$\frac{\partial n^+}{\partial t} + \frac{\partial}{\partial x}(v_{1D}n^+) = p^- n^- - p^+ n^+,$$
(2.3)

$$\frac{\partial n^-}{\partial t} - \frac{\partial}{\partial x}(v_{1D}n^-) = p^+ n^+ - p^- n^-,$$
(2.4)

where p^+ is the probability per unit time that an n^+ cell tumbles and becomes an n^- cell (and vice-versa for p^-). [Fig. 2.1] Tumbles are assumed to be instantaneous. Addition of these two equations yields the cell conservation equation $\partial B/\partial t = -\partial J/\partial x$, where $B = n^+ + n^-$ is the overall bacterial concentration and $J = v_{1D}$ (n^+ - n^-) is the bacterial flux. An equation for the bacterial flux can be obtained by subtracting Eq. 2.3 from Eq. 2.4 and rearranging:

$$\frac{\partial J}{\partial t} - \frac{J}{v_{1D}}\frac{\partial v_{1D}}{\partial t} = -J\left(p^+ + p^-\right) - v_{1D}\frac{\partial}{\partial x}\left(v_{1D}B\right) - v_{1D}B\left(p^+ - p^-\right).$$
(2.5)

For observation times larger than the persistence time $(p^+ + p^-)^{-1}$, a quasi steady-state value for the local flux can be assumed ($\partial J/\partial t = 0$). The persistence time for *E. coli* is ~ 0.5 s, considerably shorter than observation time in our experiments. With the further assumption that swimming speed is constant over space and time, Eq. 2.5 reduces to:
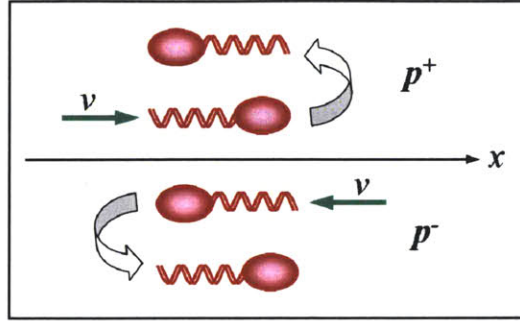
Figure 2.1 Schematic representation of the two tumbling probabilities p^+ and p^-. p^+ (p^-) are defined as the probability of a cell moving in the positive (negative) x-direction becomes a cell moving in the negative (positive) x-direction. v is the swimming speed.

$$J = -\frac{v_{1D}^2}{p^+ + p^-} \frac{\partial B}{\partial x} + v_{1D} \frac{p^- - p^+}{p^+ + p^-} B \,. \tag{2.6}$$

This is equivalent to Eq. 2.1, with $\mu = (v_{1D})^2 / (p^+ + p^-)$ and $V_C = v_{1D} (p^- - p^+) / (p^+ + p^-)$. Chen *et al.* [96] show that Eq. 2.1 also applies to cells swimming at speed v_{3D} in a 3D domain with a chemoattractant gradient along a single dimension x, with somewhat modified expressions for V_C ($= (2/3)v_{3D} (p^- - p^+) / (p^+ + p^-)$) and μ ($=(2/3)v_{3D}^2 / [(p^+ + p^-)(1 - \psi)]$), where ψ is the directional persistence [~0.3 for *E. coli*; [20]]. Ford and Cummings [97] further demonstrate that, if one measures the 2D velocity v_{2D} resulting from the projection of the 3D swimming speed v_{3D} onto a 2D plane, as is often done in microscopy, one can still use these same expressions for V_C and μ, after replacing v_{3D} with $4v_{2D}/\pi$.

$$V_C = \frac{8v_{2D}}{3\pi} \frac{T^+ - T^-}{T^+ + T^-} = \frac{8v_{2D}}{3\pi} \frac{1 - \beta}{1 + \beta}, \tag{2.7}$$

$$\mu = \frac{16v_{2D}^2 T_0}{3\pi^2 (1 - \psi)}, \tag{2.8}$$

where the mean run times are given by $T^+ = 1/p^+$ and $T^- = 1/p^-$ ($T^+ = T^- = T_0$ in the absence of chemoattractant gradients), and the swimming direction asymmetry, $\beta = T^-/T^+$ ($\beta = 1$ represents no chemotaxis, $\beta = 0$ is deterministic motion up the gradient).

33

Again, V_C is not an intrinsic property of a population, as it varies with the gradient dC/dx of the chemoattractant concentration $C(x)$. The parameter intrinsically measuring the attraction of a population to a given chemical is the chemotactic sensitivity χ_0, which Rivero's model relates to V_C as [83, 96]

$$V_C = \frac{8v_{2D}}{3\pi} \tanh\left(\frac{\chi_0 \pi}{8v_{2D}} \frac{K_D}{(K_D + C)^2} \frac{dC}{dx} \right),$$
(2.9)

where K_D is the receptor/ligand dissociation constant. The derivation of Eq. 2.9 for the 1D case is given in the Appendix A. For *E. coli* exposed to α-methylaspartate, K_D has been estimated as 0.125 mM [98] or 0.160 mM [99]. For this purpose, it proves convenient to rewrite Eq. 2.9 as

$$P = \chi_0 Q,$$
$$P = \tanh^{-1}\left(\frac{3\pi V_C}{8v_{2D}} \right); \quad Q = \frac{\pi}{8v_{2D}} \frac{K_D}{(K_D + C)^2} \frac{dC}{dx},$$
(2.10)

and determine χ_0 as the slope of the best-fit line of Q vs. P. Here, β and v_{2D} will be directly measured to calculate V_C from Eq. 2.7, and further measure C and dC/dx to compute χ_0 from Eq. 2.10.

Finally, to measure the random motility μ of a bacterial population a 1D band of bacteria (of initial width $(2\mu t_0)^{1/2}$) will be created and their spread as a result of their random walk behavior will be observed. μ will be computed by fitting the observed spatiotemporal distributions of bacteria to the analytical solution of the diffusion equation (Eq. 2.2 with $V_C = 0$) in an infinite domain, given by

$$B(x,t) = \frac{1}{\sqrt{4\pi\mu(t + t_0)}} e^{-\frac{x^2}{4\mu(t+t_0)}}.$$
(2.11)

2.3 Materials and Methods

2.3.1 Bacteria, growth conditions and chemoattractants

E. coli HCB1 (provided by H. Berg) was grown in Tryptone Broth at 34 °C on an orbital shaker (220 rpm) to mid-exponential phase (optical density = 0.4), then washed thrice by centrifuging at 2000g for 5 min and resuspending the pellet in motility buffer (10 mM potassium phosphate, 0.1 mM EDTA, 10 mM NaCl; pH = 7.5). The suspension was further diluted (1:5 – 1:2) in motility buffer to ensure optimal cell concentration for tracking.

For chemotaxis experiments, *E. coli* cells were exposed to the non-metabolizable chemoattractant α-methylaspartate (Sigma-Aldrich, USA) diluted in motility buffer. Three sets of experiments were performed, corresponding to initial chemoattractant concentrations in the microchannel of $C_0 = 0.1$, 0.5 and 1.0 mM. A different bacterial batch was used for each set of experiments. Fluorescein (Sigma-Aldrich, USA) was added to α-methylaspartate solutions to visualize the concentration field by epifluorescence microscopy, using an EXFO X-Cite 120 fluorescent lamp (Photonic Solutions, Ontario, Canada). Fluorescein has a diffusion coefficient of 5×10^{-10} m^2 s^{-1}, nearly identical to α-methylaspartate [5.5×10^{-10} m^2 s^{-1}; [66]]. It has been previously verified that fluorescein does not induce chemotaxis in *E. coli* [14]. For random motility experiments, nine realizations were performed, using two different batches of bacteria.

2.3.2 Microchannel fabrication

Microfluidic devices were fabricated using soft lithography techniques [64, 86]. The channel design was produced using CAD software (Autodesk) and printed onto transparency film with a high-resolution image setter (Fineline Imaging, Colorado Springs, CO, USA), creating a design 'mask'. A 60 μm thick layer of negative photoresist (SU8-2100; Microchem, Newton, MA, USA) was applied to a 4-inch silicon wafer (University Wafer, South Boston, MA, USA) by spin-coating. With the mask laid onto the coated wafer, exposure to UV light was used to polymerize exposed regions of the photoresist, appending an impression of the channel design onto the silicon wafer (the 'master'). Positive replicas with embossed channels were fabricated by molding polydimethylsiloxane (PDMS, Sylgard 184; Dow Corning, Midland, MI, USA) against the master and baking at 65° C for 12 h. The hardened PDMS, containing the channel

structure, was then peeled from the master and cut to size. Access holes for tubing were punched using a sharpened lure tip. The PDMS layer was then sealed against a glass microscope slide by exposure to oxygen plasma (Harrick Plasma Cleaner/Sterilizer; Harrick Scientific, Ossing, NY, USA) for 1 min, forming a covalent bond and completing the microfluidic channel. Peek tubing (Upchurch Scientific, WA, USA), with inner/outer diameters of 0.76/1.59 mm, was inserted into inlets and outlet.
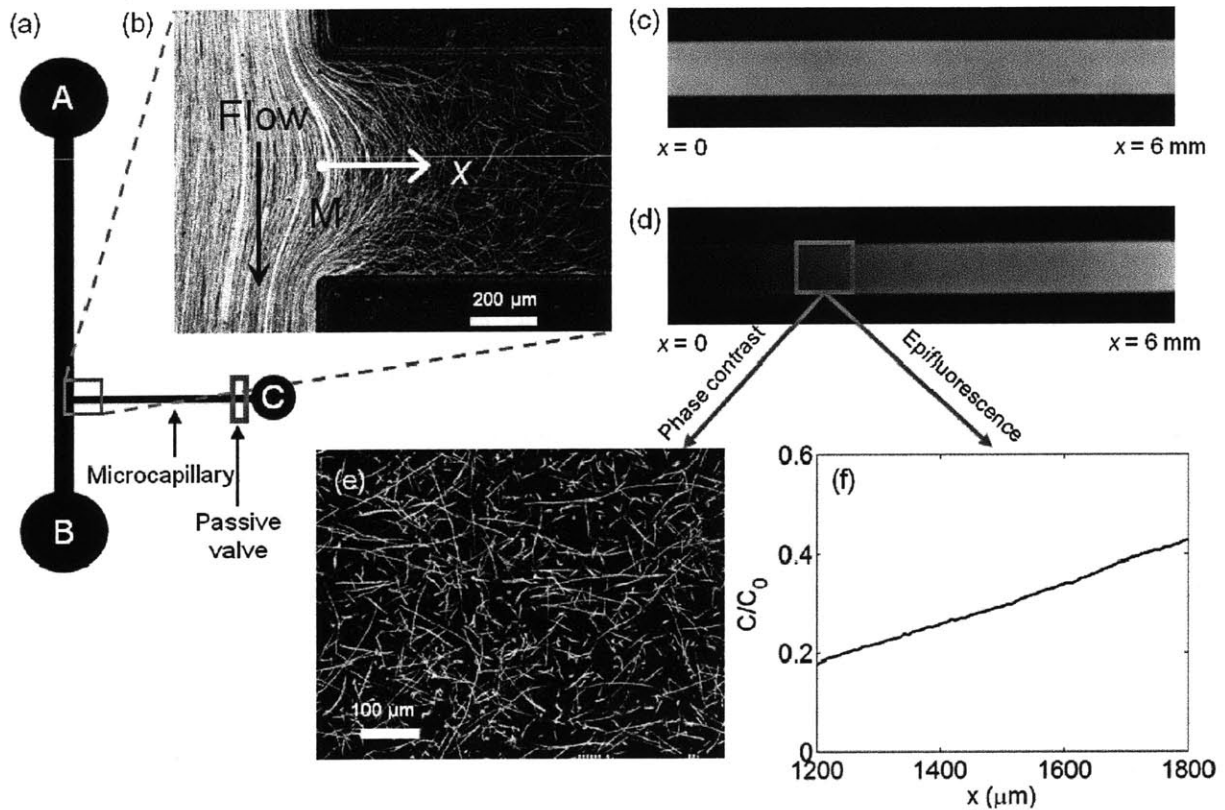
Figure 2.2 Experiments to determine the chemotactic sensitivity χ_0 of *E. coli*. **(a)** Schematic of the microfluidic channel. Chemoattractant and fluorescein were injected in the microcapillary via inlet C, by means of a passive valve. **(b)** Flow in the main channel (from A to B) was used to transport *E. coli* bacteria past the mouth (M) of the microcapillary, where a fraction of the population swum into the microcapillary. Each white path is an *E. coli* trajectory. The image is a superposition of 200 frames captured over 6.2 s. **(c,d)** Epifluorescence images (using a 2× objective) of the microcapillary, initially filled uniformly with α-methylaspartate ($t = 0$; panel c), and later exhibiting a non-uniform concentration profile ($t = 45$ min; panel d). The latter was used to probe the chemotactic response of the *E. coli* cells that had swum into the microcapillary. 100 μM fluorescein was added to variable concentrations of α-methylaspartate (0.1, 0.5, or 1.0 mM) for visualization. **(e)** Trajectories of *E. coli*, from 300 frames recorded over 9.4 s using a 20× objective. **(f)** Concentration profile $C(x)$ obtained from (d) and normalized by the initial concentration C_0 in the microcapillary. The field of view is the same as in (e).

2.3.3 Microchannel layout and operation

Two different microchannels were fabricated. The first [Fig. 2.2(a)] was used to determine χ_0 and consisted of a 20 mm long, 1 mm wide and 60 μm deep main channel, with a 9 mm long, 0.6 mm wide and 60 μm deep side channel (the 'microcapillary'), branching off from the main one at a right angle. The direction along the microcapillary will be denoted by x, with $x = 0$ at the mouth of the microcapillary (M, in Fig. 2.2(a)). Before the start of an experiment, a solution of α-methylaspartate and fluorescein was injected in the microcapillary via inlet C [Fig. 2.2(a)] using a 1ml plastic syringe. Inlet C was equipped with an on-chip passive valve [92], which allowed flow under sufficient pressure, such as that exerted by gentle manual injection, and prevented it otherwise, so that the microcapillary was sealed from external perturbations.

After completely filling the microcapillary with chemoattractant, motility buffer was injected into the main channel via inlet A at a constant flow speed of 300 μm s^{-1}, using a 1 ml plastic syringe driven by a syringe pump (PHD 2000, Harvard Apparatus, Holliston, MA, USA), and collected at the outlet B. The continuous buffer flow washed out any chemoattractant that had leaked from the microcapillary into the main channel and established a boundary condition of zero chemoattractant concentration ($C = 0$) at the mouth M of the microcapillary. From this time on, the concentration profile of chemoattractant $C(x)$ in the microcapillary evolved as a result of molecular diffusion and $C = 0$ at M. After approximately 45 min, injection from inlet A was switched from buffer to a suspension of *E. coli* using an external valve. Maintaining the same flow speed prevented any flow disruption in the microchannel. A fraction of the bacteria advected past the mouth of the microcapillary swam into it and moved up the concentration gradient [Fig. 2.2(b)]. Their trajectories were subsequently recorded, along with the concentration gradient, as described in the next section.

A second microchannel [Fig. 2.8(a)] was used to measure the random motility μ of *E. coli* from the lateral diffusion of a thin band of cells. This microchannel, described in detail elsewhere [14], consisted of a 45 mm long, 3 mm wide and 50 μm (three realizations) or 100 μm (six realizations) deep channel, with two in-line inlet points, used to separately introduce motility buffer and bacteria with the syringe pump. The inlet through which bacteria were introduced led to a 100 μm wide PDMS microinjector, which focused the bacteria in a thin band at the center of

the main channel. The second inlet was used to flow buffer into the channel, so that the bacterial band was sandwiched between two buffer streams. The three streams flowed side by side, at the same mean speed of 240 μm s^{-1}, until the experiment was started by turning off the flow. This 'released' the thin bacterial band, which thereafter spread laterally due to random motility. The distribution of bacteria across the channel was captured over time using videomicroscopy, at a fixed location 5 mm downstream of the microinjector tip.

2.3.4 Data acquisition and processing

All experiments were conducted using a computer-controlled inverted microscope (TE2000-E, Nikon, Japan), equipped with a 1600x1200 pixels, 14-bit CCD camera (PCO 1600, Cooke, Romulus, MI, USA). For the set of experiments designed to quantify χ_0, chemoattractant concentrations and gradients in the microcapillary were measured by addition of 100 μM fluorescein to α-methylaspartate solutions, and epifluorescence imaging with a 2$\times$ objective [Fig. 2.2(c,d)]. Fluorescein was visualized using a FITC filter cube, with excitation at 460-500 nm and emission at 515-560 nm. An earlier study showed that 300 ms pulses of blue light can briefly (<2s) affect motility of E. coli [100]. In our experiments, epifluorescent light pulses lasted 200 ms and at least 15s elapsed between a pulse and data collection. Furthermore, swimming speeds recorded before and 8 s after a 200 ms pulse showed negligible variation (< 5%). Fluorescent intensity was converted to concentration via a previously determined calibration curve, which was found to be linear in the range of interest (0 to 1 mM α-methylaspartate). Across-channel averaging gave a 1D concentration profile $C(x)$ along the microcapillary [Fig. 2.2(e)].

Bacteria were observed at mid-depth of the microcapillary, using phase contrast microscopy and a 20$\times$ objective. For each experimental run, a sequence ('movie') of 300 frames was captured over 9.4 s (32 frames/s). Each movie was analyzed using BacTrack, an in-house cell tracking software, to obtain bacterial trajectories: first, each frame was subtracted from the following one to remove background and obtain a cleaner image; then, bacteria in each frame were located as peaks in a monochrome intensity field; finally, bacteria were tracked between frames using particle tracking algorithms. Postprocessing of trajectories in Matlab (The Mathworks, Natick, MA, USA) yielded the 2D swimming speed of each bacterium and thus the population-average

38

velocity v_{2D}, as well as the swimming direction asymmetry β. The latter, as defined above, is the ratio of times spent traveling down and up the gradient, respectively. Because individual trajectories tended to be short as a result of bacteria swimming out of the focal plane, it was not possible to calculate β for each trajectory. Instead, β was equivalently calculated as the ratio of the sums of travel times for all trajectories down and up the gradient, respectively. Using v_{2D} and β the chemotactic velocity V_C is then calculated from Eq. 2.7.

To sample a range of concentration/concentration-gradient pairs while ensuring nearly simultaneous measurement of bacterial trajectories, the following automated acquisition sequence was adopted: (i) a 2× (the number refers to the power of the objective) epifluorescent image of a 6mm-long segment of the microcapillary; (ii) five to six 20× phase-contrast movies at different locations within the previous 2× field of view, using computer-controlled motion of the microscope stage; and (iii) a second 2× epifluorescent image at the same location as (i). This routine lasted approximately 4 min, which accounts for switching of objectives, filters and illumination source as well as stage motion. Comparison between the two epifluorescent images allowed us to quantify the change in the concentration profile over the 4 min time interval. The mean between the two profiles was used for further analysis and denoted $C(x)$. By selecting the region of $C(x)$ corresponding to each 20× movie, a mean concentration C (as the average of $C(x)$ over the 20× window) and a concentration gradient dC/dx (by a linear fit to $C(x)$ over the 20× window) were obtained.

For the set of experiments performed to quantify μ, bacteria were imaged at mid-depth, 5 mm downstream of the microinjector tip [Fig. 2.8(a)], using phase-contrast microscopy and a 10× objective, by taking a 100-frame movie at 32 frames/s every 20 s for 2 min after release of the bacterial band. Bacterial positions in the direction across the channel (x) were determined over all frames in a movie by image analysis as described earlier, yielding the cell distribution $B(x,t)$. Each profile $B(x,t)$ comprised at least 400 bacterial counts and the experiment was repeated nine times.

2.4 Results

2.4.1 Generation and measurement of chemoattractant gradients

To reliably quantify the chemotactic sensitivity χ_0, it is crucial to generate stable chemoattractant concentration profiles and measure them accurately. The on-chip passive valve allowed flow during manual injection to fill the microcapillary with α-methylaspartate solutions, while otherwise successfully preventing any external perturbation from inlet C. This was confirmed by visually observing 2 μm fluorescent latex beads, which were found to not move except by Brownian motion. Furthermore, epifluorescent imaging of fluorescein concentration showed that switching the external valve controlling inflow in the main channel (inlet A) from buffer to bacterial solution did not perturb the concentration profile in the microcapillary.

At the mouth (M) of the microcapillary, flow from the main channel partially intruded into the microcapillary (~ 600 μm; Fig. 2.2 (b)), exposing bacteria to chemoattractant gradients. A fraction of the bacteria swam out of the flow and into the microcapillary [Fig. 2.2(b)]. Because motility is required to move into the microcapillary, this setup guaranteed that only motile cells were subsequently assayed, while dead cells and debris from the bacterial culture (e.g. the thicker streaks in the main channel, Fig. 2.2(b)) were washed away. Incidentally, the observed flow intrusion generates a more complex concentration field in the mouth region than predicted by analytical solutions used in previous chemotaxis studies [55] and underscores the importance of direct visualization of the fluid mechanical and chemical environment in a chemotaxis assay. In our experiments, this did not represent a problem, because direct measurement of concentration prevented artifacts associated with the use of analytical solutions. Furthermore, flow in the main channel was turned off well before data collection in the microcapillary began. Flow, then, was used only to initially set up a concentration profile inside the microcapillary and advect bacteria to the mouth of the microcapillary.

Data were collected in the microcapillary between $x = 0$ and 3 mm at different times, to ensure the chemotactic response of bacteria was captured for a wide range of $(C, dC/dx)$ pairs. Fluorescent intensity images revealed that concentration varied only along the microcapillary (x) and was uniform across it (not shown). Three series of experiments with different initial

40

concentrations of α-methylaspartate (C_0 = 0.1, 0.5 and 1.0 mM) were performed. The measured values of C and dC/dx, summarized in Fig. 2.7, ranged from 0.007 to 0.970 mM [$0.06K_D$ – $7.76K_D$; K_D = 0.125 mM [98]] and from 0.02 to 0.5 mM/mm, respectively. Larger values of C were prevalently sampled at locations further inside the microcapillary, where dC/dx was smaller, while cases with smaller C came primarily from closer to the mouth, where dC/dx was initially large and progressively decreased.

2.4.2 Measurement and analysis of bacterial trajectories

Simultaneously to concentration profile measurements, tracked individual bacteria swimming in the microcapillary were tracked. The mean 2D swimming velocity was v_{2D} = 29.8±2.7 μm s^{-1}, corresponding to v_{3D} = $4v_{2D}/\pi$ = 37.9 μm s^{-1}. Statistical analysis revealed no correlation of v_{2D} with either C or dC/dx, confirming the absence of chemokinetic behavior. On the other hand, the swimming direction asymmetry β and the chemotactic velocity V_C were strongly correlated with the chemoattractant concentration field. Differences in β were so strong as to be discernible visually from sample trajectories [Fig. 2.3]. When concentration gradients were large and concentration was well below saturation ($C<<K_D$; Fig. 2.3(a,c)), trajectories showed a clear bias of motion up the gradient (black) compared to down the gradient (gray). This resulted in small values of β (0.46 and 0.40 for panels a and c, respectively) and large values of V_C (12.6 and 9.3 μm s^{-1}). In contrast, trajectories were nearly equally partitioned between up and down the gradient when concentration exceeded saturation values ($C>>K_D$; Fig. 2.3(b,d)), resulting in considerably larger β (0.78 and 0.79 for panels b and d, respectively) and smaller V_C (2.7 and 3.1 μm s^{-1}).

For each value of the initial chemoattractant concentration (C_0 = 0.1, 0.5, 1.0 mM) V_C was computed from Eq. 2.7, for a range of times and positions along the microcapillary. V_C ranged from 0.6 μm s^{-1} (β = 0.95) to 13.8 μm s^{-1} (β = 0.36), corresponding to 1.8% and 35% of the swimming speed v_{3D}, respectively. To ensure statistical significance of V_C, a convergence test was performed for each experiment, by calculating V_C from a progressively increasing portion of time t of a movie. Two examples are shown in Fig. 2.4, for a successful (solid line) and a failed (dotted line) converge tests. The estimate of V_C was considered statistically significant when the standard deviation computed from t = 6.6 to 9.4 s (i.e. the final 30% of a movie) did not exceed

41
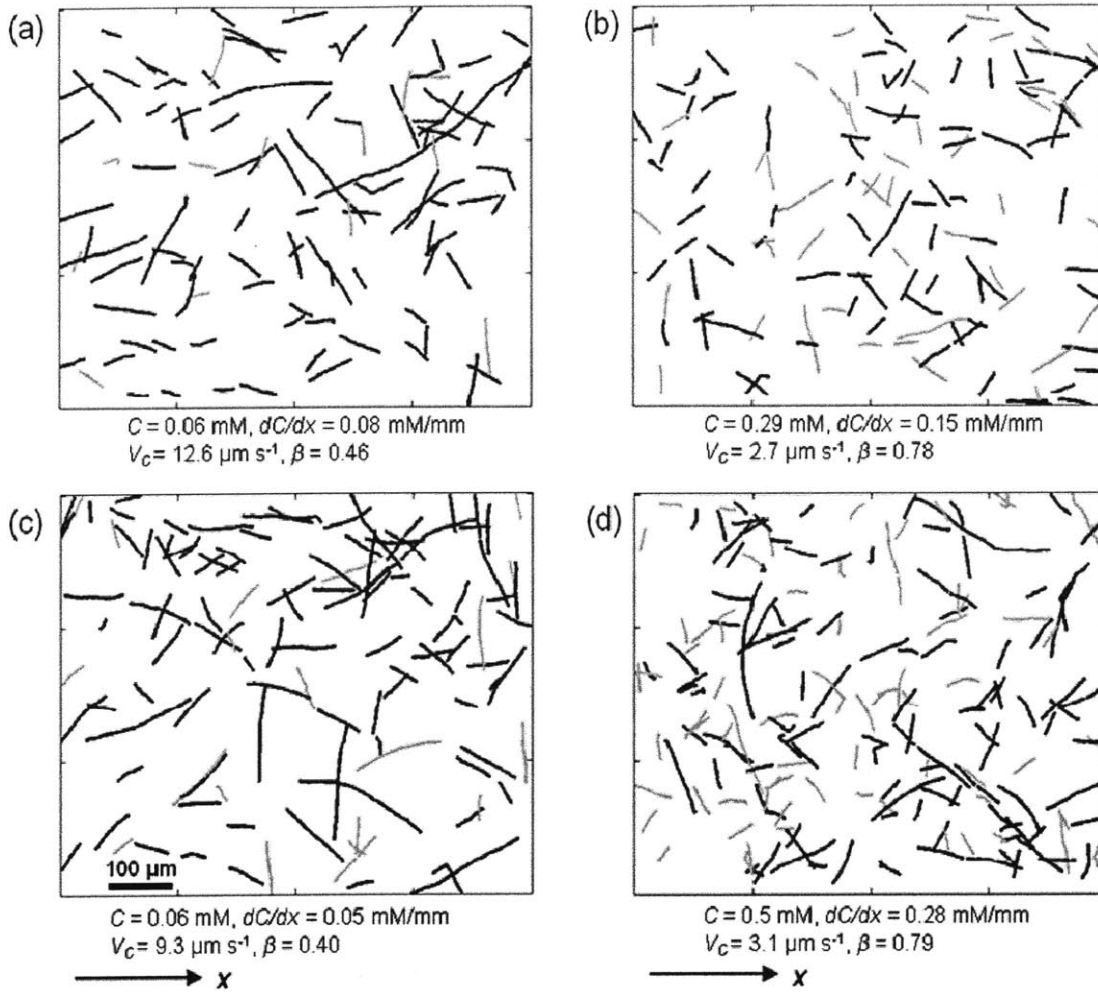
Figure 2.3 Digitized trajectories of *E. coli* corresponding to different combinations of chemoattractant concentration *C* and concentration gradient *dC/dx*. Concentration increased along *x*. Black (gray) trajectories had a net positive (negative) displacement in the direction of the gradient and contributed to the total cumulative time T^+ (T) cells spent traveling up (down) the gradient. **(a,c)** $C \ll K_D$ ($K_D = 0.125$ mM): most cells swum up the gradient, resulting in a small swimming direction asymmetry β and a large chemotactic velocity V_C. **(b,d)** $C \gg K_D$: receptors saturated, chemotaxis diminished and trajectories were nearly equally partitioned between up- and down- the gradient.

0.5 μm s^{-1}. For most experiments, 9.4 s of data were sufficient to achieve convergence. This corresponded to cumulative trajectory-time (i.e. the sum of the durations of all trajectories in a movie) ranging from 376 to 1164 s, or an average of 40-120 bacteria in the field of view. Only in two out of 28 cases was convergence not achieved and those cases were discarded from the analysis.
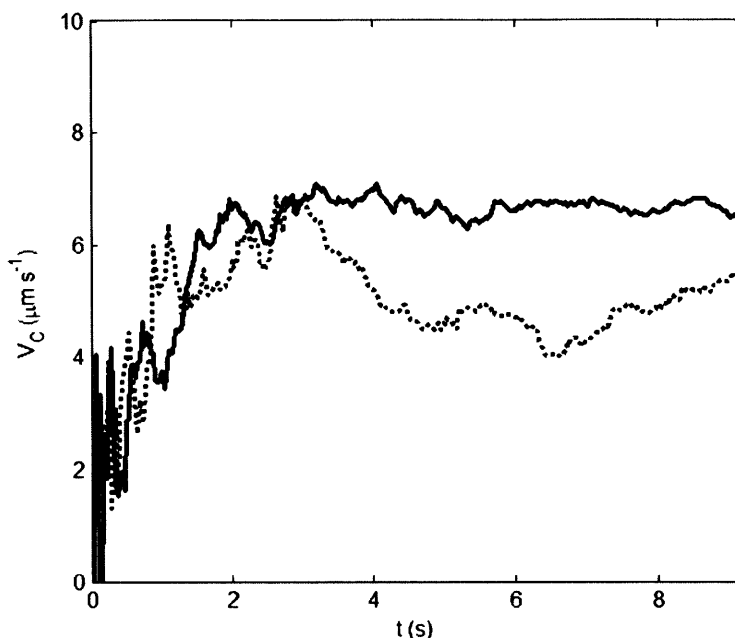
Figure 2.4 The chemotactic velocity V_C as a function of time t elapsed in a movie, to test for convergence of V_C. The solid line shows an experiment where V_C converged to 7.1 μm s^{-1}, while the dotted line corresponds to a run where V_C did not converge. The latter case was discarded from further analysis. The cumulative trajectory time for the two cases was 907 and 494 s, respectively. A recording time of 9.4 s was typically sufficient to ensure convergence, and only two out of 28 experiments failed to converge.

2.4.3 Chemotactic sensitivity coefficient χ_0

Direct measurement of v_{2D} and V_C for the 26 pairs of C and dC/dx described above [Fig. 2.7(a)] enabled the testing of the relation between chemotactic velocity and chemotactic sensitivity (Eq. 2.9) which was done separately for the three sets of experiments, corresponding to three initial chemoattractant concentrations C_0. A successful verification of Eq. 2.9 would have two features: a linear variation of $P = \tanh^{-1}[3\pi V_C/(8v_{2D})]$ with $Q = \pi/(8v_{2D})[K_D/(K_D+C)^2](dC/dx)$ (Eq. 2.10), and a slope $\chi_0 = P/Q$ that is independent of C_0. Experimentally determined values of v_{2D}, V_C, C and dC/dx were used to compute P and Q for each of the 26 experiments, assuming $K_D = 0.125$ mM [98]. In Fig. 2.5, P as a function of Q is plotted for $C_0 = 0.1$, 0.5 and 1.0 mM. In all three cases a linear relation satisfactorily describes the dependence of P on Q, as supported by the large value of the correlation coefficient r^2, with the biggest scatter in the 0.5 mM data ($r^2 = 0.93$). A least-squares fit constrained to go through the origin gave $\chi_0 = 13.5 \times 10^{-4}$, 14.3×10^{-4} and 9.6×10^{-4} cm^2 s^{-1} for $C_0 = 0.1$, 0.5 and 1.0 mM, respectively, with an average of $\chi_0 =$
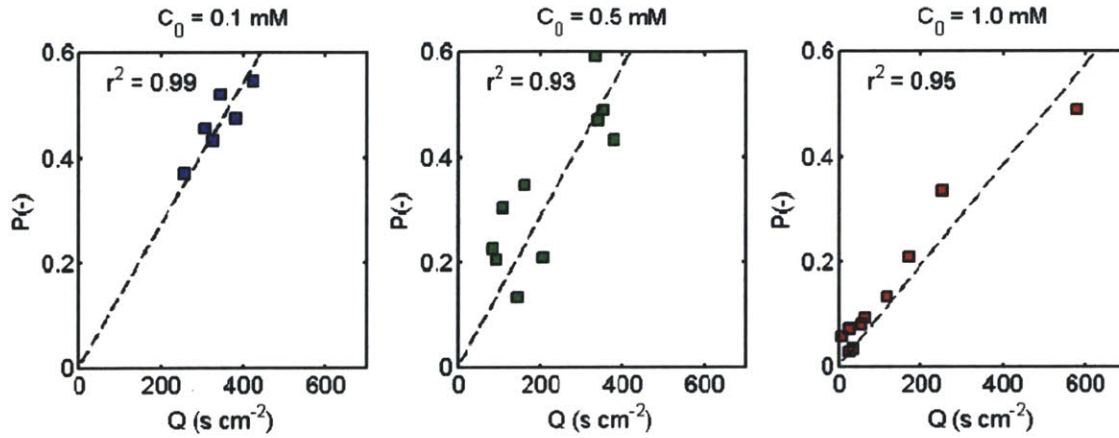
Figure 2.5 Determination of the chemotactic sensitivity coefficient χ_0, for three initial concentrations C_0: (a) 0.1 mM; (b) 0.5 mM; (c) 1.0 mM. Each square represents one experiment. Here $P = \tanh^{-1}(3\pi V_C/8\ v_{2D})$, $Q = \pi/(8v_{2D})[K_D/(K_D+C)^2]dC/dx$ and the slope P/Q corresponds to χ_0 (Eq. 2.10). A least-square linear fit constrained to go through the origin (dashed line) gave $\chi_0 = 13.5\times10^{-4}$, 14.3×10^{-4} and 9.6×10^{-4} cm^2 s^{-1} for the three cases, respectively. The average is $\chi_0 = 12.4\times10^{-4}$ cm^2 s^{-1}.

$(12.4\pm2.0)\times10^{-4}$ cm^2 s^{-1}, showing good agreement between the three sets of data. This is further emphasized by the agreement between the measured chemotactic velocity and its theoretical prediction, plotted in Fig. 2.6 as V_C/v_{3D} vs. χ_0Q, where the experimentally determined mean value was used for χ_0. These results then support the dependence of chemotactic sensitivity on chemotactic velocity derived in Rivero's model.

Having established that the behavioral foundation of the bacterial transport model of Rivero *et al.* [83] is supported experimentally, one can now use the model along with our measured value of χ_0 to predict the chemotactic velocity of *E. coli* towards α-methylaspartate as a function of C and dC/dx [Fig. 2.7(a)]. When $C<<K_D$, increasing values of V_C are related primarily to increases in dC/dx. In these experiments, this regime often occurred near the mouth of the microcapillary, where dC/dx was relatively large and C was low. Conversely, in the region of Fig. 2.7(a) where $C>>K_D$ (corresponding to receptor saturation), $V_C \sim 1/C^2$ and changes in V_C are dominated by changes in C: this regime occurred further into the microcapillary.

2.4.4 Effect of temporal and spatial averaging

This approach for calculating χ_0 relied on both temporal and spatial averaging of the chemoattractant concentration to obtain C and dC/dx. As bacteria experienced local and
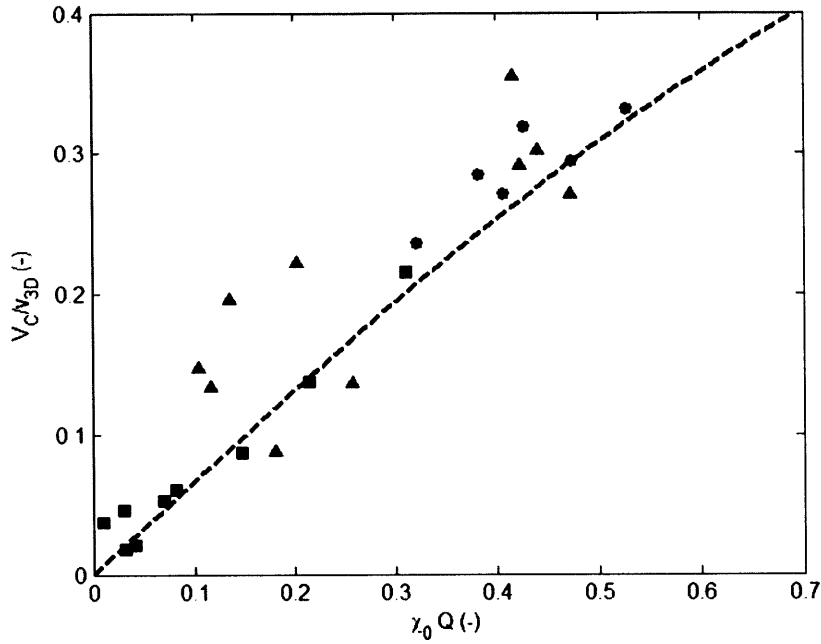
Figure 2.6 Observed values of the relative chemotactic velocity V_C/v_{3D} **of** *E. coli* **towards α-methylaspartate, as a function of** $\chi_0 Q$. $\chi_0 = 12.4 \times 10^{-4}$ cm^2 s^{-1} from the experiments. Symbols correspond to the three initial concentrations $C_0 = 0.1$ (●), 0.5 (▲) and 1.0 mM (■). The highest value of V_C/v_{3D} achieved in our experiments was 0.35. The dashed curve represents the theoretical prediction (Eq. 2.9), which plateaus at V_C/v_{3D} = 2/3 (not shown).

instantaneous concentrations, rather than mean values, it is important to quantify the error associated with these averaging processes. Temporal averaging comes from taking the mean of the concentration profiles from two epifluorescent images recorded ~4 min apart. Comparison of the two images showed that C and dC/dx varied at most by 4.2% and 8.2%, respectively, translating into an error in V_C that is always less than 8.1% and 8.2%, respectively, for all experiments. As for spatial averaging, the use of a constant value of dC/dx was justified because $C(x)$ was nearly perfectly linear ($r^2 > 0.96$) over each 20× field of view. On the other hand, changes in $C(x)$ over a field of view ($L = 600$ μm) could be substantial ($\Delta C = 0.30$ mM for the steepest gradient, $dC/dx = 0.50$ mM/mm). Because Q (Eq. 2.10) is related non-linearly to C [$Q \sim (1+C/K_D)^{-2}$], use of a mean concentration could bias the calculation of χ_0. To investigate this further, the average V_C was computed over the field of view, as $\int_0^L V_C(x)dx/L$, using Eq. 2.9 with a linearly varying $C(x)$ (and $v_{2D} = 29.8$ μm s^{-1}, $K_D = 0.125$ mM, $\chi_0 = 12.4 \times 10^{-4}$ cm^2 s^{-1}).

45
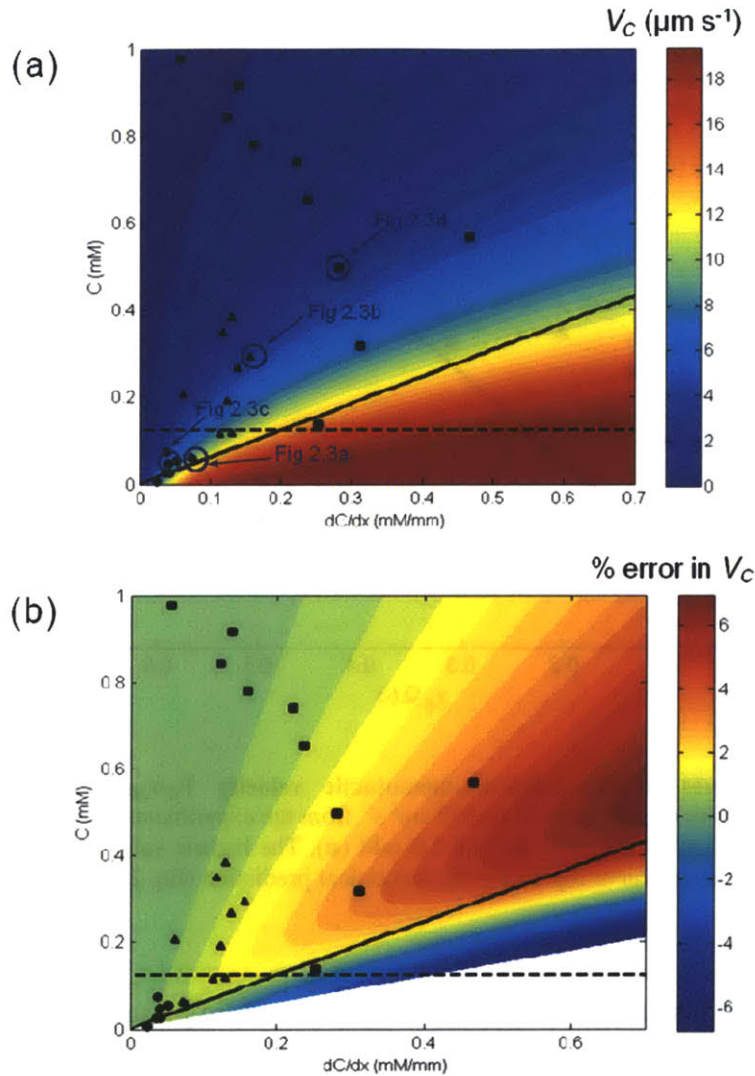
Figure 2.7 Chemotactic velocity and the error incurred in estimating chemotactic velocity as a function of the chemoattractant field. **(a)** The chemotactic velocity V_C of *E. coli* exposed to α-methylaspartate, as a function of the concentration C and concentration gradient dC/dx. V_C was calculated from Eq. 2.9 using the experimentally determined values $v_{2D} = 29.8$ μm s^{-1} and $\chi_0 = 12.4 \times 10^{-4}$ cm^{2}s^{-1}. Symbols represent the experimental runs, separated based on initial chemoattractant concentration ($\bullet$: $C_0 = 0.1$ mM; $\blacktriangle$: $C_0 = 0.5$ mM; $\blacksquare$: $C_0 = 1.0$ mM). Bacterial trajectories corresponding to four cases (circled symbols) are shown in Fig. 2.3. The dashed line indicates $C = K_D$. The solid line represents $C = (dC/dx) \cdot v_{1D}/a_{crit}$ (with $v_{1D} = v_{3D}/2 = 19$ μm s^{-1} and $a_{crit} = 0.03$ s^{-1}). The parameter space below this line represents experimental conditions for which saturation of the adaptation response is expected. Only two points fall below the saturation line. **(b)** The error incurred in estimating V_C (Eq. 2.9) using the mean nutrient concentration C over the entire field of view, expressed as a percentage deviation from the average V_C calculated for a linearly varying concentration profile, as a function of C and dC/dx. Symbols and lines as in (a). The error is <4% for all experiments. In the white region comparison with a linear concentration scenario is not possible, as it would correspond to negative concentrations.

Compared to this value of V_C, the one computed using the mean concentration never differed more than 4% [Fig. 2.7(b)] for these experimental conditions, justifying the use of the mean concentration C in determining χ_0.

2.4.5 Random motility coefficient μ

To fully characterize bacterial transport at the population scale, one further requires the random motility coefficient μ. Measurement of μ for *E. coli* was done by observing the spreading of a band of bacteria. Using a microchannel equipped with a microinjector, a 250 μm wide band of *E. coli* [Fig. 2.8(b)] was generated.
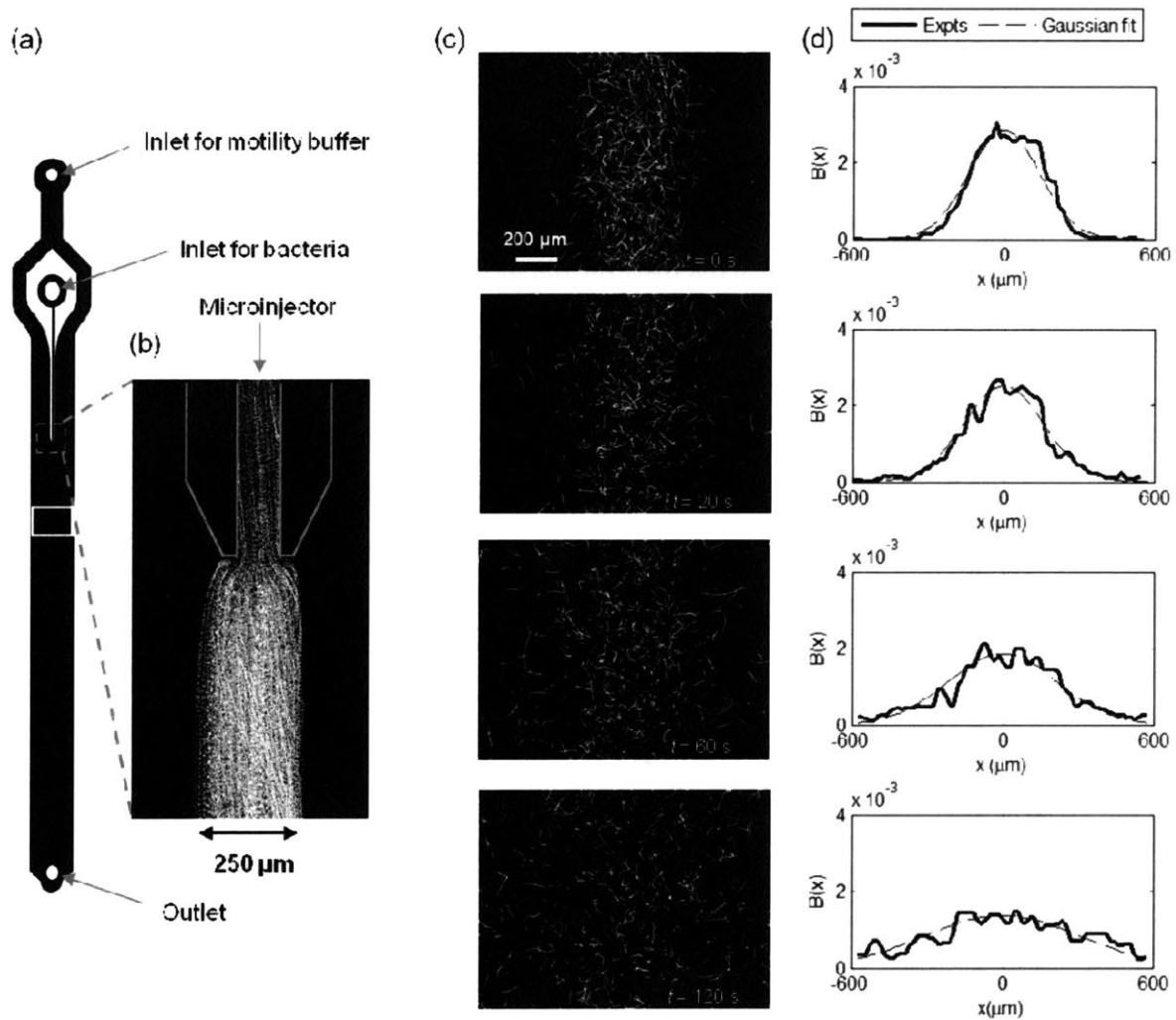
Figure 2.8 Experiments to determine the random motility μ of *E. coli*. (a) Schematic of the microfluidic channel. The observation region is marked by a white rectangle. (b) Close-up of the microinjector, showing the 250 μm wide band of *E. coli*. The image is comprised of 100 frames recorded over 3.1 s and white tracks represent individual bacterial trajectories. (c) Bacterial trajectories at four times after the flow was stopped ($t = 0$), 'releasing' the band of bacteria. Because no chemoattractant is present, lateral spreading is due to random motility alone. Images acquired as in b. (d) Profiles of bacterial positions across the channel, $B(x)$, along with the best Gaussian fit. Each profile was normalized to a total area of 1 and corresponds to the adjacent panel in (c).

47

The experiment started by turning off the flow (at time $t = 0$), causing the bacterial suspension to stop nearly immediately (<3s). The band of bacteria diffused laterally, due to random motility, and the cell distribution $B(x,t)$ across the channel was recorded at a range of times after release of the band. At each observation time t, a 1D Gaussian (Eq. 2.11) was fitted to $B(x,t)$ [Fig. 2.8(d)] and the standard deviation S of the Gaussian was taken as a measure of the lateral width of the bacterial band. The linear increase of S^2 with time [Fig. 2.9] confirmed the diffusive nature of random motility. A linear least-squares fit to $S^2 = 2\mu(t+t_0)$, where $(2\mu t_0)^{1/2}$ is the initial width of the bacterial band, yielded values of μ ranging from 1.8×10^{-6} to 4.8×10^{-6} cm^2 s^{-1} for nine realizations, with an average of $\mu = (3.3 \pm 0.8) \times 10^{-6}$ cm^2 s^{-1}. Negligible differences were observed among the two bacterial batches and for the two different channel depths (50 and 100 μm). In this analysis, effects from side boundaries were ignored because the observation time (2 min) was much shorter than the diffusive time for the bacterial band to reach the sidewalls [~(1.5 mm)^2/(2μ) ~ 56 min]. The mean swimming speed recorded for the random motility experiments was $v_{2D} = 23.3$ μm s^{-1}, somewhat lower than for the chemotaxis experiments.
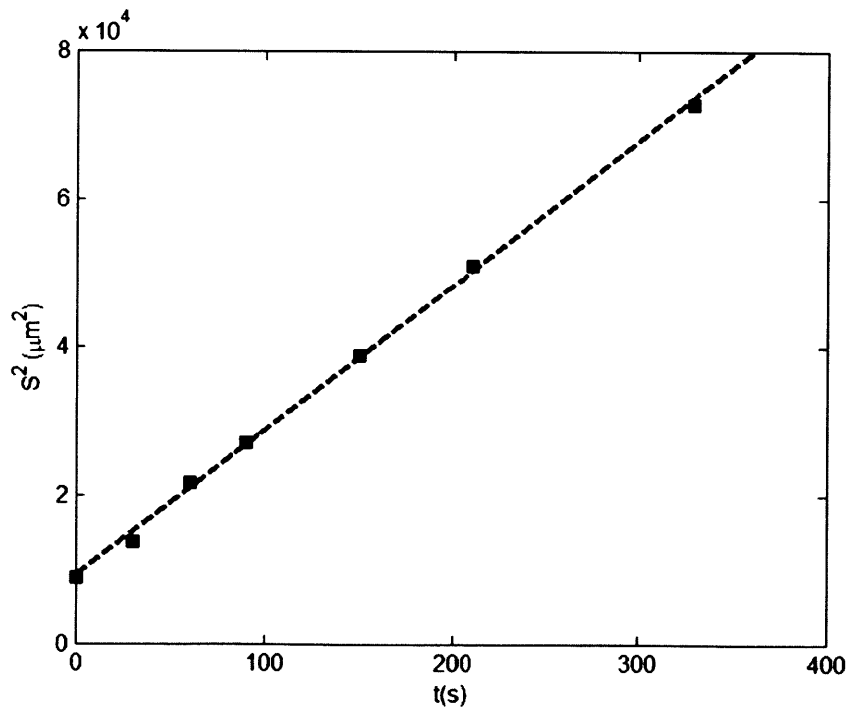
Figure 2.9 Determination of the random motility coefficient from the bacterial distributions. The squared standard deviation S^2 of the across-channel bacterial distribution corresponding to the experiments in figure 2.8(d), as a function of time t elapsed since release of the bacterial band. The dashed line represents the best linear fit and its slope is 2μ. This experiment yielded $\mu = 3.6 \times 10^{-6}$ cm^2 s^{-1}. The average random motility over nine experiments was $\mu = 3.3 \times 10^{-6}$ cm^2 s^{-1}.

2.5 Discussion

In many phenomena, the macroscopic behavior of a system emerges from the aggregate effect of a large number of players acting at smaller scales. It is then convenient to seek averaging procedures to achieve predictive power over the system's behavior without accounting for the microscale details of individual processes. Yet, before confidently doing so, it is both necessary and instructive to test such up-scaling procedures experimentally, to ensure that macroscopic formulations adequately reflect the underlying microscopic dynamics. Furthermore, observations at the scale of individual processes can shed light on additional detail lost in the averaging procedure. In the case of bacterial chemotaxis, the fate of a population emerges from the aggregate behavior of individual cells. The probabilistic model of Rivero et al. [83] provides the mechanistic basis, at the single-cell level, for the population-scale formulation of bacterial transport (Eq. 2.2), which in turn enables one to predict the fate of a bacterial population under arbitrary chemoattractant concentration conditions. Here, microfluidics and single-cell tracking have been used to provide an experimental validation of the behavioral foundation for the mathematical up-scaling at the basis of the bacterial transport equation.

A microfluidic device was used to generate and measure a range of chemoattractant concentrations and concentration gradients, while simultaneously capturing single-cell chemotactic behavior. This enabled the direct determination of the chemotactic sensitivity coefficient χ_0. The observed value of χ_0 was somewhat larger than literature results for *E. coli* exposed to α-methylaspartate (Table 2.1), but in the same order and not statistically different (Students' t-test, $p > 0.05$). Variation in α-methylaspartate concentrations and use of different bacterial batches resulted in less than 50% variation in χ_0, a variability that compares very favorably with the 5- to 7-fold change in χ_0 typically reported for replicate experiments of bacterial chemotaxis [54]. This study, then, provides a quantitative experimental verification of the behavioral basis of the bacterial chemotactic migration model proposed by Rivero et al. [83] and complements their initial validation based on previous population-scale data [101].

These measurements [Fig. 2.6] revealed chemotactic velocities as high as 35% of swimming speed (v_{3D}), larger than most literature values [20, 101, 102]. For example, Berg and Brown [20] measured $V_C = 0.9$ μm s^{-1} = $0.06v_{3D}$ for *E. coli* in aspartate and $V_C = 2$ μm s^{-1} = $0.14v_{3D}$ in serine,

while Dahlquist *et al.* [101] found $V_C = 3.5$ μm s^{-1} = $0.23v_{3D}$ for *Salmonella* in serine. The wider range of V_C/v_{3D} observed here is likely due to the broader set of concentration conditions explored in this setup, while those earlier studies focused on the mechanistic and molecular underpinnings of chemotaxis by working prevalently in shallow gradients.

Table 2.1: Chemotactic sensitivity χ_0 of *E. coli* to α-methylaspartate.

χ_0 (10^{-4} cm^2 s^{-1})	Chemotaxis assay	Reference
7.5	Capillary	[98]
4.1 ± 0.2	SFDC	[103]
2.4 ± 0.6	SFDC	[66]
12.4 ± 2.0	Microfluidic capillary	This study

Fig. 2.7(a) shows that one could in principle attain even higher chemotactic velocities, with a theoretical limit of $V_C/v_{3D} = 2/3$ (Eq. 2.9), by exposing cells to larger concentration gradients. However, when dC/dx is too large the adaptation response of *E. coli* saturates (the adaptation response is the change in counterclockwise bias of motors during an attractant stimulus that varies exponentially in time t from an initial concentration C_0, i.e. $C(t) = C_0\,e^{at}$, where a is the ramp rate) [104]. Using tethered cells, Berg and coworkers [104] found the adaptation response to depend on the ramp rate $a = (1/C) \cdot (dC/dt)$ characterizing the fractional time rate of change in concentration experienced by a bacterium. For $a < a_{crit}$, *E. coli*'s response to chemoattractants is a function of the time rate of change of chemoreceptor occupancy, as in the model of Rivero *et al.* [83] On the other hand, the adaptation response saturates above a critical ramp rate a_{crit}, with $a_{crit} \sim 0.03$ s^{-1} for α-methylaspartate [Fig. 2.7A in [104]]. For $a > a_{crit}$, cells can take seconds to minutes to adapt [99, 105] and the model of Rivero *et al.* [83] is no longer applicable. For a swimming cell, the ramp rate is $a = (dC/dx) \cdot v_{1D}/C$, where $v_{1D} = v_{3D}/2$ [97]. Thus, the response saturates ($a > a_{crit}$) at high concentration gradients dC/dx and low concentrations C. The threshold for saturation ($a = a_{crit}$) can then be expressed as $C = (dC/dx) \cdot v_{1D}/a_{crit}$, a straight line in the $(C, dC/dx)$ space [Fig. 2.7(a)]: below this line, saturation is expected to occur. Fig. 2.7(a) shows that 24 out of 26 of these experiments were conducted in the linear regime of the adaptation response (i.e. above the saturation line), as a result of letting the initial step in concentration diffuse substantially before exposing bacteria to chemoattractants, unlike previous

approaches [55, 61]. Only two data points fall in the saturation regime (below the line), one of them corresponding to the 'outlier' (right-most point) in Fig. 2.5(c). It is noteworthy that, if one removed this data point from the analysis (removal of the second point has no effect), one would obtain $\chi_0 = 12.8 \times 10^{-4}$ cm^2 s^{-1} for $C_0 = 1$ mM [Fig. 2.5(c)], bringing the average to $\chi_0 = (13.5 \pm 0.6) \times 10^{-4}$ cm^2 s^{-1} and further improving the agreement among the three sets of experiments. Finally, the requirement that adaptation should not saturate reduces the maximum predicted value of V_C, which can be computed as the maximum from Eq. 2.9 under the constraint $dC/dx = (1/C) \cdot v_{1D}/a_{crit}$. The new maximum V_C is reduced by a factor $tanh(\chi_0 a_{crit}/4v_{3D})$ compared to the theoretical one $V_C/v_{3D} = 2/3$ and occurs when $C = K_D$ (the intersection between solid and dashed lines in Fig. 2.7(a)). With $\chi_0 = 12.4 \times 10^{-6}$ cm^2 s^{-1} and $v_{3D} = 37.9$ μm s^{-1}, it can be found that $V_C/v_{3D} = 0.38$, which compares favorably with the largest measured value of chemotactic velocity ($V_C/v_{3D} = 0.35$).
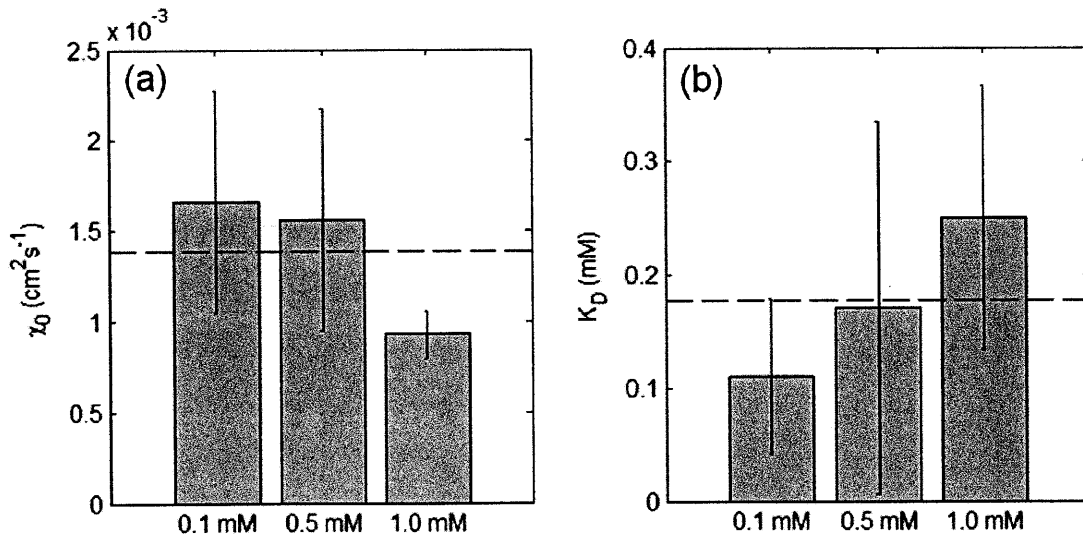
Figure 2.10 Simultaneous determination of χ_0 and K_D by nonlinear fitting. Both χ_0 (a) and K_D (b) can be obtained by non-linear fitting of Eq. 2.9 to the experimental data for the initial conditions $C_0 = 0.1$, 0.5 and 1.0 mM. The dashed line represents the mean of the three sets of experiments and the error bars indicate 95% confidence intervals.

While the quantification of χ_0 in this study was based on previous knowledge of the dissociation constant K_D, the approach is also applicable to bacteria with unknown K_D. In this case, K_D and χ_0 can be determined simultaneously from non-linear least square fitting of Eq. 2.10 to the data.

This has been implemented by simultaneous fitting of K_D and χ_0 for each of the three series of experiments using Matlab's curve-fitting toolbox and report results in Fig. 2.10. While some scatter is apparent in the estimate of χ_0, mean values for both parameters ($\chi_0 = 13.8 \times 10^{-4}$ cm^2 s^{-1}; $K_D = 0.171$ mM) are in good agreement with our earlier estimate of χ_0 (Table 1) and values from the literature for K_D [0.125 mM [98] to 0.160 mM [99]]. This demonstrates that *a priori* knowledge of K_D is in fact not required in estimating χ_0.

It remains to be seen whether Eq. 2.9 is an accurate model for bacteria other than *E. coli*. The up-scaling of simple mechanistic movement rules [83] is generally applicable, but the relation between V_C and C as well as dC/dx (Eq. 2.9) might be specific to *E. coli,* and different functional dependences might be appropriate for other bacteria. Furthermore, Eq. 2.9 does not account for chemokinetic behavior (i.e. changes in swimming speed associated with local concentration conditions). While the swimming speed of *E. coli* was found to be independent of C and dC/dx, other bacteria are known to display chemokinesis [106, 107], and the corresponding term in the model of Rivero *et al.* [83] would then have to be included in the analysis.

Unlike the single-cell approach to determine χ_0, a population-scale approach was used to quantify μ. The reason is that the small depth of focus of traditional microscopy severely limits the duration over which individual bacteria can be tracked. Thus, individual run times (T_0) as well as directional persistence (ψ) – elegantly measured by Berg and Brown [20] with a 3D tracking microscope – are difficult to obtain reliably with a 2D setup. Fortunately, this does not affect the determination of V_C (hence χ_0), as only the swimming speed and the *ratio* of run times β are required in this case (Eq. 2.7), both of which are independent of trajectory duration. The situation is different for μ (Eq. 2.8), which directly depends on average run time (T_0), making a single-cell approach more challenging. To obtain longer trajectories, one could use shallower microchannels, at the expense of increased confinement artifacts, or recently developed 3D visualization techniques, such as defocused particle tracking [108] and digital holographic microscopy [109]. On the other hand, unlike χ_0, μ can easily be determined from population-scale data, as neither concentration gradients nor numerical solutions of the transport equation (Eq. 2.2) are required in this case. Hence, a single-cell approach is primarily of interest for determining χ_0, while μ is best obtained from population-scale methods. Here, this has been

illustrated by one such method by using microfluidics to generate a band of bacteria and tracking its diffusion over time. The value of random motility [$\mu = (3.3\pm0.8)\times10^{-6}$ cm^2 s^{-1}] has been found of magnitude comparable to that obtained from the single cell estimate from Eq. 2.8 ($\mu = 4.2\times10^{-6}$ cm^2 s^{-1}, using $v_{2D} = 23.3$ μm s^{-1} and assuming $T_0 = 1$ s and $\psi = 0.3$), particularly in light of the three orders of magnitude variability in literature values of μ for *E. coli* [$(0.1-72)\times10^{-6}$ cm^2 s^{-1}; [66]], likely associated with differences in bacterial strains, growth and experimental conditions.

This microfluidic capillary assay presents several advantages over traditional chemotaxis assays. First, the laminar nature of the flow [110] prevents mixing except by molecular diffusion and allows fine-scale concentration profiles to be generated and accurately measured, bypassing the need for theoretical predictions. This eliminates the risk of unpredictable perturbations [54] arising from natural [111] or operator-induced convection [102]. Second, the size and transparency of microchannels are optimally suited for microscopy, enabling direct observation of single bacteria and quantification of their chemotactic response by automated image analysis and cell tracking. This method of quantifying chemotaxis bypasses plate counting, which is both time-consuming [1-3 days; [112]] and inaccurate. Third, by relying on single-cell information, one can analyze cultures with lower cell densities (<10^7 cells/ml) compared to population-scale assays [~10^8 cells/ml; [66]], reducing consumption of metabolizable chemoattractants, which generates unpredictable secondary gradients [55, 113]. Fourth, analysis of chemotaxis in a microcapillary accessible only to motile bacteria excludes non-motile cells and debris, unlike previous approaches [54, 66, 81, 114], enhancing the signal-to-noise ratio in the measurements. Fifth, studying chemotaxis under no-flow conditions prevents potential artifacts associated with flow-based gradient generators [89], where hydrodynamic shear might reorient cells [88, 115, 116] and potentially impair chemotaxis [115]. Finally, the use of an unsteady concentration profile allows sampling of a range of gradients within a single experiment. In this respect, steady gradients might allow for greater repeatability, but microfluidic devices that generate steady gradients have only recently been proposed [93, 94, 117] and have seen limited application to bacterial chemotaxis, always at the population scale.

There are two potential drawbacks in the approach used in this study. First, measurements of V_C were based on quantification of bacterial fluxes. For uniform bacterial distributions, the only

53

flux is the one associated with chemotaxis (BV_C in Eq. 2.1), as $dB/dx = 0$: thus, one is justified in calculating V_C from measured bacterial fluxes. In our experiments, however, bacteria moved freely within the microcapillary, giving rise to non-uniform distributions $B(x,t)$. The ensuing diffusive flux of bacteria, $\mu(dB/dx)$, contributed to the total observed flux and could thus have potentially affected our measurement of V_C. It has been verified that this was not the case by comparing diffusive and chemotactic fluxes, and found that in all experiments the diffusive flux was negligible, since $\mu(dB/dx)/(BV_C) < 4 \times 10^{-3} \ll 1$. This was a result of allowing sufficient time for redistribution of bacteria before data collection. Second, the confined microchannel environment could potentially have influenced V_C by affecting bacterial motility. Boundaries are well known to alter motility in complex fashions [56, 118-124]. Although one cannot completely rule out boundary effects on V_C, these are confined to within 5 [125] to 10 [122] μm from boundaries, while the microcapillary depth (60 μm) is twice a typical *E. coli* run length [~30 μm; [126]]. Furthermore, the use of fluorescein as a proxy for chemoattractant concentration holds only for low-molecular-weight attractants: for less-diffusive compounds, one would have to seek fluorescent dyes of higher molecular weight.

In conclusion, it has been shown that single-cell swimming information accurately and reproducibly encodes the parameters governing chemotaxis of a bacterial population, enabling the direct quantification of chemotactic velocity and chemotactic sensitivity for a broad range of chemoattractant concentration conditions. This bypasses the need to fit the bacterial transport equation to observed bacterial distributions. At the same time, the ability to carefully measure the concentration field bypasses the use of theoretical predictions. Thus, this approach removes two key drawbacks (and the associated uncertainties) characteristic of most existing assays. The use of microscopic information provides a complementary approach to study microbial processes compared to traditional population-scale methods, and allows for the experimental verification of the behavioral foundation of chemotactic transport. This, in turn, lends confidence to the predictive use of population-scale models to a wide range of applications, whenever bacteria are exposed to chemically heterogeneous environments. Furthermore, individual-based data can reveal mechanistic details that are not observable at the population scale [127], and important questions in microbial ecology hinge on the behavior of individuals, including cell-cell interactions, quorum sensing [128], predation [16] and resource tracking

[129]. The relevance of single-cell information is directly proportional to the level of resolution at which one wishes to investigate a given process. The quantitative understanding of population-scale processes ultimately emerges from an accurate mechanistic description of the underlying dynamics at the single-cell level. Here novel experimental tools have been used to provide the first experimental verification of the mechanistic processes underlying a macroscopic bacterial transport model. It can be foreseen that, by providing high-resolution information at the behavioral level, microfluidic techniques will trigger a deeper understanding of the ecology of motile microorganisms.

Chapter 3

Bacterial chemotaxis in steady linear and nonlinear microfluidic gradients[a]

3.1 Introduction

The study of chemotaxis hinges strongly on the ability to expose cells to gradients that are quantifiable, controllable and mimic those in natural environments. Although, a range of macroscopic approaches, including capillary assays [130] and stopped-flow diffusion chambers [61] (see Chapter 1) have revealed valuable information on bacterial chemotaxis, the accurate control of gradients at cellular length scales is challenging in such macroscopic devices. In recent years a variety of microfluidic gradient generators have been proposed, leveraging the ability to accurately control fluid flow in the low Reynolds number regime to manipulate and quantify gradients with high accuracy at scales relevant to cells. These microfluidic gradient generators fall into two broad categories, flow-based and diffusion-based. The former can create steady gradients using streams of miscible fluid flowing side by side that can mix only by diffusion in a laminar flow regime typical of a microfluidic environment [6, 86, 89, 90] and gradients of arbitrary shape can be established by appropriately selecting the spatial layout and concentration of multiple adjacent streams. These gradient generators have been used extensively in chemotaxis assays involving surface attached cells like breast cancer [86] and leukemia cells [88, 92] as they can be exposed to steady gradients with small shear forces (provided flow rates are small) and their migration will thus primarily be along the gradient which is established *across* the channel. Chemotaxis of free-swimming cells like bacteria presents different fundamental challenges for the design of microfluidic devices and experiments from those presented by chemotaxis of surface-adherent cells. Hydrodynamic shear can reorient cells [88, 115, 116] and potentially impair chemotaxis [131], making it difficult to distinguish between the active movement due to chemotaxis and the passive movement due to hydrodynamic shear. Also, cells experience temporally varying gradients as they are transported by the flow [6, 89] which can potentially confound measurements. Another disadvantage of flow-based devices for bacterial chemotaxis is the difficulty of obtaining single-cell movement information if one wishes to analyze the swimming kinematics of single bacteria, often with the goal of obtaining a chemotactic velocity [70] Nevertheless, bacterial chemotaxis in flow-based devices can be an excellent approach if one needs to the capture the simultaneous effect of chemical cues and fluid mechanical forces on chemotaxis i.e. the flow-field is an integral part of the problem to be studied. On the other hand, when one is interested in chemotaxis in the absence of flow, diffusion-based gradient generators are more preferable. While even flow-
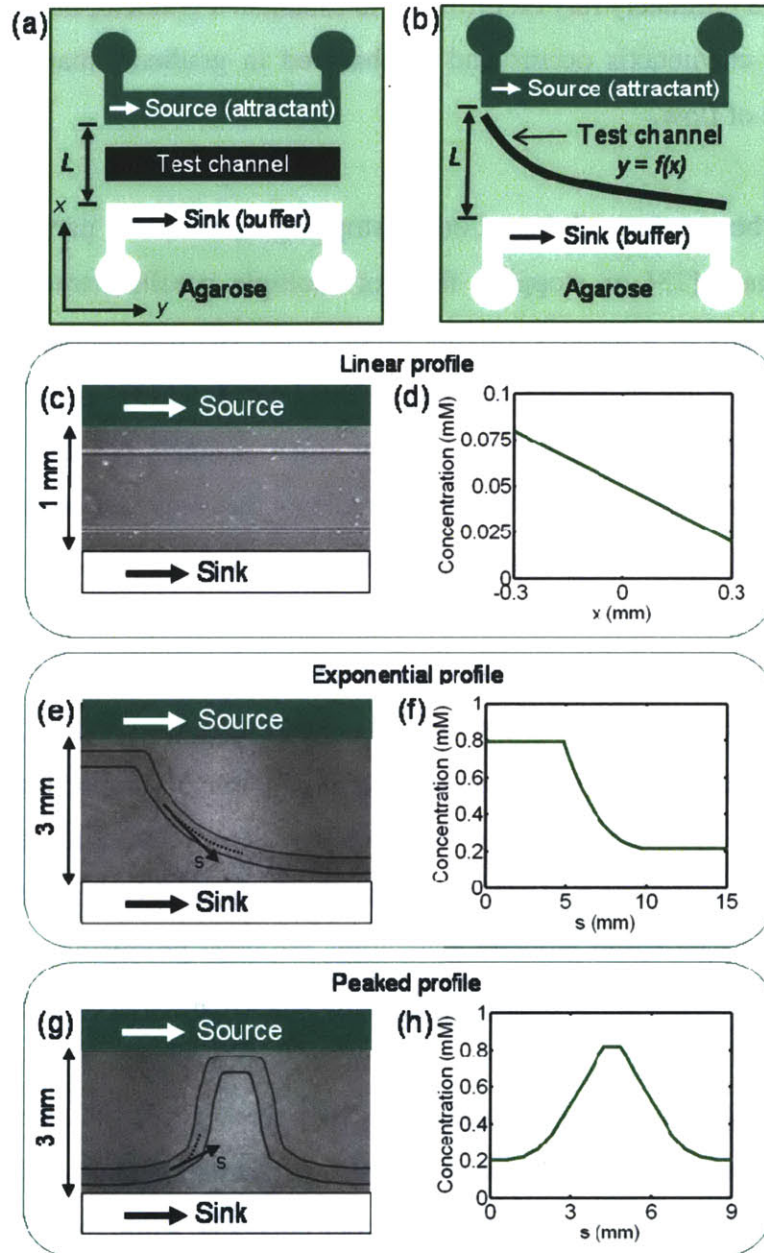
Figure 3.1 Microfluidic devices to generate steady linear and nonlinear gradients (a,b) Schematic planar layouts of a class of diffusion-based microfluidic gradient generators for (a) linear and (b) nonlinear gradients. Constant-concentration boundary conditions in the source channel (flowing chemoattractant) and sink channel (flowing buffer) generate a steady gradient in the test channel by diffusion through the underlying agarose layer. L is the distance between the 'feeder' channels (i.e. source and sink channels), measured between their inner walls facing towards the test channel. The direction of the gradient (s) corresponds to the x axis in this case. **(c,d)** Microdevice to study chemotaxis in linear gradients. (c) Micrograph illustrating planar layout (source and sink channels are shown schematically in green and white, respectively) and (d) numerically computed concentration profile across the test channel, for source and sink concentrations of 0.1 and 0 mM, respectively. **(e)-(h).** Microdevices to study chemotaxis in nonlinear gradients. (e,g) Micrographs showing the planar layout of the microdevices to create an exponential and a peaked concentration profile, respectively. s denotes the coordinate along the test channel. (f,h) Concentration profiles along the channels in (e) and (g), respectively, computed numerically from the shape of the microchannels. The source and sink concentrations were 1 and 0 mM, respectively.

59

based gradient generators ultimately rely on diffusion to establish a gradient, the term 'diffusion-based' emphasizes that chemotaxis occurs and is observed in gradients that evolve only by diffusion, in the absence of flow.

Three approaches have been proposed, based on (i) stopping flow of two parallel streams, one containing chemoattractant [73] or stopping flow of multiple parallel streams, the streams containing chemoattractants in a linearly varying order [132], (ii) maintaining a gradient in a quiescent fluid chamber by use of source and sink microchannels [133], or (iii) maintaining a gradient across a hydrogel layer using source and sink microchannels [93, 94, 134, 135]. The first approach by Seymour *et al.* produces unsteady gradients that only last minutes and is most suitable to study chemotaxis towards ephemeral chemical patches [14, 136, 137]. In this case, the unsteadiness represented a real feature of an environmental signal, as in the nutrient pulses often experienced by marine bacteria [14, 138]. In the device by Jeon *et al.*, if operated on short timescales, the gradient can be considered steady to a good approximation [132] and can be useful if the characteristic times of bacterial sensing is are much smaller than the gradient relaxation time-scale. The second approach exposes cells to steady two-dimensional gradients and has been tested only qualitatively [133]. However, the focus of this chapter is on the third approach which uses hydrogel-based gradient generators, the most promising to study bacterial chemotaxis because of the flexibility in creating arbitrarily shaped gradients without flow.

Hydrogel-based gradient generators rely on the use of two parallel 'feeder' microchannels (the 'source' and 'sink' channels), between which, a third 'test' channel containing the cells is laid out [Fig. 3.1]. A constant flow rate is applied in the feeder channels, while there is no flow in the test channel. The source channel carries a solution of chemoeffector, while the sink channel typically carries buffer. The chemoeffector diffuses across the hydrogel from the source to the sink. This creates a steady concentration profile in the hydrogel, because the feeder channels provide constant-concentration boundary conditions. The characteristic time to set up the gradient, $T \sim L^2/(2D)$, is determined by the diffusion of the chemoeffector (of diffusivity D) across the distance L between the feeder channels. Because the test channel is in direct contact with the hydrogel, its concentration profile reflects the concentration in the underlying hydrogel. This enables the generation of arbitrarily shaped gradients by appropriately configuring the

planar layout of the test channel [135]. After the gradient is established in the hydrogel, cells are injected in the test channel. The gradient in the test channel is rapidly generated over a time scale $T_H \sim H^2/(2D)$, determined by the diffusion of the chemoeffector across the height H of the test channel. For small molecules ($D = 5\times10^{-10}$ m^2 s^{-1}) diffusing across a 100 μm deep test channel, $T_H = 10$ s. A commonly used hydrogel is agarose (often at ~3% w/v), which is highly transparent in thin (~1-3 mm) layers, biocompatible, can be molded to form microchannels, and is quick and easy to assemble because of its thermal gelation properties [134]. The diffusivity of small molecules in agarose is the same as in water [93].

Several implementations of hydrogel-based microfluidic gradient generators have been proposed. Channels can be fabricated in the hydrogel [67, 93, 94] or in a PDMS layer attached to a hydrogel slab [135]. The latter system has been used to generate arbitrarily shaped gradients by fabricating test channels with the appropriate planar layout [135] and has been tested for surface attached cells [139]. These devices are extremely promising to study bacterial chemotaxis, yet their performance as chemotaxis assays has rarely been assessed quantitatively in terms of the bacterial response [93, 94] and to date no bacterial chemotaxis studies have been performed in steady, nonlinear microfluidic gradients. In this chapter, three hydrogel-based gradient generators have been compared and an optimal design has been selected and applied to quantify the chemotactic response of *Escherichia coli* to linear and nonlinear chemoattractant gradients. To determine the applicability of these microdevices as chemotaxis assays, a relevant metric for chemotactic performance – the quantitative cell distribution along a chemical gradient has been used and it is compared with predictions from a mathematical model.

3.2 Materials and Methods

3.2.1 Bacterial strain and chemoattractant

Escherichia coli AW405 (gift of H. Berg), a strain considered wild type for chemotaxis [140] and having a typical length of 2 μm has been used. Bacteria were grown in Tryptone Broth (1% tryptone, 0.5% sodium chloride) at 34°C on an orbital shaker (220 rpm) to mid-exponential phase ($OD_{600} = 0.4$), then washed twice by centrifugation at 2000g for 5 min and resuspension of the pellet in motility buffer (10 mM potassium phosphate buffer, 0.1 mM EDTA, 10 mM NaCl;

pH = 7). The suspension was then diluted 1:5 in motility buffer, achieving a cell concentration of 4×10^7 cells/ml in the microchannel (quantified by counting cells in a 20× field of view, measuring $600 \times 450 \times 28 \ \mu m^3$). The chemoattractant α-methylaspartate (Sigma-Aldrich, USA), a non-metabolizable analog of aspartate [53], was diluted in motility buffer to final concentrations of 0.1 or 1.0 mM in the source channel. Motility buffer without attractant was flowed in the sink channel. To characterize the concentration field by confocal microscopy, a solution of 100 μM fluorescein (Sigma-Aldrich, USA) was flowed in the source channel. Fluorescein has a diffusion coefficient of $5 \times 10^{-10} \ m^2 \ s^{-1}$, nearly identical to α-methylaspartate ($5.5 \times 10^{-10} \ m^2 \ s^{-1}$ ([66])) and its concentration field is thus a good proxy for that of α-methylaspartate.

3.2.2 Design and microfabrication of gradient generators

Three configurations of a hydrogel-based gradient generator, having a 1 mm thick agarose layer sandwiched between a glass slide and a PDMS (Polydimethylsiloxane; Sylgard 184; Dow Corning, MI, USA) layer (above) were studied. The microdevices used to generate steady linear gradients consisted of three parallel channels [Fig. 3.1], each 600 μm wide. In design 1, all three channels were patterned in the PDMS layer [Fig. 3.2(a)]. In design 2, they were patterned in the agarose layer [Fig. 3.2(b)]. In design 3, the feeder channels were patterned in agarose and the test channel in PDMS [Fig. 3.2(c)]. The test channel was separated from the source and sink channels by a 200 μm wide layer of PDMS [Fig. 3.2(a,c)] or agarose [Fig. 3.2(b)], resulting in an edge-to-edge distance between source and sink channels of $L = 1$ mm. The devices used to create nonlinear gradients had a 400 μm wide test channel, and 600 μm wide source and sink channels parallel to each other and separated by $L = 3$ mm (edge to edge). The depth of the source and sink channels was 100 μm in all cases. The depth of the test channels was 100 μm in designs 1 and 2, and 50 μm in design 3 and for the nonlinear gradient devices.

Channels were designed using CAD software (Autodesk Inc., CA, USA) and printed onto transparency film with a high-resolution image setter (Fineline Imaging, CO, USA). Microchannels were fabricated by prototyping against a silicon master with positive relief features, fabricated using standard soft lithography techniques [64]. PDMS layers with embossed channels [Fig. 3.2(a,c)] were obtained by molding against the silicon master, baking at 65°C for 12 hr, peeling off the hardened PDMS, cutting it to size, and punching access holes

using a 20 gauge sharpened luer tip (BD, NJ, USA). The agarose layer was made from a 3% (w/v) solution of Ultra Pure Agarose (Invitrogen, CA, USA) in motility buffer, heated for 30 s in a 1250 W microwave oven, poured, allowed to gel at room temperature, cut to size, and used immediately or stored in motility buffer. Pouring occurred over a flat surface (a Petri dish) to obtain unpatterned agarose slabs [Fig. 3.2(a)], and over the silicon master to obtain patterned agarose layers [Fig. 3.2(b,c)]. Flexible polyethylene tubing (Cole-Parmer USA; inner/outer diameter = 0.5/1.5 mm) and metal connectors (New England Small Tube Corp, NH, USA; inner/outer diameter = 0.43/0.64 mm) were used to connect the inlets of the source and sink channels with two 0.5 ml glass syringes (Hamilton Company, NV, USA), driven by a syringe pump (PHD 2000, Harvard Apparatus, MA, USA), and the inlet of the test channel with a 1 ml plastic syringe (BD, NJ, USA), operated manually.
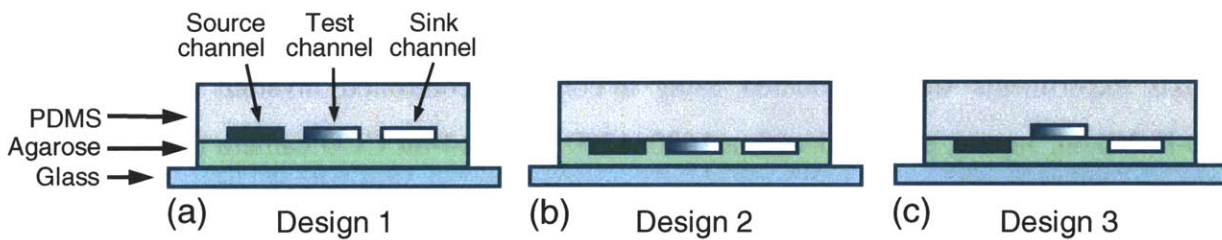
Figure 3.2. Schematic vertical cross-sections of three different designs of the diffusion-based microfluidic gradient generator. The designs differ in the arrangement of the source, sink and test channels within the agarose and PDMS layers. **(a)** Design1, with all three channels in the PDMS layer. **(b)** Design 2, with all three channels in the agarose layer. **(c)** Design 3, with source and sink channels in the agarose layer, test channel in the PDMS layer. In all designs, the test channel was separated from the feeder (i.e. source and sink) channels by a 200 μm wide layer of PDMS (a,c) or agarose (b), resulting in an edge-to-edge distance between the feeder channels of $L = 1$ mm. The intensity of the green shading is illustrative of the chemoattractant field in the channels (shown quantitatively in Fig. 3.4).

3.2.3 Device operation and data acquisition

The agarose layer was simply placed on the glass slide (not bonded) and the PDMS layer was placed on the agarose manually, by exerting gentle pressure until achieving reversible bonding. To avoid delamination of the agarose–PDMS interface, fluid flow through the channels was driven by application of negative, rather than positive pressure, eliminating the need for an external clamping device

In experiments to measure fluorescein concentration profiles an inverted microscope (Zeiss Axiovert 200M) equipped with a confocal laser-scanning unit (Zeiss LSM 510 META) was used.

The 488 nm line of the unit's Argon laser was focused through a 10× objective to excite fluorescein, and fluorescence emission reflected by the dichroic beam splitter (HFT 488 or HFT UV/488/543/633) was collected by a photomultiplier through a 505 nm long-pass filter and a variable pinhole adjusted to 70 μm diameter.

For chemotaxis experiments, a bacterial suspension was manually injected in the test channel by gentle pressure, after a time sufficient for the concentration field to become steady in the agarose layer. Then, the inlet and outlet of the test channel were sealed, using drops of heated, liquid agarose or small PDMS blocks, to prevent residual flow in the channel and evaporation. Without this seal perfect no-flow conditions could not be maintained, which are essential for these experiments. Flow in the source and sink channels was driven by the syringe pump at a constant flow rate of 1 μl/min for the duration of each experiment.

Chemotaxis experiments were conducted using a computer-controlled inverted microscope (TE2000-E, Nikon, Japan), equipped with a 1600×1200 pixel, 14-bit CCD camera (PCO 1600, Cooke, MI, USA). Bacteria were observed at channel mid-depth, using phase contrast microscopy and a 20× extra-long-working-distance objective. To obtain the spatial distribution of bacteria for the linear gradient experiments, three sequences ('movies') of 300 frames were captured at 9.4 frames/s every 5 min, starting 10 min after injection of bacteria in the test channel. Comparison of the bacterial distribution among movies ensured that steady state had been achieved. Long-time-exposure images were obtained from each movie, by locating the maximum pixel intensity for each pixel over the duration of the movie. Furthermore, image analysis was performed by subtracting each frame from the following one, to focus only on motile cells, and by subsequently locating bacteria in each frame as peaks in a monochrome intensity field, using IPlab (BD, MD, USA). Bacterial positions were determined over all frames in a movie and binned to yield the cell concentration profile $B(s)$ along the direction of the gradient, with MATLAB (The Mathworks, MA, USA). Bacterial swimming speeds were computed with an in-house cell tracking software (BacTrack), as described previously[70]. The population-average speed ($V = 28$ μm s^{-1}) was determined as the mean over all motile cells and represents a two-dimensional projection of the three-dimensional swimming speed.

Nonlinear gradients consisted in a peaked profile and an exponential profile, each flanked by two flat-profile regions [Figs. 3.1 and 3.6]. Data were collected 1 hr after injection of the bacteria. Bacterial positions were obtained as above. The microscope stage was translated successively over a series of positions along the channel, in rapid sequence, and a movie (200 frames at 30 frames/s) was acquired at each position. 15 and 25 such movies were used to cover a length of 9 and 15 mm along the test channel for the peaked and exponential profiles, respectively. The data collection sequence lasted <10 min.

3.2.4 Mathematical model

A mathematical model was used to compute the concentration field and bacterial distribution in the test channel. The concentration field $C(x,z)$ of chemoattractant (or fluorescein) in a vertical cross-section xz of each microdevice was modeled by solving the two-dimensional, steady-state diffusion equation, $D(\partial^2 C/\partial x^2 + \partial^2 C/\partial z^2) = 0$, in a domain comprising the hydrogel and the test channel (with the appropriate geometry for each design), using a finite element software (COMSOL Multiphysics, MA, USA). The edges of the source and sink channels were modeled as constant-concentration boundary conditions, while a no-flux condition was implemented at domain boundaries in contact with PDMS or glass. The distribution of bacteria, $B(s)$, along a microchannel that is arbitrarily oriented in the xy plane was modeled using the bacterial transport equation (Eqs. 2.2 and 2.9, see Chapter 2) [70, 83, 96]. Rewriting these equations for the longitudinal coordinate along the microchannel, s in the xy plane:

$$\frac{\partial B}{\partial t} = \frac{\partial}{\partial s}\left(\mu \frac{\partial B}{\partial s}\right) - \frac{\partial}{\partial s}(V_c B), \qquad (3.1)$$

$$V_c = \frac{8V}{3\pi} \tanh\left(\frac{\chi_0 \pi}{8V} \frac{K_D}{(K_D + C)^2} \frac{dC}{ds}\right), \qquad (3.2)$$

In this case, C and dC/ds were determined from the solution of the diffusion equation, the swimming speed V was measured as described above and the receptor/ligand dissociation constant K_D was assumed to be 0.125 mM [98]. No-flux boundary conditions were applied at the channel sidewalls. The random motility coefficient μ and the chemotactic sensitivity coefficient χ_0, which measures the diffusivity of the bacterial population and the strength of chemotaxis of

the cells respectively, were obtained by non-linear chi-square estimation (see the following section).

3.2.5 Non-linear chi-square fitting and error analysis

Nonlinear chi-square estimation and parameter uncertainty estimation were performed by standard procedures [141]. The merit function to be minimized in chi-square fitting is the sum of squared errors weighted by the estimated variance of each data point. To obtain these variance estimates, 1,000 Monte Carlo re-samplings of the experimentally determined bacterial distribution, $B(s)$, were carried out and the variance was computed in the sampled values of each bin explicitly. The data was fitted by minimizing the chi-square merit function, computed using these variance estimates. This yielded best-fit values for the parameters μ and χ_0 that minimize chi-square. To obtain confidence intervals for these values of μ and χ_0, the local parameter space near the chi-square minimum was sampled by systematically varying one parameter while holding the other fixed. The local curvature in the chi-square landscape was then used to compute the displacement in the parameter required to increase chi-square by 4, the 95% confidence limit of the chi-square distribution with one degree of freedom. The procedure was repeated for both of the parameters, μ and χ_0.

3.3 Results

3.3.1 Gradient characterization

Diffusion from the source (carrying a concentration C_0) to the sink (carrying a buffer solution) establishes a concentration gradient across the agarose. Common to all three designs, the flow-through configuration of the feeder channels eliminates the need for open-air reservoirs [135] and their periodic replenishment to maintain the gradient. When the feeder channels are far apart compared to the agarose thickness, the hydrogel domain is nearly one-dimensional and solution of the diffusion equation yields the linear concentration profile $C(x) = xC_0/L = xG_E$, where $G_E = C_0/L$ is the magnitude of the predicted one-dimensional gradient.

Confocal laser scanning microscopy was used to measure $C(x)$ [Fig. 3.3(a)-(c); see section 3.2.3]. Buffer was flowed at 1 μl/min in the feeder channels, with addition of 100 μM

fluorescein to the source channel. After the initiation of the feeder flows, a 30 min period was allowed for the concentration field in the agarose to be established (for $L = 1$ mm this occurs over $T \sim L^2/(2D) = 17$ min). Then, buffer was injected in the test channel to mimic injection of a
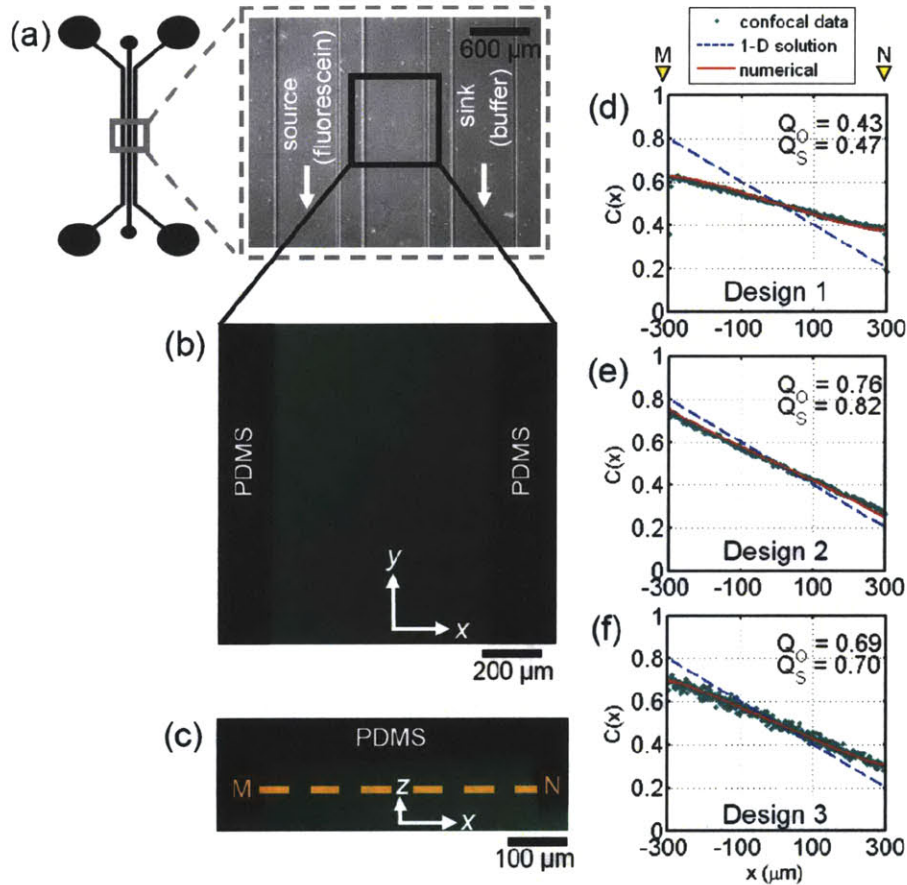
Figure 3.3 Gradient characterization of the steady linear gradient generator. (a) Planar layout of the microdevice to generate a steady linear gradient (schematic and micrograph). (b) Confocal image showing fluorescence at mid-depth in the test channel for the planar section defined by the black box in (a). 100 μM fluorescein was added to the source channel (shown in (a)). (c) Vertical line-scan of the test channel taken along the centerline of the same region. The dashed line MN indicates mid-depth and corresponds to the image in (b). (d)-(f) Concentration profiles across the width of the test channel, at channel mid-depth, for designs 1 (d), 2 (e), and 3 (f) (see Fig. 3.2). The green dots are confocal data for fluorescence intensity, obtained along the mid-depth cross-section of each test channel (line MN in (c)). The red lines are numerically modeled profiles, taken along MN in Fig. 3.4(a)-(c), respectively. Triangular markers labeled M and N indicate the corresponding points in panel (c) and Fig. 3.4(a)-(c). The blue dashed line corresponds to the one-dimensional solution, i.e. the profile predicted if concentration decayed linearly between source and sink. Q_O measures the ratio of the magnitudes of the experimentally observed gradient and the predicted one-dimensional gradient. Q_S measures the ratio of the magnitudes of the numerically computed gradient and the predicted one-dimensional gradient. $C(x)$ represents concentration normalized by the concentration in the source channel.

cell suspension and measurements started within minutes. Concentration profiles $C(x)$ recorded at channel mid-depth [Fig. 3.3(d)-(f), green dots] were highly linear. A linear least-squares fit to

$C(x)$ within the test channel yielded the magnitude of the experimentally observed gradients, G_O, and confirmed the linearity of the gradients ($r^2 > 0.98$ for all three designs). Importantly, G_O was found to be considerably lower than G_E [Fig. 3.3(d)-(f), dashed blue line] and differed among the
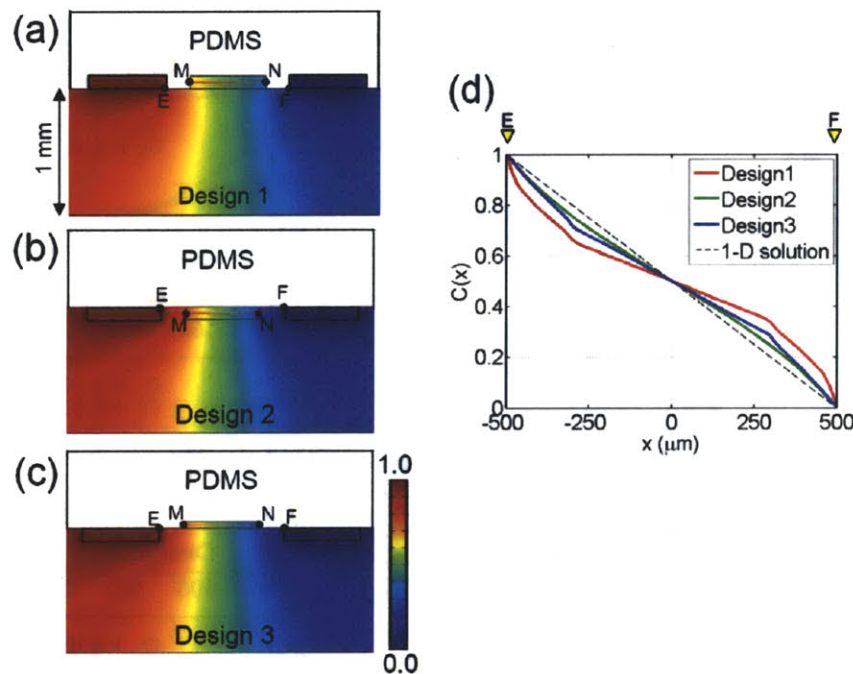
Figure 3.4 Numerical simulation of the concentration field in the agarose layer of the steady linear gradient generator. (a)-(c) Numerically modeled concentration fields in the agarose layer and in the test channel (middle channel in each panel) for designs 1 (a), 2 (b), and 3 (c) (see Fig. 3.2). Transects EF and MN indicate cross sections at the top of the agarose layer and at mid-depth in the test channel, respectively, and correspond to the numerically modeled concentration profiles plotted in panel (d) and in Fig. 3.3(d)-(f), respectively. (d) Numerically modeled concentration profiles, $C(x)$, at the top of the agarose layer, along lines EF in panels (a)-(c). Triangular markers labeled E and F indicate the corresponding points in panels (a)-(c). The dashed line is the one-dimensional solution, i.e. the profile predicted if concentration decayed linearly between source ($x = -500$ μm) and sink ($x = 500$ μm). These profiles show that the concentration profile in the agarose layer is not linear and that the departure from linearity is design-dependent. In all cases, concentrations were normalized by the concentration in the source channel.

designs. The ratio of the magnitudes of the experimentally observed gradient and the predicted one-dimensional gradient, $Q_O = G_O/G_E$, was 0.43, 0.76 and 0.69 for designs 1, 2 and 3, respectively.

Numerical simulations of the diffusion equation (Section 3.2.4) showed good agreement with measured profiles [Fig. 3.3(d)-(f), red line]. Linear least-squares fitting of the simulated concentration profiles within the test channel yielded the magnitude of the numerically computed gradient, G_S, and confirmed that gradients were highly linear ($r^2 > 0.99$ for all three

designs). The ratio of the magnitudes of the numerically computed gradient and the predicted one-dimensional gradient, Q_S $=G_S/G_E$, was 0.47, 0.83 and 0.70 for designs 1, 2 and 3, respectively, in close agreement with the observed ratios, Q_O. These results imply a steeper decay profile in the regions flanking the test channel, since the magnitude of the gradient averaged over the entire distance from the source channel to the sink channel must still be equal to G_E, to satisfy conservation of flux. This was confirmed by numerical simulations of $C(x)$ at the top of the agarose layer [Fig. 3.4]: while $C(x)$ is linear *within* the test channel, it is flanked by nonlinear regions where the magnitude of the gradient is greater than G_E. This nonlinearity is more pronounced in design 1, consistent with the lower value of Q_O and Q_S.

These findings show that the magnitude of the chemoeffector gradient within the test channel will be less than G_E (by up to 50%) and the geometry of the system must be accounted for in determining the actual gradient magnitude. This was not recognized in previous studies that reported $Q_O = 1$ based on wide-field fluorescence microscopy measurements [93, 94]. The latter, however, is inappropriate for accurate characterization of the test-channel gradients because the out-of-plane fluorescence from the agarose layer, which is considerably thicker than the test channel, can override that of the test channel. This has been confirmed by applying wide-field microscopy and also recovering $Q_O = 1$. This points to the importance of accurately quantifying the gradient through cross-sectional imaging and mathematical modeling.

This analysis leads us to select design 3 as the best choice for bacterial chemotaxis applications, for two reasons. First, design 3 establishes a gradient whose magnitude is closer to G_E compared to design 1. Second, design 3 enables the fabrication of more complex designs for the test channel compared to design 2, because patterning occurs in the PDMS as opposed to the agarose. Fabrication of deeper channels (~500 μm) was also found to be easier in PDMS than agarose, which tends to get torn when peeled off from the silicon master if thick. The chemotaxis experiments that follow will thus be based on the configuration in design 3.

3.3.2 Chemotaxis in a linear gradient

chemotaxis experiments in linear concentration profiles were performed by exposing the bacteria *Escherichia coli* AW405 to gradients of α-methylaspartate, a non-metabolizable analog of

aspartate [53]. Gradients were created by flowing 0.1 or 1.0 mM α-methylaspartate in the source channel and buffer in the sink channel. After a time sufficient to reach a steady concentration field in the agarose (~17 min), a bacterial suspension was manually injected in the test channel by gentle pressure. Bacteria were filmed at channel mid-depth, using a computer-controlled inverted microscope equipped with a CCD camera. From movies both long-time-exposure images of the bacterial distribution and positions of individual bacteria were obtained. The latter were binned to yield the cell concentration profile along the gradient (see section 3.2.3).
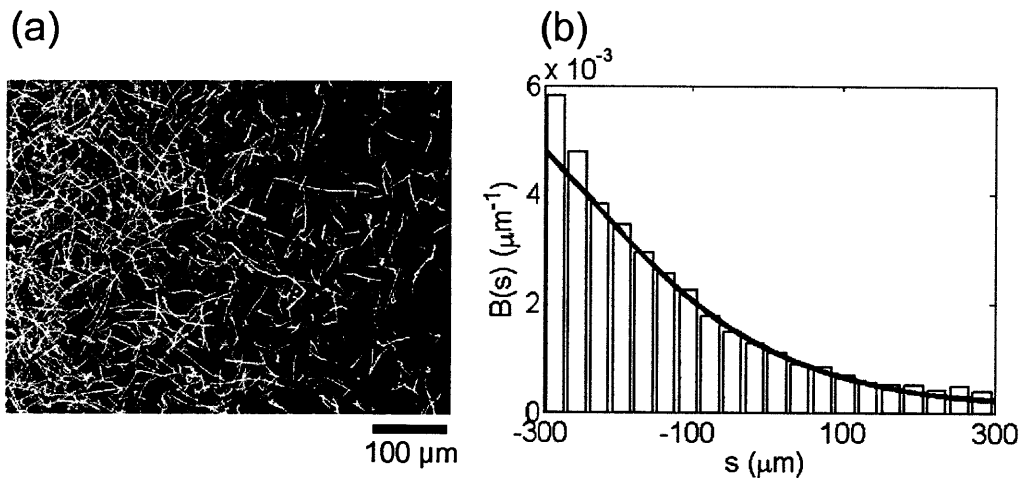
Figure 3.5 Chemotactic response of the bacteria _E. coli_ to a linear gradient of α-methylaspartate. A constant flow (1 μl/min) was maintained in the source and sink channels, containing 0.1 mM α-methylaspartate and motility buffer, respectively (see Fig. 1(c) for the microdevice layout). This corresponds to a predicted one-dimensional gradient magnitude $G_E = 0.1$ mM/mm and an actual gradient magnitude $G_O = 0.069$ mM/mm (since $Q_O = 0.69$, see text). **(a)** Long-time-exposure image, recorded over 9.4 s, showing trajectories of _E. coli_ cells. Note the accumulation of cells in the highest concentration region, on the side of the test channel closest to the source channel (left). **(b)** Normalized distribution of _E. coli_ cells along the gradient, $B(s)$, from the experiments (bars) and the numerical model (line). The model result is the solution of the bacterial transport equation (Eqs. 3.1, 3.2) for μ = 5.9×10^{-6} cm^2 s^{-1} and $\chi_0 = 5.0 \times 10^{-4}$ cm^2 s^{-1}. $B(s)$ was normalized so as to have an area of 1.

Flagellar rotation enables _E. coli_ to swim, and switching between clockwise and anti-clockwise rotation results in tumbling (directional change) and smooth swimming, respectively. An increasing attractant concentration causes a suppression of tumbling [142] depending on the temporal change of attractant experienced by a swimming cell. The result is a net migration towards higher attractant concentrations [83]. In linear gradients, cells indeed accumulated near the edge of the test channel closest to the source channel [Fig. 3.5(a)], resulting in a strongly skewed steady-state bacterial distribution [Fig. 3.5(b), bars].

70

To test the performance of the gradient generator in the chemotaxis assay, the observed bacterial distribution was compared with that predicted from a mathematical model (section 3.2.4). The model computes the concentration field in the test channel, C, by solving the diffusion equation, and the distribution of cells, B, by solving the bacterial transport equation [70, 83, 96]. The bacterial transport equation has previously been used as a model to fit data from population-scale measurements in order to quantify the intensity of random motility and chemotaxis [61, 78].

For the linear gradient generator [Fig. 3.1(c)], the direction of the gradient s corresponds to x and the chemoattractant concentration profile $C(x)$ is shown in Fig. 3.1(d). The observed bacterial distribution was strongly skewed towards higher chemoattractant concentrations [Fig. 3.5(b)]. Nonlinear chi-square fitting and uncertainty analysis of the random motility and chemotaxis parameters, μ and χ_0, with the observed bacterial distribution yielded $\mu = (5.9 \pm 0.7) \times 10^{-6}$ cm^2 s^{-1} and $\chi_0 = (5.0 \pm 0.7) \times 10^{-4}$ cm^2 s^{-1} (the error bounds represent 95% confidence intervals). The best-fit values provide an accurate description of the observed bacterial distribution [Fig. 3.5(b), solid line] and are in general agreement with recently reported values for chemotaxis of E. $coli$ AW405 towards α-methylaspartate [66, 70] ($\mu = (3.3-3.8) \times 10^{-6}$ cm^2 s^{-1}; $\chi_0 = (2.4-12.4) \times 10^{-4}$ cm^2 s^{-1}), particularly in view of the sensitivity of motiliy and chemotaxis to small changes in growth and experimental conditions [54, 61, 66, 68].

3.3.3 Chemotaxis in nonlinear gradients

Fabrication of test channels with appropriate planar layouts enables the generation of steady, arbitrarily-shaped gradients [135]. The response of E. $coli$ to two types of nonlinear concentration profiles was investigated: an exponential profile connecting two constant-concentration regions [Fig. 3.1(e)] and a peak in concentration [Fig. 3.1(g)]. In both cases, the distance L between the feeder channels was 3 mm, resulting in a gradient set-up time of $T = 2.5$ hr. Although this design necessarily yields a finite gradient in the transverse direction across the channel, the gradient experienced by swimming cells is primarily in the longitudinal direction, parallel to the channel walls, because of the relatively narrow channel width (400 μm). The concentration gradient seen by the cells is therefore well approximated by dC/ds [Fig. 3.1(e,g)]. If the shape of the microchannel's centerline is $y(x)$, the concentration profile and its gradient along the channel are $C(s) = G_0 \int (1+y_x^2)^{-1/2} ds$, $dC/ds = G_0 (1+y_x^2)^{-1/2}$, where $y_x = dy/dx$ [135]. The

distribution of *E. coli* cells was recorded 1 hour after injection in the test channel, by rapidly translating the microscope stage along the channel and acquiring a movie at each of 15 (exponential profile) and 25 (peaked profile) positions.
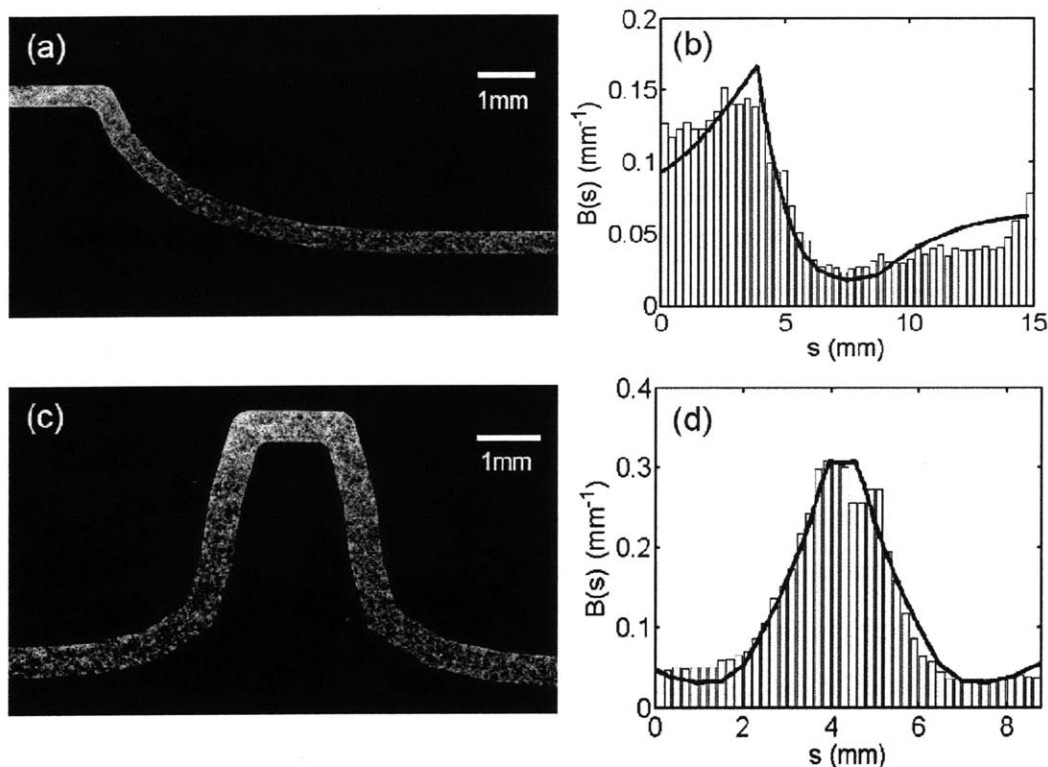
Figure 3.6 Response of *E. coli* to an exponential and a peaked concentration profile of α-methylaspartate. The concentration of α-methylaspartate in the source and sink channels was 1 and 0 mM, respectively. **(a,c)** Long-time-exposure images of cell trajectories, constructed from a mosaic of 7 (a) and 8 (c) images, each recorded over 6.7 s and acquired in rapid sequence. Accumulation of cells in the highest concentration region is evidenced by the high density of trajectories (white). **(b,d)** Normalized distribution of *E. coli* cells along the test channel, $B(s)$, from the experiments (bars) and the numerical model (solid line). The model results correspond to the solution of the bacterial transport equation (Eqs. 3.1 and 3.2) for the best-fit values of μ and χ_0. **(b)** $\mu = 7.0 \times 10^{-6}$ cm^2 s^{-1}, $\chi_0 = 4.5 \times 10^{-4}$ cm^2 s^{-1} **(d)** $\mu = 7.0 \times 10^{-6}$ cm^2 s^{-1}, $\chi_0 = 4.1 \times 10^{-4}$ cm^2 s^{-1}. $B(s)$ was normalized so as to have an area of 1.

In the exponential profile, bacteria migrated from the lower to the higher chemoattractant concentration, creating a peak in cell concentration followed by a depleted region [Fig. 3.6(a,b)]. The peak was positioned at the beginning of the constant, high-chemoattractant-concentration region. This distribution was compared with that predicted from the mathematical model (Eqs. 3.1 and 3.2), with good agreement in the location and magnitude of the peak and depleted regions [Fig. 3.6(b), solid line]. The best fit, computed by nonlinear chi-square fitting, was

obtained for $\mu = (7.0 \pm 0.5) \times 10^{-6}$ cm^2 s^{-1} and $\chi_0 = (4.5 \pm 0.2) \times 10^{-4}$ cm^2 s^{-1}, consistent with the values obtained for the linear concentration profile at the 95% confidence level and with the literature ranges cited above. Observations of bacterial chemotaxis in exponential gradients are not new and have been performed before using macroscopic devices [61, 102], where gradients were created by capillary assays [143], step addition [102] or stopped flow [61]. However, in those approaches gradients were unsteady and concentration fields difficult to control and quantify [61, 78]. Here it was possible to observe the response of bacteria to a steady exponential chemoattractant gradient and successful comparisons with theoretical predictions were made.

In the peaked profile, bacteria swam into the higher concentration region from both sides, resulting in strong accumulation [Fig. 3.6(c,d)]. The best fit was again obtained by nonlinear chi-square fitting, yielding $\mu = (7.0 \pm 0.4) \times 10^{-6}$ cm^2 s^{-1} and $\chi_0 = (4.1 \pm 0.2) \times 10^{-4}$ cm^2 s^{-1} [Fig. 3.6(d), solid line], consistent with results reported above. Chemotaxis in peaked concentration profiles applies for example to foraging of aquatic microbes, because nutrients in aquatic environments are often released from point sources[17] and result in Gaussian-type patches. Chemotaxis towards such patches has been studied with microdevices [14, 136, 137], limited to transient patches. In contrast, here the response of bacteria was observed to a steady patch, a useful model in the limit of slow patch diffusion (e.g. high molecular weight compounds) or fast motility.

3.4 Discussion

By creating steady concentration profiles, the chemotactic response dynamics without the chemoeffector gradient changing over time was studied. The decoupling of the temporal scales of the evolution of the chemical signal and the bacterial response is a highly desirable feature for chemotaxis studies, allowing for a simpler test of the gradient sensitivity and increased reliability in the quantification of random-motility and chemotaxis parameters. This decoupling enables one to extend the use of such devices to the study of the transient responses of a bacterial population to a steady chemoeffector gradient, thereby enabling the characterization of transient and steady-state responses within a single experiment. Moreover, these devices eliminate nearly all practical constraints on observation times characteristic of other diffusion-based gradient generators [73, 132], and thus can be applied to slow responses including sensory adaptation and population migrations over long length scales. Chemotactic response time can be species-specific and one would ideally be able to extend observations over large times otherwise experiments with slow-

swimming cells can become prohibitive. It is not surprising that these devices are nowadays being used to address a broader set of scientific questions. For example, one such application has been in identifying the logarithmic sensing mechanism of *E. coli* [67] while in another study, an alternate configuration of this device has been used to probe bacterial chemotaxis in stable competing gradients [68]. In this chapter, chemotaxis in arbitrarily shaped one-dimensional gradients was investigated, and the proposed microdevices can easily be modified to achieve alternate steady configurations, including but not limited to two-dimensional gradients. It can be expected that this class of microdevices will find a wide range of applications.

In addition to steadiness, an important feature of the proposed gradient generators is the rapid establishment of the gradient within the test channel once the gradient in the agarose layer is formed. In other diffusion-based designs [133, 144], cells experience an ever-changing concentration field while the gradient develops in the test channel. In this device and related designs [93, 135] there is a significant separation of time scales between gradient generation in the agarose layer ($\sim L^2/2D$) and in the test channel ($\sim H^2/2D$). Whereas the former must be established by horizontal diffusion across a few millimeters (L) over one to several hours, the latter only requires vertical diffusion over ~ 100 μm (H), and thus forms in a few seconds. On the other hand, the time required to generate the gradient in the agarose can be a drawback in some applications. Flow-based microdevices can generate gradients more rapidly [86, 88, 92], but they expose cells to shear stresses. A recent method succeeded in eliminating shear from a flow-based device [145] by translating the gradient to a static chamber through a porous layer and can possibly be adapted to create nonlinear gradients.

In summary, the observed distribution of *E. coli* was compared with model predictions for both linear and nonlinear gradients and very good agreement with published literature values was obtained. These results demonstrate the applicability of hydrogel-based microfluidic gradient generators to quantitative chemotaxis studies of free-swimming cells and their versatility in generating arbitrarily-shaped gradients. While the focus in this chapter was investigating bacterial chemotactic behavior, the applicability of these devices can be extended to a broad range of problems, whenever rapid establishment of stable gradients in the absence of flow is desired. Two such applications are presented in Chapters 4 and 5. The simplicity of fabrication

74

of the proposed design, along with its versatility to explore a wide range of chemical environments, will hopefully appeal to researchers in many fields and contribute to the improvement of understanding of microbial and cellular processes.

Chapter 4

Behavioral Consequences of Response Rescaling in Bacterial Chemotaxis[a]

4.1 Background

Sensory systems in organisms and cells allow them to sense and respond to physical and chemical cues in their environment. Some of the best characterized sensory systems include human senses, such as vision, touch and hearing, or unicellular sensing such as bacterial chemotaxis. A ubiquitous property of sensory systems at all scales is that of adaptation, in which a step increase in stimulus triggers an initial and often rapid change in a biochemical or physiological response, followed by a more gradual return toward a basal, pre-stimulus level. Graphically [Fig. 4.1(a)], consider a system with an input u (u_1 or u_2, representing two different level of inputs) and a response y, with y_0 being the initial, steady level of the response. A step change in input from u to pu (pu_1 or pu_2), where p is a scalar, will cause a change in the response, Δy. Adaptation then brings the response towards its pre-stimulus level, y_0. The term "exact" or "perfect" adaptation is used to refer to cases where the signal in question returns with very high precision to the pre-stimulus level.

Examples of adaptation in higher organisms include phenomena such as the control of the amount of light entering the eyes through the contraction and relaxation of the pupil by the nervous system, which brings intensities of illumination within the retinal working range. Adaptation helps increase sensitivity ranges, allowing sensory systems to detect changes in signals while ignoring background information.

Another property of an adaptive sensory system is its ability to rescale its response sensitivity to different ambient levels of input stimuli. In a wide variety of sensory processes (such as human vision and hearing), this rescaling is analogous to a quantitative relationship known as the Weber-Fechner law in psychophysics. This law states that the maximal response (Δy) to a change in stimulus is proportional to the change in stimulus scaled by the background ($\Delta u/u_1$ or $\Delta u/u_2$). In other words, two input signals with the same fold change (say, u_1 stepped to pu_1 or u_2 stepped to pu_2) yield the same maximum response, Δy.

The Weber-Fechner law by itself concerns only the maximal response and imposes no restriction on the transient response. On the other hand, exact adaptation concerns only the long-time return of the response to a steady state level, without regard to the maximal response [Fig. 4.1(c,d)]. If,

on the other hand, the entire shape of the response is identical under the same fold change in inputs (u_1 stepped to pu_1 or u_2 stepped to pu_2), a more general property is said to apply, namely Fold Change Detection (FCD) [Fig. 4.1(d)][72], which implies both Weber-Fechner's law and exact adaptation. Mathematically, if a system having internal variables x, input u and output y can be described by the set of ordinary differential equations $\dot{x} = f(x,y,u)$ and $\dot{y} = g(x,y,u)$, FCD holds if the system is stable, shows exact adaptation, and if g and f satisfy the following conditions for any $p>0$ [72]:

$$f(px, y, pu) = pf(x, y, u)$$
$$g(px, y, pu) = g(x, y, u)$$

(4.1)

FCD imposes strong limitations on potential mechanisms and it has been theoretically shown that many models for biological regulation do not exhibit FCD [146]. However, recent experimental studies showed that the transient response of certain biological systems (e.g. EGF induced ERK2 response dynamics, Wnt-induced β-catenin response dynamics in mammalian cells) [146, 147] exhibit FCD and it has been hypothesized that a wider class of mechanisms may exhibit this property as well [72].
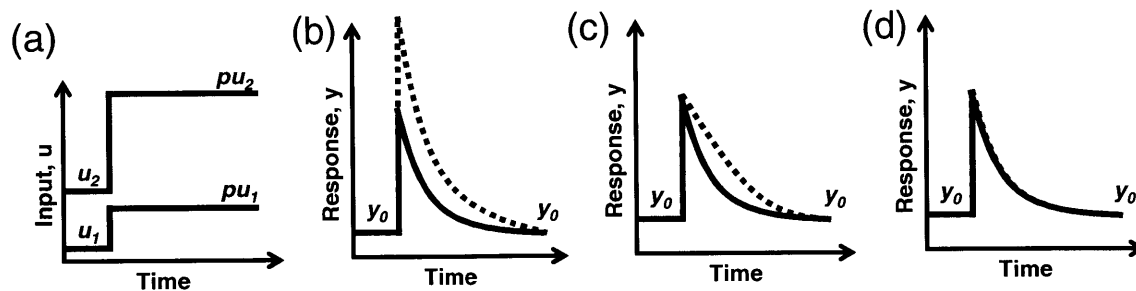
Figure 4.1 Possible dynamics of a sensory response to fold changes in input. (a) Input signal with two step changes having identical fold change (the same factor p), but different absolute changes. (b) Response of a sensory system to the two input signals with exact adaptation. The red line and the blue dashed line correspond to the responses to the step input changes from u_1 to pu_1(red) and u_2 to pu_2(blue), respectively. The two responses both adapt to the same pre-stimulus level. (c) Response of a sensory system that has exact adaptation and follows Weber-Fechner's law. The two responses have the same maximum amplitude. (d) Response of a sensory system that exhibits Fold-Change Detection: the two responses are entirely identical.

79

The chemotaxis system of the bacterium *Escherichia coli*, which senses temporal gradients of chemoeffectors as the cell samples its environment by swimming, has been known to possess the two complementary properties of exact adaptation and Weber-Fechner law. At the molecular level, the adaptive response, which follows a rapid excitatory response due to binding of chemoeffectors to the membrane-spanning receptors, is achieved by covalent modification of receptors by intra-cellular enzymes that restore pathway activity towards the pre-stimulus level, while also rescaling the sensitivity of receptors to ligand molecules (see section 1.2). Observations of exact adaptation of the chemotaxis signalling system can be found in studies with tethered cell assays, where the dynamic response of the cells to varied configurations of chemoeffector gradients are measured by either the bias in flagellar rotation [104] or *in vivo* kinase activity [25]. Evidence of response rescaling in bacterial chemotaxis can be traced back to the pioneering capillary assay experiments by Mesibov and Adler [98] in the 1970s, where a swimming population of bacteria was first allowed to adapt to a given concentration in a bath of chemoattractant and then to accumulate in a capillary containing a higher concentration of chemoattractant. By systematically varying the concentrations in the bath and capillary, while keeping the ratio of the two concentrations the same in each case, the authors found that the response (measured by the number of bacteria migrating into the capillary in a fixed amount of time) remained constant across several orders of magnitude of the ambient concentration, a property analogous to Weber-Fechner's law. Weber-Fechner's law for bacterial chemotaxis was also demonstrated in experiments using microfluidic devices, where a swimming population of bacteria was exposed to different scaled versions of a steady linear gradient and the response (measured by the strength of accumulation in a finite spatial domain) was found to scale with the ambient concentration in a similar way [67].

Recently, it has been predicted that bacterial chemotaxis in fact exhibits FCD, i.e. the response can be invariant not only in terms of the instantaneous response following a step change in stimuli (as in Weber-Fechner's law), but also in terms of the entire time series of the response, when the stimulus is rescaled with the background [72]. The stimuli-response relationship described in a recently developed bacterial chemotaxis model by Tu *et al.* [33] was found to satisfy the conditions for FCD (i.e. Eq. 4.1) [72]. The theoretical framework for the chemotaxis model by Tu *et al.* [33] is based on a Monod-Wyman-Changeux (MWC) description of the

receptor clusters that rapidly responds to stimuli and generates a response that affects the cell tumbling frequency (see Appendix B for details), matches very well experimentally measured responses to various monotonic, oscillatory, and impulsive stimuli of alpha-methyl-DL-aspartate (MeAsp), and can be used to predict responses to arbitrary temporal signals [32].

Previous experiments showed that the property of response rescaling holds in terms of the absolute magnitude of the response, when the measured quantities were number of bacteria in the capillary [98] or strength of accumulation in a spatial distribution [67] at a fixed point in time. However, the rescaling of the entire response time series as in FCD has remained unexplored. One could potentially perform experiments using different scaled step inputs of stimuli and compare the entire response time series to verify FCD. But typical signals encountered by cells in their natural environments are hardly constant or step-changing. Given the rapid diffusion of chemoeffector molecules over distances characteristic of bacterial motility [O (10-100 μm)], natural stimuli will mostly occur in the form of smooth gradients. When a swimming bacterium changes its position in a spatial gradient, steady or unsteady, its signaling system essentially senses fluctuating temporal patterns of input stimuli. Previous observations suggest that bacteria are able to rescale their responses in steady spatial gradients [67]. Also, in the famous capillary assay experiments by Mesibov $et\ al$ [98] the stimuli experienced by swimming cells were not steps, but rather time-varying spatial gradients. Therefore, characterizing the response to a continuously changing input signal, as experienced by the cells in steady or unsteady gradients, is crucial to understanding the cell's behavior and would provide a robust test of the FCD property.

In this chapter, the effects of FCD on the migratory behavior of swimming cell populations in controlled spatial gradients of chemoattractant was tested within a microfluidic device. Various scaled versions of steady and unsteady gradients of chemoattractants were generated using microfluidic devices, by systematically varying the ambient chemoattractant concentrations. The range of ambient chemoattractant concentrations was selected based on observed responses of recent tethered-cell assay experiments. A swimming population of $E.\ coli$ was exposed to these gradients and the quantitative response of the entire time series was recorded and compared. The prediction, based on the FCD property, is that the spatial distribution of a population will evolve

identically in different chemoeffector gradients, as long as the population is pre-adapted to concentrations scaled by the same factor as the fold-change in the magnitude of the gradients.

4.2 Experiments: from *in vivo* FRET to swimming populations

To test the theoretical predictions by Shoval *et al.* [72], Milena Lazova and Thomas S. Shimizu recently performed fluorescence resonance energy transfer (FRET) experiments on tethered cells [25]. FRET experiments yield real-time response feedback (in this case the activity of the kinase CheA) to arbitrary time-varying stimuli signals. In these experiments, bacteria were adapted to a given concentration of MeAsp and then exposed to a smoothly varying temporal waveform of stimulus. The response was observed for multiple MeAsp concentration waveforms, where the amplitude of the waveform in each case was scaled proportionately with the background concentration [Fig. 4.2(a)]. Within the ~10,000 fold range of background concentration tested, the response waveform (measured by the change in FRET signal, ΔFRET) showed distinct characteristics within three different concentration ranges. At low concentrations (< 0.018 mM), the response amplitude increased with the background concentration [Fig. 4.2(b)]. Within each of the next two regimes, at intermediate (0.018 mM - 0.23 mM) and high (0.82 mM - 10.3 mM) concentrations, it was found that the responses were invariant in both amplitude and waveform, although the response amplitude was ~40% greater in the intermediate regime compared to the high-concentration regime [Fig. 4.2(b)]. Therefore, although with a different amplitude, a response rescaling obeying the FCD property was observed in both of these concentration regimes, which therefore will be termed as regimes "FCD1" and "FCD2", respectively. Together, these two adjacent regimes span a ~500-fold range of background concentration. Since the low concentration regime does not obey FCD, it is referred to as the "no FCD" regime. The concentration range over which this invariance was observed in the FCD1 and FCD2 regimes altogether is consistent with expectations from the analysis by Shoval *et al.*[72] where they showed that FCD would be valid between the concentrations defined by the dissociation constants, K_I(~18µM) and K_A (~2.9mM), of the Tu-Shimizu-Berg model [33].

If the chemotaxis signaling pathway can produce invariant responses under rescaling of temporal gradients by the same factor as the ambient stimulus level, a swimming *E. coli* cell might, on average, do equally well at climbing chemoattractant gradients that are rescaled in a similar

manner. Trajectories of single bacteria are highly random and difficult to follow over extended times; however the spatial distribution of an ensemble of *E. coli* cells can be readily imaged over long periods. The spatial distribution of a population of bacteria exhibiting the FCD property is expected to evolve identically in a range of chemoattractant gradients where the magnitude of the gradients is scaled proportionately with the ambient chemoattractant concentration to which the bacteria is initially exposed.
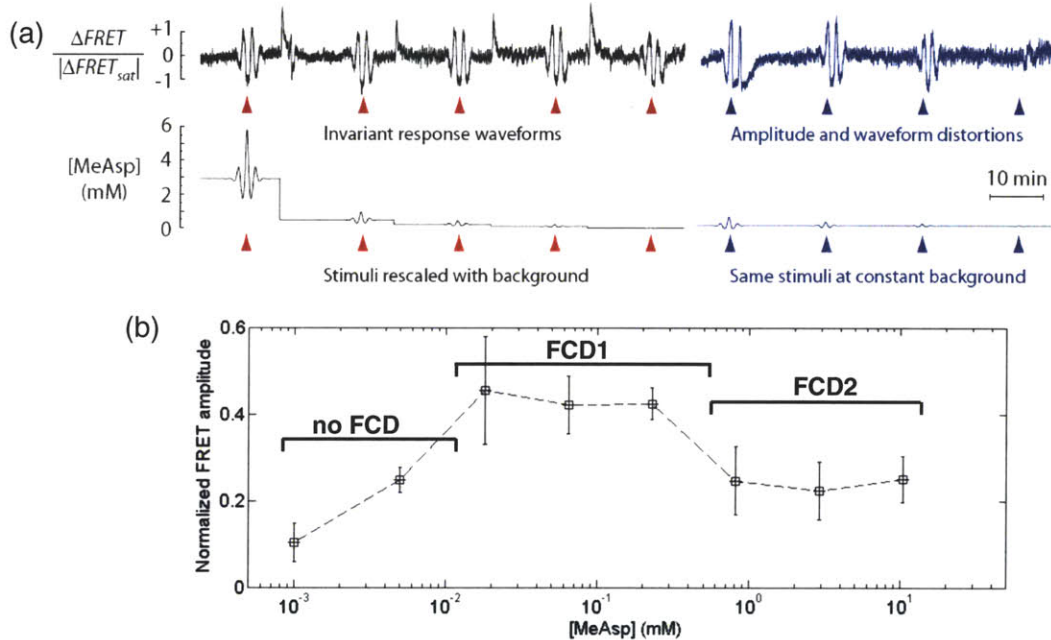
Figure 4.2 FRET experiments reveal response rescaling properties over a broad dynamic range (a) The stimulus and FRET response time series are shown for two different experiments in which *E. coli* cellswere exposed to time-varying concentrations of the attractant MeAsp. In the experiment shown on the left (black traces), five stimuli of identical waveforms, rescaled by the same factor as the background, were successively applied. Both the amplitude and waveform of responses were essentially invariant. In the experiment shown on the right (blue traces), the last four stimuli were repeated while the background concentration was kept constant at 0.23 mM. Both the amplitude and waveform of response varied significantly with the applied stimulus amplitude. [Figure reproduced with permission] **(b)** Normalized FRET response amplitudes of the waveforms within the linear regime of the response as a function of background MeAsp concentrations show three distinct concentration regimes. At the lowest concentrations (below 0.018 mM), the amplitude of response increases with background concentration ("no FCD" regime); between 0.018mM and 0.23 mM, the response amplitudes and waveforms are essentially invariant, demonstrating FCD with a large response amplitude ("FCD1" regime); between 0.82 and 10.3 mM, response amplitudes and waveforms are again invariant, but with a smaller amplitude ("FCD2" regime). [Figure reproduced with permission]

In order to test this prediction, it is necessary to expose bacteria to carefully controlled and manipulatable chemoattractant gradients: this can be done using microfluidic devices. In this study, the FCD property was tested in two different microfluidic devices, which generated (1)

steady, linear gradients and (2) unsteady, nonlinear gradients, representing two opposite ends of the spectrum of gradient complexities prevailing in natural environments. The steady, linear gradient represents a simplified version of many natural gradients in the limit of slow diffusion of chemicals (i.e. high molecular weight compounds) or for the case of constant flux from a source (e.g. from nutrients leaking from sediments, or dissolved organics exuded by a phytoplankton cell). The unsteady gradient, in contrast, mimics the case of a changing nutrient environment (e.g. an ephemeral nutrient pulse). The spatial distribution of bacteria in the microchannels was monitored over time and compared, in order to test the prediction – born out of the FRET experiments – that *E. coli* chemotaxis exhibits the FCD property.

4.3 Materials and methods

4.3.1 Bacterial strains and chemoattractant

Both *Escherichia coli* RP437 and AW405 cultures were used in this study. The cultures were grown in Tryptone Broth (1% tryptone, 0.5% sodium chloride) at 34°C on an orbital shaker (220 rpm) to mid-exponential phase ($OD_{600} = 0.45$) and then washed twice by centrifugation at 2000g for 5 min and resuspension of the pellet in motility buffer (10 mM potassium phosphate buffer, 0.1 mM EDTA, 10 mM NaCl; pH = 7). Cells were kept at 4°C for 1 to 3 h prior to the start of the microfluidic experiments. Cells were further diluted 1:2 to 1:3 in motility buffer to obtain optimal condition for tracking (cell concentration = $(2.5-4.0)\times10^8$ cells/ml). α-methylaspartate (Sigma-Aldrich, USA), a non-metabolizable analog of aspartate[53], having a diffusivity of 5.5×10^{-10} m^2s^{-1}, was used as a chemoattractant. α-methylaspartate was diluted in motility buffer to obtain final concentrations ranging from 0.75 μM to 13.79 mM [see Tables 4.1 and 4.2].

4.3.2 Experimental setup for steady linear gradients and data acquisition

Microfluidic chemotaxis experiments were performed in a hydrogel-based linear gradient generator, using agarose as the hydrogel (see Chapter 3). Briefly, a 1 mm thick agarose layer was sandwiched between a glass slide and a PDMS (Polydimethylsiloxane; Sylgard 184; Dow Corning, MI, USA) layer. The microdevice consisted of three parallel channels, each 600 μm wide [Fig. 4.3(a)]. Two 100 μm deep feeder channels (source and sink channels) were patterned
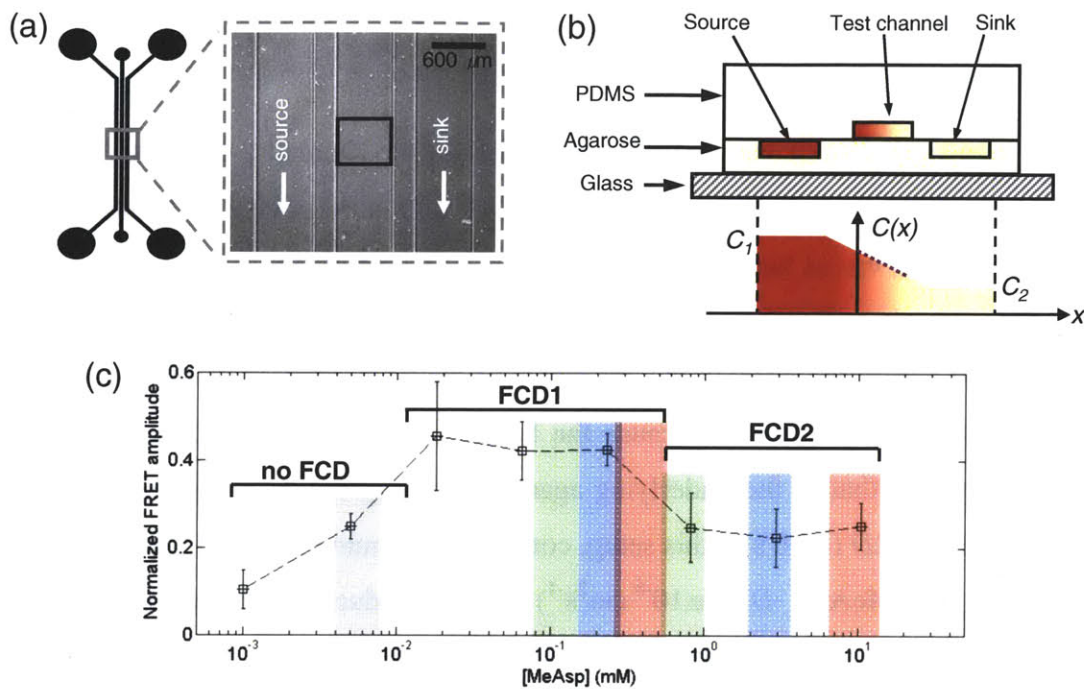
Figure 4.3 Experimental setup to test FCD property in steady linear gradients. (a) The three-channel microfluidic device used to generate a steady linear gradient to test the chemotactic performance at the level of cell behavior. The configuration of this channel corresponds to the 'design 3'channel described in Chapter 3. (b) A schematic illustration of the cross-section of this channel and gradient generation. A stable linear gradient is generated in a layer of agarose hydrogel, between the source channel and the sink channel, through which constant concentrations of MeAsp, C_1 and C_2 respectively ($C_1=2C_2$), are flowed. At the start of each experiment, the bacteria are injected into the "test channel", engraved within a slab of PDMS, which rests above the hydrogel, and the MeAsp profile within the test channel rapidly equilibrates with that in the hydrogel gradient below. Bacterial distributions were obtained in a 600μm × 450μm field of view inside the test channel as shown in (a). (c) The color-shaded bars (see also Figure 4.2(b))highlight theconcentrations spanned by each of the seven spatial gradients in which the population migration experiments were conducted for the steady linear gradient. The bars from left to right correspond to the ranges of concentrations for each case described in Table 4.1.

in agarose and one 50 μm deep test channel in PDMS corresponding to the configuration of 'Design 3' in Chapter 3. The test channel was fabricated using standard soft lithography techniques [64, 71]. The agarose layer was made from a 3% (w/v) solution of Ultra Pure Agarose (Invitrogen, CA, USA) in motility buffer, heated for 30 s in a 1250 W microwave oven, and poured over a silicon wafer with positive reliefs of the feeder channels. After being allowed to gel at room temperature, the agarose layer was cut to size and used immediately or stored in motility buffer. Flexible polyethylene tubing (Cole-Parmer, USA) and metal connectors (New England Small Tube Corp, NH, USA) were used to connect the inlets of the source and sink channels with two 0.5 ml glass syringes (Hamilton Company, NV, USA), driven by a syringe

pump (PHD 2000, Harvard Apparatus, MA, USA), and the inlet of the test channel with a 1 ml plastic syringe (BD, NJ, USA), operated manually.

A constant flow rate of 1 μl/min was maintained in the feeder channels, with two different concentrations of α-methylaspartate (Sigma Aldrich, MO, USA) in the source and sink channel. These concentrations were varied between 0.004 mM and 13.8 mM (Table 4.1). Diffusion from the source to the sink channels, which are $L = 1$ mm apart (edge-to-edge), establishes a concentration gradient across the agarose in ~20 min, and the concentration in the test channel reflects that in the underlying agarose. Because the height of the test channel, $H = 50$ μm, is small, a gradient mirroring that of the underlying agarose layer rapidly develops within the test channel within a time $\sim H^2/2D$ (< 10 s in this setup, computed assuming a typical small-molecule diffusion coefficient for MeAsp, $D = 5 \times 10^{-6}$ cm^{2}s^{-1}) after introduction of the bacteria. The gradient within the test channel was previously verified to be linear, with a magnitude equal to 69% of the gradient predicted assuming a completely linear decay between source and sink channels. After the gradient had formed, a suspension of *E. coli* RP437 was manually injected in the test channel by suction and the inlet and outlet of the test channel were sealed with coverslips to prevent residual flow and evaporation. Before injection, the cells were pre-adapted for at least 20 minutes to the mean of the source and sink channel MeAsp concentration (i.e. the mean concentration of the test channel, C_0; Table 4.1).

Experiments were conducted for seven different steady linear gradients ranging from 0.004 mM/mm to 6.9 mM/mm. These gradients were set up by flowing seven different pairs of MeAsp concentrations in the source and sink channels. In each case, the concentration of MeAsp in the source channel was maintained at twice the concentration of the sink channel (i.e. $C_1 = 2C_2$). This ensured that the steepness of the expected gradient rescaled by the mean concentration in the test channel was the same in each case (Table 4.1).This is a necessary condition for the input stimuli for FCD. The mean MeAsp concentrations in the test channel, C_0, were selected based on the FRET amplitude responses [Fig. 4.2(c)] in the following way: one of them corresponds to a concentration in the "no FCD" regime, while three others correspond to each of the "FCD1" and "FCD2" regimes [see Table 4.1 and Fig. 4.3(c)]. It is important to note that in this microfluidic setup, the magnitude of the actual gradient would differ from that of the expected gradient by a

factor of 0.69, because of the 2-D nature of solute diffusion through the agarose (see Chapter 3). Therefore, the logarithm of the actual gradient would be decreased by 0.37. Yet, this decrease is identical in all cases and the condition for input stimuli for FCD are still not been violated.

Table 4.1 Range of MeAsp concentrations and gradients in the microfluidic linear gradient generator.

Regime	Concentration of MeAsp (μM)			Gradient (μMmm^{-1}) dC/dx	Relative gradient(mm^{-1}) $(1/C_0)dC/dx$
	Source channel, C_1	Sink channel, C_2	Mean (pre-adaptation), C_0		
No FCD	8	4	6	4	0.67
FCD1	160	80	120	80	0.67
	304	152	228	152	0.67
	574	287	430	287	0.67
FCD2	1086	543	814	543	0.67
	3870	1935	2903	1935	0.67
	13794	6897	10346	6897	0.67

4.3.3 Experimental setup for unsteady nonlinear gradients

To test the FCD property in unsteady nonlinear gradients, the microfluidic device described in section 2.4.5 was used with a minor modification (the channel was fabricated with a width of 2.4 mm instead of 3 mm) [Fig. 4.4(a)]. This device was primarily designed with the objective of creating a diffusing band of chemoattractant, to simulate an ephemeral, microscale 1-D nutrient patch in the ocean [13, 14, 73, 136, 137, 148]. Using two inline inlet ports, which were used to introduce bacteria and chemoattractant into the channel separately, initially a coherent band of chemoattractant in the center of the channel was produced by a constant flow rate driven by a syringe pump (PHD 2000, Harvard Apparatus). PEEK tubing (0.762 mm ID, 1.59 mm OD; Upchurch Scientific) was used to connect inlets to 5 mL and 500 μL glass syringes (Hamilton Gastight) containing chemoattractant and bacterial suspension, respectively. When the flow was stopped by turning off the syringe pump, the chemoattractant band began to diffuse laterally and the bacterial suspension on either side of the band experienced time-varying nonlinear spatial gradients. However, the observation time frame for response that this device provides is limited

by the time scale of diffusion of chemoattractants over the half-width of the channel, after which the gradients inexorably reduce to homogeneity. In this case, the diffusion time-scale can be
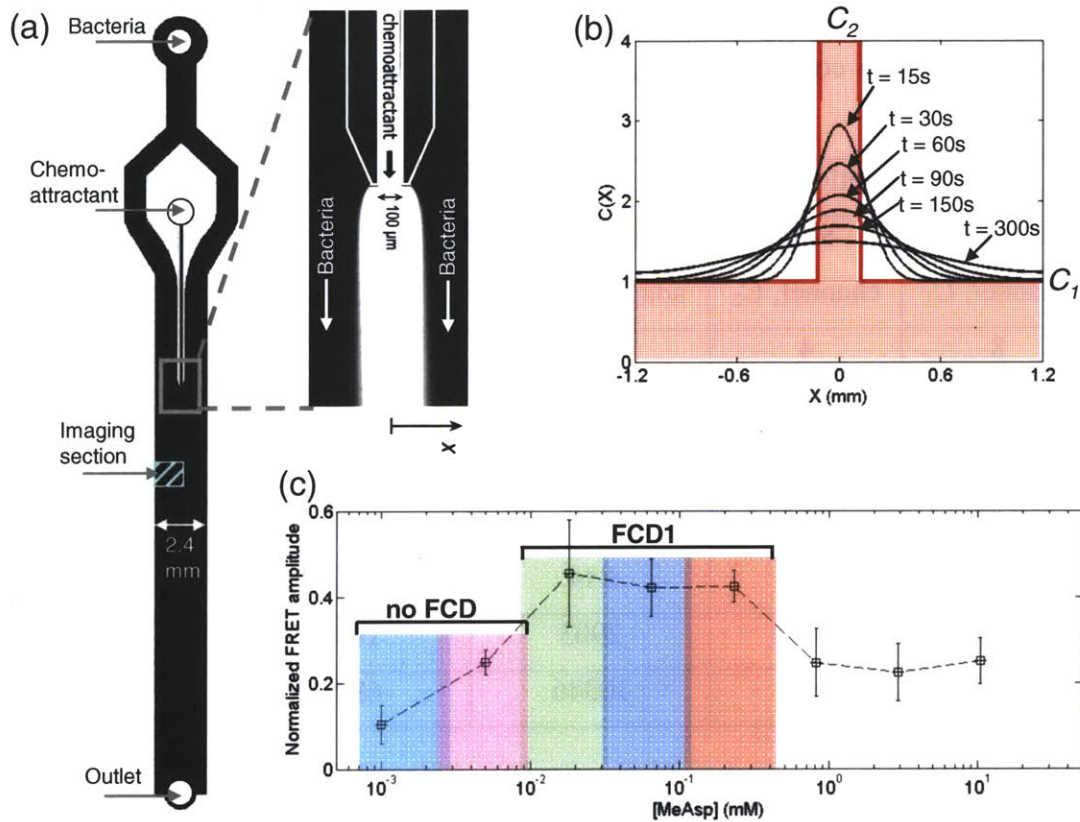
Figure 4.4 Experimental setup to test FCD property in unsteady nonlinear gradients. (a) The microinjector device used to generate unsteady nonlinear MeAsp gradients. MeAsp having a concentration C_2 was injected at the centre of a 2.4mm wide channel while bacteria preadapted to a concentration of C_1 were flown in parallel on both sides. Since $C_2>C_1$, this generates a coherent band of chemoattractant of higher concentration in the middle at time $t = 0$ (shown with fluorescein). The imaging section for obtaining bacterial distributions was a 900µm × 1200µm rectangular region and spanned the width of the left half of the channel. **(b)** Numerical simulation of the evolution of the concentration profile, $C(x)$, after the flow is stopped assuming a step concentration profile at time $t = 0$. $C(x)$ is normalized by the initial ambient (preadaptation) concentration, C_1. **(c)** The color-shaded bars (see also Fig. 4.2(b)) highlight the concentrations spanned by each of the five spatial gradients in which the population migration experiments were conducted for the unsteady nonlinear gradient. The bars from left to right correspond to the range of concentrations for each case described in Table 4.2. Two of the bars span a range within the "no FCD" regime while three of the bars span a range within the "FCD1" regime.

estimated as $W^2/2D$ (~21 min, computed assuming a typical small-molecule diffusion coefficient, $D = 5.5 \times 10^{-6}$ cm^{2}s^{-1} and using the half-width of the channel, $W = 1.2$ mm).

Experiments with nonlinear gradients were performed for five different injection concentrations (C_1) of MeAsp, ranging from 0.003 mM to 0.456 mM. To satisfy the input stimuli condition for FCD, in each case the *E. coli* suspension was pre-adapted to MeAsp concentrations 1/4th of the initial concentration of the pulse, thereby ensuring that the initial step change in concentration rescaled by the ambient concentration C_1 remained the same. As time progresses, MeAsp diffuses on both sides of the injection space and the spatial gradient will evolve from a step-like profile to smoother Gaussian-type profiles with a gradually decreasing peak [Fig. 4.4(b)]. Therefore the ratio between the maximum (at the peak) and minimum (near the walls) concentration will also decrease. However, this ratio remains identical at each time for each of the five cases, implying that the input conditions for FCD remain valid for all subsequent time steps after initial injection. The five injection and ambient concentration pairs were selected within the concentration domain of the FRET response-concentration relationship [Fig. 4.2(c)] so that the average of the respective injection and ambient concentrations correspond to the "no FCD" regime for the first two cases, while the remaining three belonged to the "FCD1" regime. The details of the initial input stimuli conditions are summarized in Table 4.2 and the ranges of concentrations are shown in Fig. 4.4(c).

Table 4.2 Range of MeAsp concentrations in the microfluidic injector channel used to generate nonlinear gradients.

Regime	Concentration of MeAsp (µM)		Fold change in concentration, C_2/C_1	Relative step in concentration $(C_2-C_1)/C_1$
	Preadaptation, C_1	Injection, C_2		
No FCD	0.75	3	4	3
	2.5	10	4	3
FCD1	9	36	4	3
	32	128	4	3
	114	456	4	3

4.3.4 Data acquisition and analysis

Chemotaxis experiments were conducted using a computer-controlled inverted microscope (TE2000-E, Nikon, Japan), equipped with a CCD camera (PCO 1600, Cooke, MI, USA).

Bacteria were observed at channel mid-depth, using phase contrast microscopy. To obtain spatial distribution of bacteria a sequence of multiple frames ('movie') was captured. Image analysis was performed by subtracting each frame from the following one, to focus only on motile cells, and by subsequently locating bacteria in each frame as peaks in a monochrome intensity field, using IPlab (BD, MD, USA). Finally bacterial positions were determined over all frames in a movie and binned to yield the cell concentration profile, $B(x)$, along the direction of the gradient, using MATLAB (The Mathworks, MA, USA).

For experiments in steady linear gradients, movies were captured every 2 minutes, from 1 min to 39 min after the injection of bacteria in the test channel, using a 20× objective, where each of the movies consisted of 200 frames recorded at 10 frames/s. The longer side of the field of view under a 20× objective coincided with the width of the test channel [Fig. 4.3(a)]. For the experiments in unsteady nonlinear gradients, movies consisting of 200 frames were captured at 32 frames/s every 30 seconds, from 15 seconds to 12.25 min, after stopping the flow in the main channel. In this case, the movies were taken using a 10× objective at a location 4 mm downstream from the tip of the injector. The field of view under the 10× objective (900μm × 1200μm) was positioned in such a way that the longer side spanned the width of the left half of the channel [Fig. 4.4(a)]. Since the profiles of the spatial gradients are symmetrical along the longitudinal axis of this channel, the response is symmetric as well. A data acquisition scheme incorporating the bacterial response in only one half of the total width of the channel was adopted for achieving a finer temporal resolution of data within a limited available observation time, due to the diffusion of the chemicals in a finite spatial domain. Three replicates were run for each of the unsteady nonlinear gradient scenario.

4.4 Results

4.4.1 FCD in steady linear gradients

To test the FCD property for chemotaxis, the migration behavior of swimming *E. coli* RP437 cells was studied in steady linear spatial gradients of MeAsp established in a microfluidic device. Steady gradients of seven different magnitudes were generated by systematically varying MeAsp concentrations in the source-sink channels. For each case, bacteria, pre-adapted to the mean

concentration of MeAsp were introduced into the test channel, which had one face open to the underlying agarose layer where the steady linear gradient had been pre-established. Preadaptation to the mean MeAsp concentration ensured that the bacteria were exposed to the same rescaled gradient magnitude.

In the beginning of the experiment, immediately after the injection of bacteria, the cells are distributed nearly uniformly across the width of the channel. However, as the cells begin to respond to the steady gradient, the distribution of cells gradually becomes non-uniform, as they move towards the gradient. Fig. 4.5 shows typical cell-trajectory images acquired during such an experiment. The left panel shows the nearly uniform distribution in the beginning of the experiment, while the right panel is from a time close to the end of the experiment, and demonstrates strong accumulation of cells near the source channel. By computer analysis of the sequence of images the bacterial distribution along the gradient, $B(x)$, was obtained at two-minute intervals.
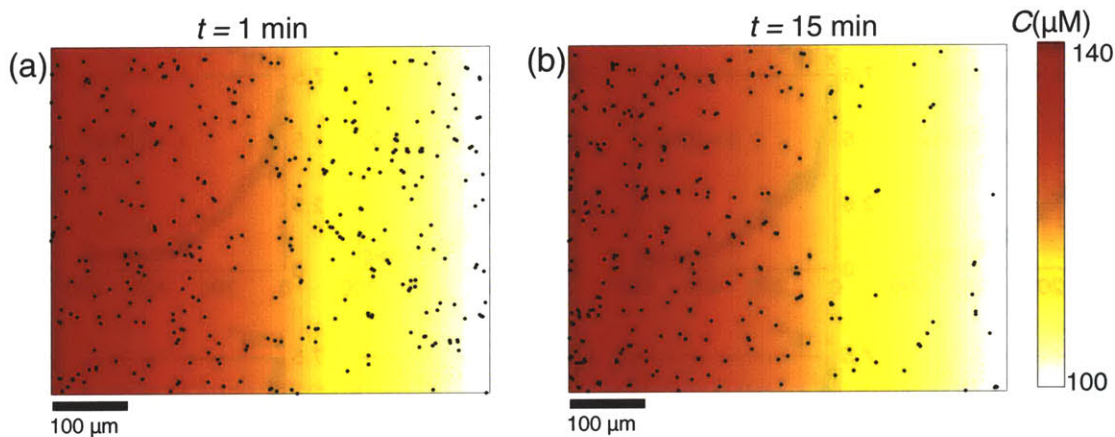
Figure 4.5 An example of the evolution spatial distribution of cells in the presence of a linear chemoeffector gradient. The spatial coordinates of cells identified by image analysis are indicated as black points within a 600μm × 450μm field of view over the linearly varying concentration background having a gradient of 80 μM/mm. Panel (a) shows the positions of cells 1 min after injection, which is nearly uniform along the x direction. Panel (b) shows the positions of cells 15 min after injection. In this case, a clear accumulation of cells can be observed towards the direction of the gradient (increasing from right to left).

Figures 4.6 and 4.7 show the time evolution of the distributions, $B(x)$, in response to the gradients in the FCD1 and FCD2 regimes, respectively, the three profiles in each subplot corresponding to the response to the three gradients chosen under each of the FCD regimes (see
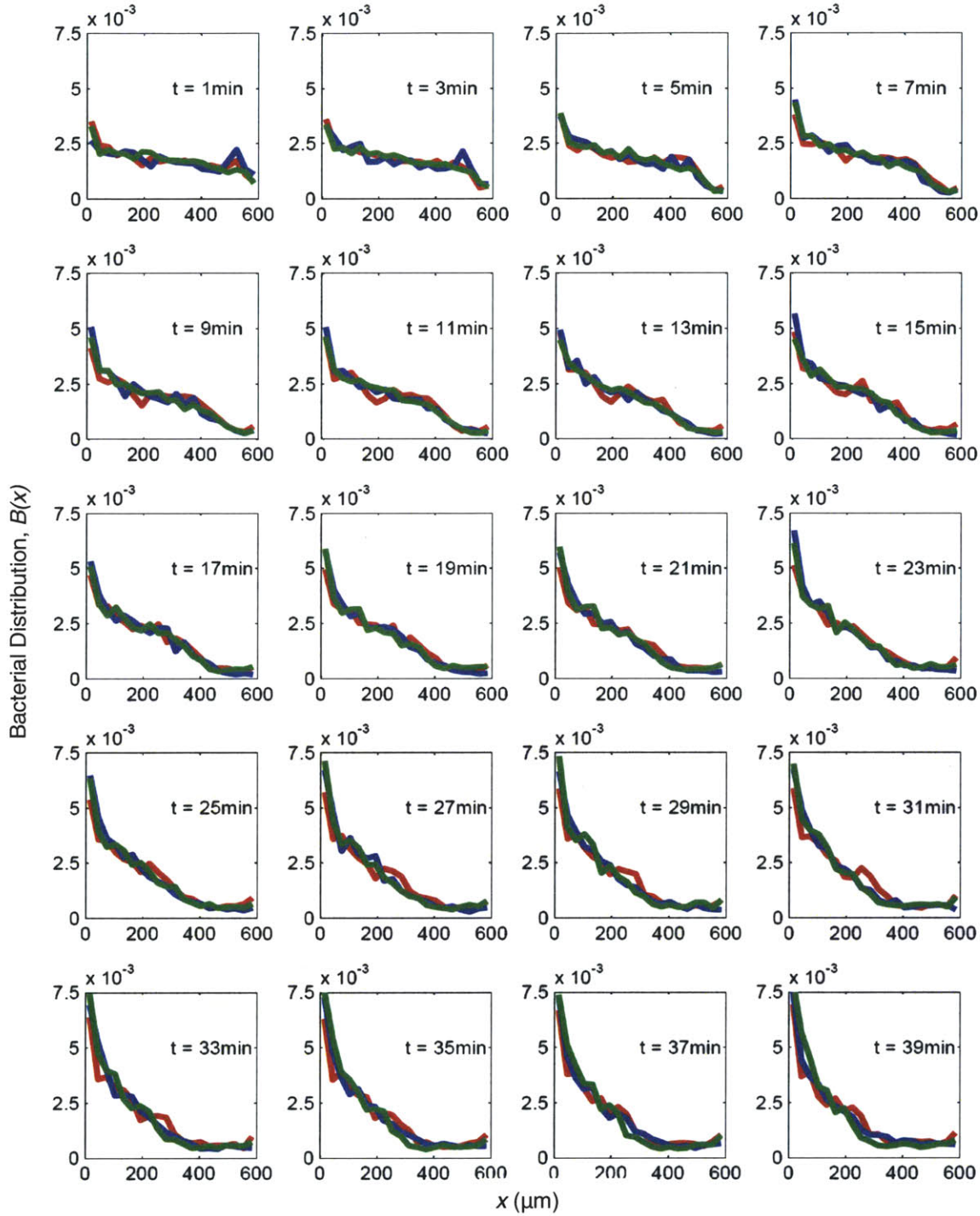
Figure 4.6 Time evolution of the bacterial density profile, $B(x)$ in steady linear gradients in the FCD1 regime. The direction of the MeAsp gradient is towards the left. The red, blue and green curves correspond to the bacterial response for the gradients 80, 152 and 287 μM/mm, respectively. In each experiment, bacteria were pre-adapted to a mean concentration, C_o, prior to injection, so that the ratio $(1/C_0)dC/dx$ was always kept at a fixed value ($2/3$ mm^{-1}), in order to maintain a fixed fold-change in the stimulus experienced by bacterial populations during each experiment. The time evolution of bacterial responses were indistinguishable within this regime for the three gradients, indicating that *E. coli* chemotaxis exhibits fold-change detection property
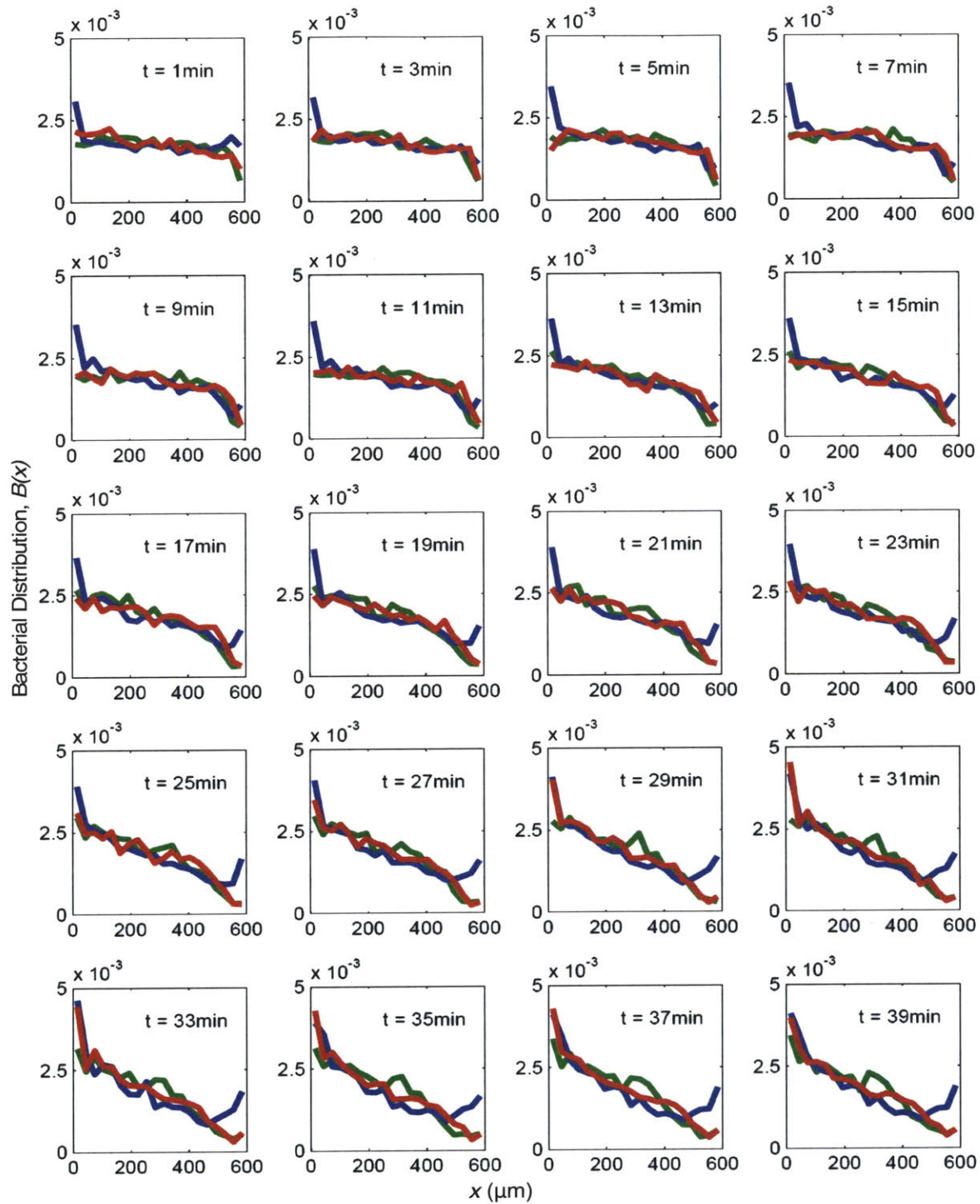
Figure 4.7 Time evolution of the bacterial density profile, $B(x)$, in steady linear gradients in the FCD2 regime. The direction of the gradient is towards the left. The red, blue and green curves correspond to the bacterial response for the gradients 543, 1935 and 6897 μM/mm, respectively. In each experiment, bacteria were pre-adapted to a mean concentration, C_o, such that the ratio $(1/C_0)dC/dx$ was always kept at a fixed value (2/3 mm^{-1}) in order to maintain a fixed fold-change in the stimulus experienced by bacterial populations during each experiment. The time evolution of bacterial responses were indistinguishable within this regime for the three gradients.

Table 4.1). In Fig. 4.6, the red, blue and green profiles correspond to the results for mean concentrations of 0.12, 0.228 and 0.43 mM, respectively, all of these taken within the FCD1 regime. In each instance, as mentioned above, the bacterial distribution is uniform at the start of the experiments (t = 1 min), but becomes progressively more skewed towards the direction of the gradient (to the left) as time progresses. Eventually, a steady state distribution is obtained, around $t = 25$ minutes, after which there is no appreciable difference in the profiles. It can be readily seen from these profiles that the entire time-evolution of $B(x)$ is essentially invariant within the FCD1 regime, even though the difference in the absolute mean concentration is ~4-fold. Similar time-evolution plots for the three mean concentrations in the FCD2 regime show similar characteristics, as depicted in Fig. 4.7, where the red, blue and green profiles correspond to mean concentrations of 0.81, 2.9 and 10.3 mM. In this case, a ~12 fold change in the mean concentration again yielded an invariant response in bacterial distribution. There is, as expected, a clear difference in the response among the two FCD regimes, with the lower-concentration FCD regime ("FCD1") demonstrating considerably stronger accumulation near the source than the higher-concentration FCD regime ("FCD2"). This confirms the observation of the lower amplitude FRET response in the FCD2 regime compared to the FCD1 regime, observed by Lazova and Shimizu [Fig. 4.2(b)].

To better demonstrate the time-evolution of the bacterial profiles, a Chemotactic Migration Coefficient (CMC) was computed for each time, from 1 to 39 minutes. The CMC is shown in Fig. 4.8. The CMC is a dimensionless metric of the strength of chemotaxis, measured as the degree of non-uniformity in the cell distribution along a spatial gradient, and is defined as [94]:

$$CMC = \frac{1}{L/2} \frac{\int_{-L/2}^{L/2} x'B(x')dx'}{\int_{-L/2}^{L/2} B(x')dx'} \tag{4.2}$$

Here, x' is the direction across the channel (i.e. along the gradient), with $x' = 0$ at mid-width, and the integral extends over the entire width of the channel, L. No chemotaxis (uniform distribution) corresponds to CMC = 0, while accumulation towards $x' > 0$ corresponds to CMC > 0.

The chemotactic migration pattern of bacteria in a steady linear gradient determines the shape of the CMC time series. Initially, bacteria are nearly uniformly distributed over the channel and the

CMC values are close to zero. As the bacterial distribution becomes gradually skewed in the direction of the gradient, CMC values increase, until a steady-state is achieved. Fig. 4.8 demonstrates the time evolution of CMC within the two FCD regimes, as well as for the "no FCD" regime (mean concentration of 5 µM MeAsp). As expected from the low amplitude of the FRET response in the "no FCD" regime, the accumulation in the direction of the source channel is weak, even at the final time (CMC = 0.12 at t = 39 min). Higher CMC values were found for
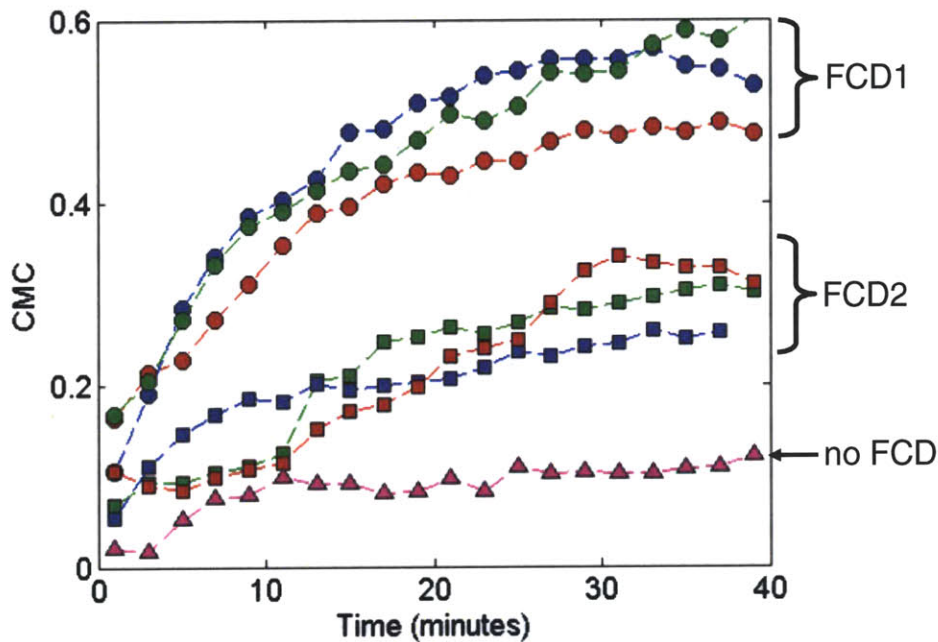
Figure 4.8 The Chemotactic Migration Coefficient (CMC) as a function of time, computed from the chemotactic response of swimming cell populations within and outside the two FCD regimes. The red, blue and green filled circles correspond to the CMC values for 80, 152 and 287 µM/mm, respectively, the three MeAsp gradients within the FCD1 regime. The red, blue and green filled squares correspond to the CMC values for543, 1935 and 6897 µM/mm, respectively, the three MeAsp gradients within the FCD2 regime. The magenta triangles correspond to the "no FCD" regime. The CMC is a measured by the degree of accumulation of bacteria near the side facing the source channel. Chemotaxis was stronger in the FCD1 regime, resulting in higher CMC values, while the response for the FCD2 regime was somewhat weaker, resulting in lower CMC values. However, within each of the two FCD regimes the temporal CMC profiles were found to be essentially invariant. The weakest chemotactic response was observed for the "no FCD" regime, for which the temporal CMC profile was distinct from either of the two FCD regimes.

the two FCD regimes, with the low concentration regime showing the highest chemotactic performance (average CMC for the three FCD1 cases = 0.53 at t= 39 min) than the higher concentration regime (average CMC for the three FCD2 cases = 0.27 at t= 39 min). Most importantly, for the three cases tested within each FCD regime the temporal CMC profiles remain essentially invariant. These results with swimming populations demonstrate that within the concentration regime in which both response waveform and amplitude are invariant in the

95

FRET experiments, i.e. where FCD holds, the chemotactic performance in spatial gradients is also invariant.

4.4.2 FCD in unsteady nonlinear gradients

To test the effect of FCD in unsteady gradients, *E. coli* AW405 were pre-adapted to a concentration varying between 0.75 and 114 μM MeAsp and exposed to a pulse of MeAsp in the microinjector channel. The concentration in the pulse was 4-fold larger than the pre-adaptation concentration. The region of the pulse was initially devoid of bacteria. Swimming cells rapidly fill this gap by random motility and chemotaxis, as evidenced by the nearly uniform bacterial distribution at $t = 15$ s [Fig. 4.9(a)]. The diffusion of MeAsp in the transverse direction causes chemotactic bacteria to swim up the gradient, which results in the accumulation of cells within the central region of the microchannel [Fig. 4.9(b)]. However, as the gradient becomes milder, the intensity of the aggregation also decreases, although a clear accumulation of cells can persist for several minutes, before returning to a uniform distribution as the chemoattractant profile becomes nearly uniform across the channel. Fig. 4.9 shows typical snapshots of bacterial positions over time along the left half of a transverse section of the microchannel for a pulse concentration of 456 μM MeAsp.
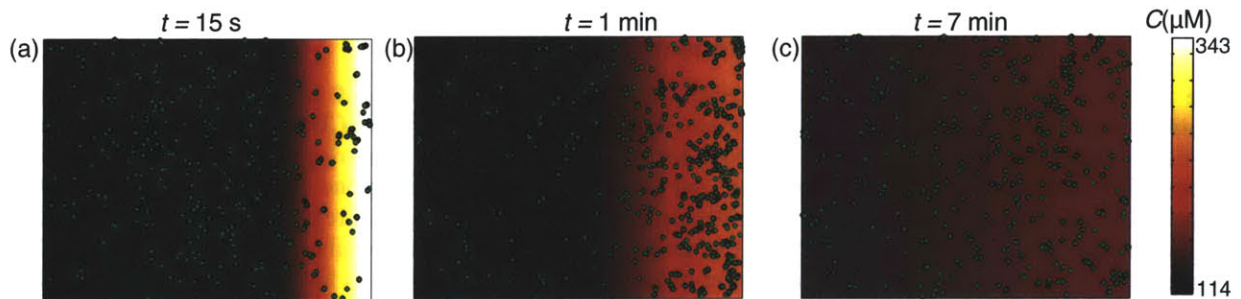
Figure 4.9 An instance of the time-evolution of the spatial distribution of cells in the presence of an unsteady MeAsp gradient. The spatial coordinates of cells identified by image analysis are indicated as green points within a 1200μm × 900μm field of view (left half of a transverse section of the microfluidic device) over a nonlinearly varying concentration background generated by a 456 μM MeAsp pulse. The colorbar indicates the concentration, C, of MeAsp. Panel (a) shows the positions of cells 15 s after injection of the pulse, at which time the bacterial distribution is nearly uniform along the x-direction (i.e. horizontal direction). Though the gradient is steep, the majority of the cells have not yet been exposed to the gradient. Diffusion of MeAsp makes the gradient milder but allows more cells to be exposed to the gradient, as evidenced by their chemotactic response shown in panel (b), which shows the position of cells 1 min after injection of the pulse. Further diffusion of chemoattractant makes the gradient even milder and reduces the intensity of chemotactic response, eventually resulting in a near-uniform bacterial distribution, as shown in panel (c) for t = 7 min.
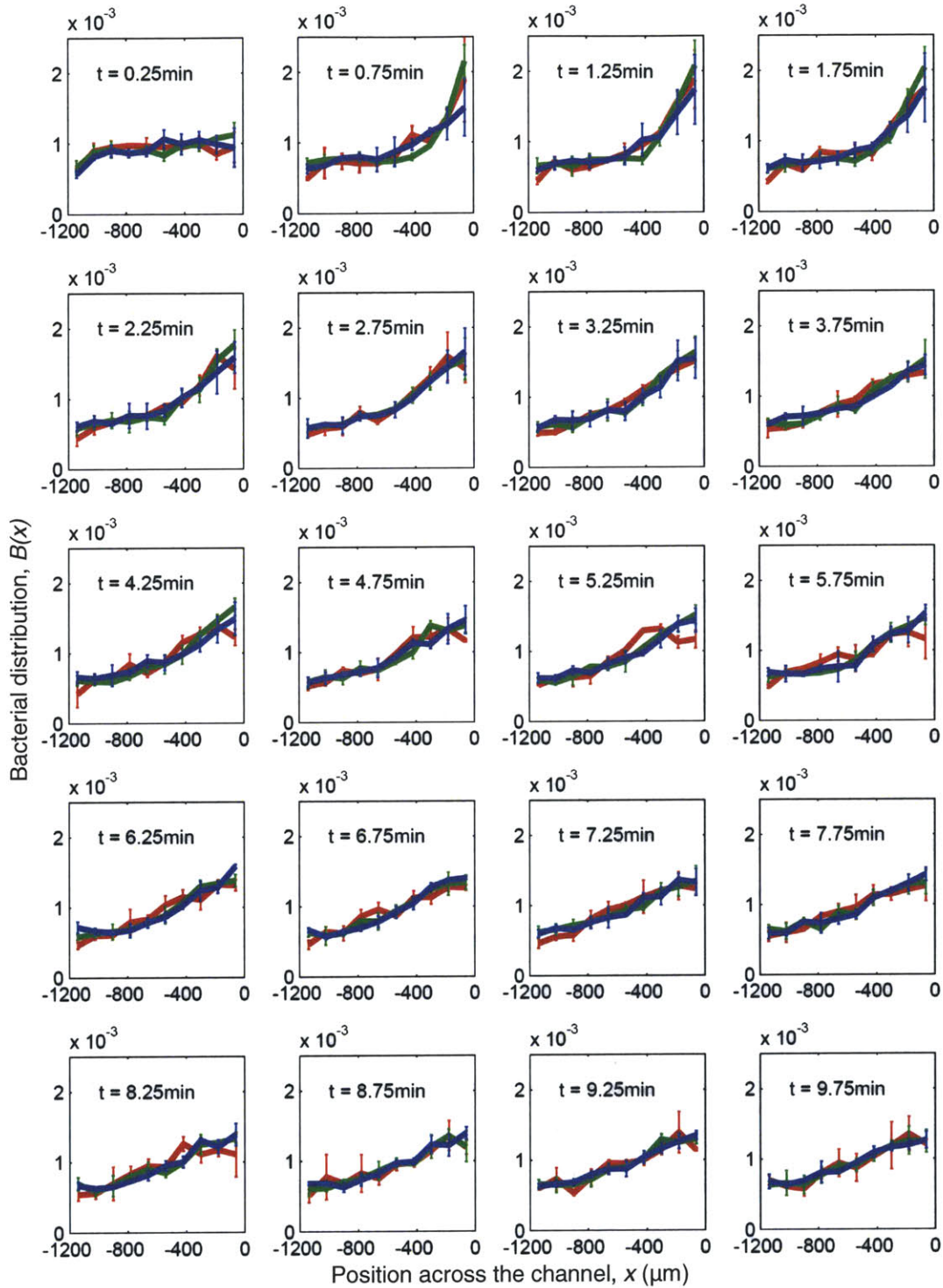
Figure 4.10 Time evolution of the bacterial distribution, $B(x)$, in unsteady nonlinear gradients in the FCD1 regime. The red, blue and green profiles correspond to unsteady gradients generated by initial injection of MeAsp concentrations of 36, 128 and 456 µM, respectively. In order to maintain a fixed fold-change in the stimulus experienced by bacterial populations, the bacteria were pre-adapted to 0.25 times the injection concentration before initiating the experiments. The time evolution of the bacterial responses were indistinguishable from each other for the three cases, indicating that *E. coli* chemotaxis exhibits FCD within this concentration regime.

Fig. 4.10 shows the time-evolution of the bacterial distribution, $B(x)$, in response to the unsteady MeAsp gradients within the FCD1 regime (Table 4.2). The three profiles in each panel correspond to the bacterial distribution along the left half of the microfluidic channel, for the three injection concentrations (the red, blue and green profiles indicate the response for pulse concentrations of 0.036 mM, 0.128 mM and 0.456mM, respectively). In all cases, as mentioned above, the bacterial distribution is nearly uniform at the start of the experiments (i.e. $t = 15$ s), but quickly becomes skewed in the direction of the gradient (i.e. to the right), showing the maximum response around $t = 1.15$ min. When the gradient becomes milder, the response gradually becomes weaker, although some degree of accumulation persists even at the endpoint of the experiments ($t = 14$ min). These profiles show that the entire time-evolution of $B(x)$ is essentially invariant over a 13-fold change in pulse concentrations within the FCD1 regime.

The degree of similarity among the three profiles is better demonstrated by the temporal CMC profiles [Fig. 4.11]. The CMC was computed using Eq. 4.2 from the time series of the bacterial distributions for the FCD1 regime [Fig.4.10], as well as the "no FCD" regime, where each point in time refers to the mean CMC for three replicates. The bacterial response in the FCD1 regime shows markedly higher CMC values (maximum CMC= 0.31) compared to the "no FCD" regime (maximum CMC = 0.06), for which the chemotactic response was weak throughout the entire experiment. These observations are in agreement with the higher amplitude response in the FCD1 regime compared to the "no FCD" regime in the FRET experiments [Fig. 4.2(b)]. For the two cases tested in the "no FCD" regime, the response for the 2.5μM injection concentration showed a slightly higher response compared to the 0.75μM case, but the profiles, though both exhibiting a weak chemotactic response, do not coincide with each other. On the contrary, for the FCD1 regime, the three temporal CMC profiles are indistinguishable for the three injection concentrations tested. Similarity can be observed not only in the maximum initial responses (maximum CMC for the three cases are 0.31±0.02, 0.28±0.09 and 0.25±0.09, respectively), but also in the time at which the peak response is observed (1.25 min for all the three cases). These results show that a ~12 fold change in the concentration of a chemoattractant pulse invokes similar migration behavior in *E. coli* AW405 when the ratio between the injection and ambient concentrations remains constant.
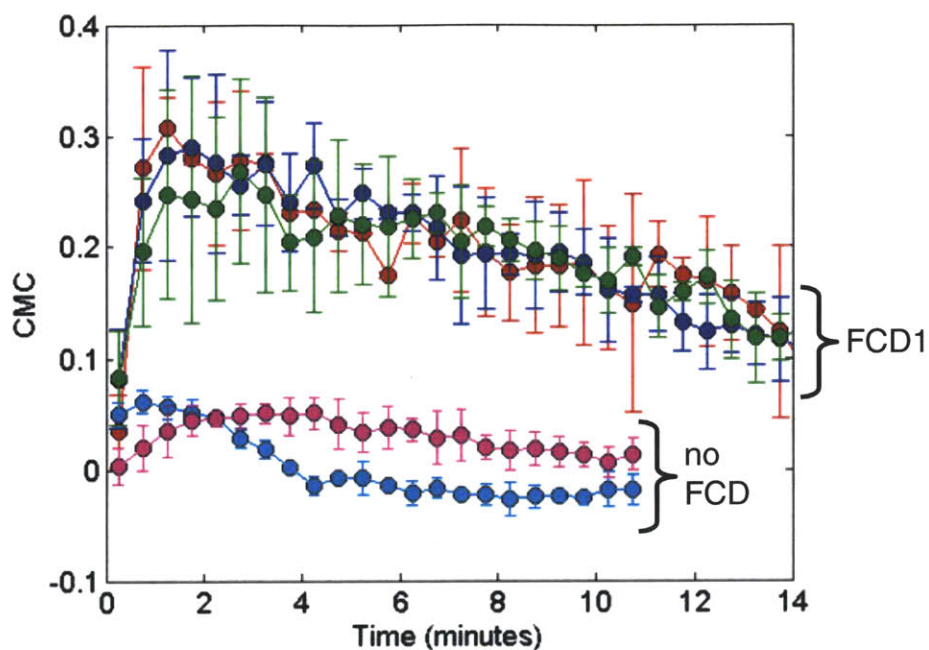
Figure 4.11 The Chemotactic Migration Coefficient (CMC) as a function of time, computed from the chemotactic response of swimming cell populations within and outside the FCD1 regime for the unsteady nonlinear gradients. The red, blue and green filled circles correspond to the CMC values for initial injection concentrations of 36, 128 and 456 μM MeAsp, respectively, all within the FCD1 regime. The cyan and magenta filled circles correspond to the CMC values for initial injection concentrations of 3 and 10 μM MeAsp, respectively, both within the "no FCD" regime. The chemotactic response was strong in the FCD1 regime compared to the "no FCD" regime, resulting in higher CMC values for FCD1. Within the FCD1 regime the CMC time series were essentially identical for the three cases tested. The two CMC profiles for the "no FCD" regime, though both showing a weak chemotactic response, were distinct from each other throughout the duration of the experiment. These observations in the unsteady nonlinear gradients further corroborate the findings from the FRET experiments.

4.5 Conclusion and discussion

Using a previously developed microfluidic device [71] to create controlled, steady spatial gradients of a chemoattractant, it was shown that the chemotactic performance of *E. coli* in linear gradients was invariant within the same two concentration regimes where the FRET measurements show FCD to hold. Furthermore, not only the steady state spatial distribution of the bacteria, but the whole time course of their distribution was found to be invariant within these two regimes. Using microfluidic devices to generate unsteady nonlinear gradients [73], it was shown that the migration behavior showed similar invariant properties when bacteria are exposed to chemoattractant pulses having the same fold change relative to the ambient concentration. In the steady linear gradient, FCD was demonstrated over a ~87 fold change in

mean ambient concentration, from 0.12 mM to 10.3 mM, in two distinct regimes confirming the conclusions from recent FRET experiments. For the unsteady nonlinear gradients, the bacterial response was found to be invariant over a ~12 fold change in chemoattractant pulse concentrations, from 0.036 mM to 0.456 mM (the FCD1 regime). The "no FCD" regime in both cases was characterized by weak bacterial response. These results indicate that FCD, which appears to play a key role in ERK, Wnt and other signaling pathways in eukaryotes [72, 146, 147], is also a property of the chemotaxis signaling system of E. coli. These results confirm the theoretical predictions of Shoval et al. [72], for the case of swimming populations. Moreover, these experiments represent an extension of the pioneering experiments by Mesibov et al. [98] and Kalinin et al. [67] for swimming populations, where the bacterial response to a rescaled gradient were observed at a given point in time. In this study, the entire time evolution of the response was characterized and compared for different scaled gradients. Microfluidics allowed us to generate and manipulate the chemoattractant field with great precision, while videomicroscopy enabled us to acquire data with high spatial and temporal resolution.

Quantitative analysis of FCD in swimming populations was done by comparing the bacterial distributions over time. The motivation for using the population-scale response was based on the argument that, if a surface-attached cell shows FCD in FRET experiments, a swimming bacterium would perform equally well in climbing a chemoattractant gradient under similar rescaled conditions. Since a swimming bacterium continuously adapts to changing attractant concentrations in a spatial domain, any differences in adaptation rates under different gradients would affect the bacterial distribution and its temporal evolution. Since the bacterial distributions have been found to evolve identically within each of the two FCD regimes, this implies that not only the response amplitude but also the time scale of adaptation of bacteria under these particular set of gradients are identical. This has been found to be true for steady linear gradients as well as for unsteady nonlinear gradients, as long as the range of concentrations is within a particular FCD regime.

Since FCD was tested in a swimming population within a microfluidic device, the swimming speed of bacteria as well as its adaptation rate in that particular concentration field will, together, define the biological timescale of the response. In the steady linear gradient generator, the

100

physical timescale for gradient generation can be conveniently decoupled from the biological timescale of the response. Therefore, even slow-swimming or slowly adapting organisms will exhibit a response as long as sufficient observation time is allowed. In contrast, for experiments in unsteady gradients, both biological and physical timescales become important in determining whether the chemotactic response elicits an accumulation of bacteria, since diffusion of the chemoeffector imposes a restriction on the observation time frame. Since the peaked concentration profile in the microchannel will inexorably diffuse to homogeneity within a time-scale of $\sim W^2/D$, fast-swimming or quickly adapting bacteria will show larger accumulations than slow-swimming or slowly adapting ones. In the unsteady experiments, *E. coli* RP437, which performed well in the steady linear gradients (reaching a maximum response in both FCD regimes in ~20 minutes), did not show a measurable response (data not shown), likely because their chemotactic performance was too weak for a population to significantly climb the gradient before the gradient reduced to homogeneity. Therefore, for the unsteady gradient case, *E. coli* AW405, a relatively fast-swimming motile strain (swimming speed ~25 μm/s), was used. This strain showed a marked chemotactic accumulation within the diffusion time scale of the chemoeffector. This is in line with previous results, that showed that fast-swimming bacteria can have a decisive chemotactic advantage over slow-swimming ones in ephemeral nutrient patches generated using this microfluidic device [14].

How could bacteria have evolved a chemotaxis strategy that is invariant to fold changes in their resource concentration? The physicochemical nature of their natural habitat may be a probable cause. Microorganisms inhabit a myriad of environments and the behavior, adaptability, and survival of organisms depends critically upon their capability to formulate appropriate responses to chemical and physical environmental cues in their natural environment. For instance, marine microbes often experience a heterogeneous and nutrient-deprived environment, characterized by sporadic and ephemeral microscale (μm –cm) patches of nutrients, generated from several sources including the lysis of cells [12, 138], excretions and exudations from other organisms [149, 150], and leakage of substrates from sinking organic particles [151]. Hence, at sub-centimeter scales, the ocean is characterized by marked nutrient heterogeneity where localized high concentrations of dissolved organic matter (DOM) occur within otherwise highly oligotrophic conditions. Typically, the DOM released by phytoplankton as point sources and

diffusion from this source allows bacteria to gain access to it. The amplitude of the concentration field resulting from diffusion from a source of attractant at r_0 is linear in the concentration u_S of the source, if a Neumann (i.e., no-flux) or a Drichlet problem (with boundary conditions appropriately scaled) is posed. Diffusion and zero conditions at infinity, for example, result in a Gaussian $u(r, t) = u_S (4\pi Dt)^{3/2} exp(-(r-r_0)^2/(4Dt))$, which is linear in u_S. Therefore, by scaling the source by a factor "p" into $p\ u_S$, the gradient field also scales by this factor. This implies that the location of the source determines the nutrient field only up to multiplicative uncertainty; the position of the source determines the shape of the field. Strength of nutrient sources in the natural environment can be extremely variable and search patterns in organisms that have the FCD property result in behaviors that are robust to large changes in background levels. In the marine environment the nutrient conditions change dramatically during phytoplankton blooms, which are periodic events in which phytoplankton populations grow exponentially. During a bloom, which unfolds over days, phytoplankton cells grow rapidly and release considerably increased amounts of DOM. Hence, both the background conditions and the high-concentrations within microzones are rescaled under bloom conditions. An FCD response would enable bacteria to respond equally effectively under normal conditions and blooms conditions. In general, it would enable bacteria to take advantage of the huge range of concentrations they are challenged within the ocean. Also, since the span of these microscale nutrient patches is limited by the erosive effects of diffusion, obtaining metabolic gains from a patch then becomes a race against time [12, 14, 16, 138]. An efficient exploitation of these dynamic and patchy nutrient landscapes by motile bacteria could have profound consequences for biogeochemical transformation rates [15].

In this study the FCD property has been demonstrated for *E. coli*: it remains to be determined how ubiquitous this property is among prokaryotes. It is only recently that FCD has been demonstrated in the transcriptional networks of eukaryotic cells [147, 152], where it results from a specific network topology, known as incoherent feed-forward loop [146]. The topology of *E. coli*'s chemotaxis signalling network, as described in the model of Tu *et al.* [33], though different from these transcriptional networks, was found on theoretical grounds to exhibit the FCD property [72]. This was tested experimentally in this study.

Since the chemotaxis signalling pathway is a highly conserved feature among prokaryotes, it is likely that bacteria other than *E. coli* also exhibit FCD. However, the molecular architecture of other prokaryotes is not as well known as *E. coli*'s and therefore performing molecular manipulations to incorporate appropriate proteins to conduct *in vivo* FRET measurements may be an arduous path to follow. Population-scale behavior of swimming cells can then be a more attractive approach to study the scaling invariance of the chemotactic response. Thus it can be envisaged that microfluidic techniques will be instrumental in studying chemotaxis and FCD in bacteria other than *E. coli*, particularly when less molecular knowledge is available.

Chapter 5

Chemotactic aggregation and predation in microfabricated landscapes[a]

5.1 Background

Predator-prey interactions affect population dynamics from the level of ecosystems to that of local communities. Predation governs energy flow among trophic levels and can drive biogeochemical cycles [153]. Predation can alter the demographic structure of prey populations by potentially causing their extinction or conversely by promoting the coexistence of less competitive species. One of the biggest challenges in contemporary ecology is to better understand the factors that confer stability to communities and ecosystems. The stability of a predator-prey system depends on a complex set of factors, both environmental (e.g. patch quality, heterogeneity) and biological (e.g. demographic rates). When stabilizing elements prevail, the prey and predator populations undergo periodic oscillations. When predators overexploit prey, oscillations grow and the resulting boom-and-bust cycles can lead to extinction [154-156].

Natural habitats are often heterogeneous in terms of (1) spatial structure and (2) resource availability. These heterogeneities span a range of scales, from the landscape to the single habitat: they can have profound effects on predator-prey interactions and are an essential component of many questions in ecology and conservation [157-159]. Many ecosystems are spatially fragmented, with separate populations inhabiting each patch. But if these populations are linked by dispersal, metapopulations can emerge [160]. This means that even if the local population in a certain patch goes extinct because of the loss of all individuals due to random demographic events, the empty patch can be re-colonized by populations from adjacent ones through dispersal [157, 161, 162]. This process leads to an increased persistence time (i.e. time to extinction). Similar dynamics can also emerge in a heterogeneous resource landscape, where aggregation of prey populations (e.g. 'hot-spots' of bacteria formed by chemotactic aggregation towards nutrients) affects the foraging capabilities and growth rates of higher organisms. In a metapopulation context, high-quality habitats (sources) produce large populations and are often sources of emigrants, whereas low-quality habitats (sinks) experience negative growth rates and tend to receive immigrants [163]. The resulting source-sink dynamics can increase regional persistence, since emigrants from source habitats can rescue extinction-prone populations in sink habitats [164]. Furthermore, preferential predation on prey-rich patches ('aggregation effect') has a stabilizing effect [165, 166], relieving sink patches from predation and increasing their

likelihood of avoiding extinction.

Mathematical models have shown that the structure of a landscape can affect the outcome of species interactions, particularly predator-prey persistence [158, 167-170]. Early laboratory studies revealed that subdivision of the habitat promotes predator-prey coexistence [155, 171, 172]. A number of experimental systems have been used since, including host-parasitoid pairs [173-175], greenhouse mites [176, 177], and protists [178-180]. These experiments have generally confirmed that extended persistence is due to the asynchrony in the dynamics of local populations, which diminishes the risk of regional extinction [181]. However, there is no conclusive agreement on whether spatial structure universally promotes predator-prey coexistence, as some studies report the opposite conclusion [182, 183]. The apparent anomaly in experimental observations can be attributed to the previously unaccounted mechanism of the dispersal of species (in many cases active, i.e. determined by the organisms' own movement), which can vary in space and time and can be affected by the habitat topology and local population density.

At very low dispersal rates, each patch behaves independently and empty patches are not recolonized often enough to balance extinctions [184, 185]. At the other extreme, very high dispersal rates also decrease persistence, because they synchronize local populations, fostering the simultaneous extinction of all local populations [184, 186, 187]. Predators are known to change their movement behavior in response to prey densities (i.e. increased swimming speed in response to low prey densities [179, 188]) but only in one instance, this behavioral change was used to explain the otherwise confounding results regarding the fate of populations in a spatially structured predator-prey microcosm [179]. It can be hypothesized that this dependence on movement behavior could account for the opposite effect of fragmentation in different experiments, stabilizing in many cases [155, 171, 179, 189, 190], but destabilizing in others [182, 183]. It has thus been suggested that the details of the organism's movement behavior should be included in explaining the effect of habitat fragmentation on population dynamics [183]. The simultaneous acquisition of population-scale and behavioral data in predator-prey studies has to date been limited by the lack of an appropriate experimental system, as existing systems have been unable to quantify movement and thus dispersal [191].

In this chapter, the effect of geometric heterogeneity and resource heterogeneity is explored in the context of a microbial predator-prey system, consisting of a species of bacteria and a species of protists, within a microfluidic experimental platform capable of simultaneously quantifying population dynamics and movement behavior. Because of their rapid generation times and the simplicity of their manipulation, microbial systems have been used to study a wide range of ecological processes [192-196]. On the other hand, the scale of microfluidic devices is ideal for application to microbial ecology, and a range of microbial processes has been successfully studied with microfluidics, including quorum sensing [197], chemotaxis [14, 70, 89], collective dynamics [198], and motility in confined environments [121, 199]. Also, spatially structured microfluidic landscapes have recently been applied to the study of metapopulations of single [200] and competing bacterial species [201], and to demonstrate that microscale spatial structure enables coexistence [202]. There are three main advantages to the microfluidic model system: (i) ability to accurately manipulate the spatial landscape; (ii) visualization of microbial dynamics at single-cell resolution; and (iii) effortless data collection through videomicroscopy and automated image analysis. These advantages enable a large number of experiments, on-chip replication and controls, and systematic exploration of a wide range of parameters.

In this study, a linear gradient of prey nutrients/chemoattractants was imposed on the prey population to trigger a chemotactic response, which in turn generated a gradient in prey population density in a microfluidic chamber constructed with varied spatial configurations. The spatial predator-prey distribution along with the movement behavior of the organisms were tracked over time, to gain insight on the effect of spatial and/or resource heterogeneity on the predator-prey dynamics.

5.2 Model organisms and their behavioral characteristics

For the microbial predator-prey model system, the bacterium *E. coli* (AW405) was selected as the prey and the ciliated protist *Tetrahymena pyriformis* (strain W) was selected as the predator. The *T. pyriformis – E. coli* model system has been the subject of numerous previous studies, both experimental [203-205] and mathematical [206] and for both of these organisms abundant behavioral and physiological data is available [23, 203-209].

E. coli swims at ~30 μm s^{-1} using 4–10 helical flagella in a characteristic 'run and tumble' movement pattern [126, 140]. At the population scale, this results in diffusive dispersal. Delaying the tumble when the swimming direction is favorable (e.g. up a resource gradient) results in net motion in that direction – or 'taxis' – at a rate of 5-35% of the swimming speed [70]. For a chemical gradient, this is 'chemotaxis'. For optimal detection, *E. coli* AW405 expressing GFP (Green Fluorescent Protein) with epifluorescent visualization [200] was used [Fig. 5.2(b)].
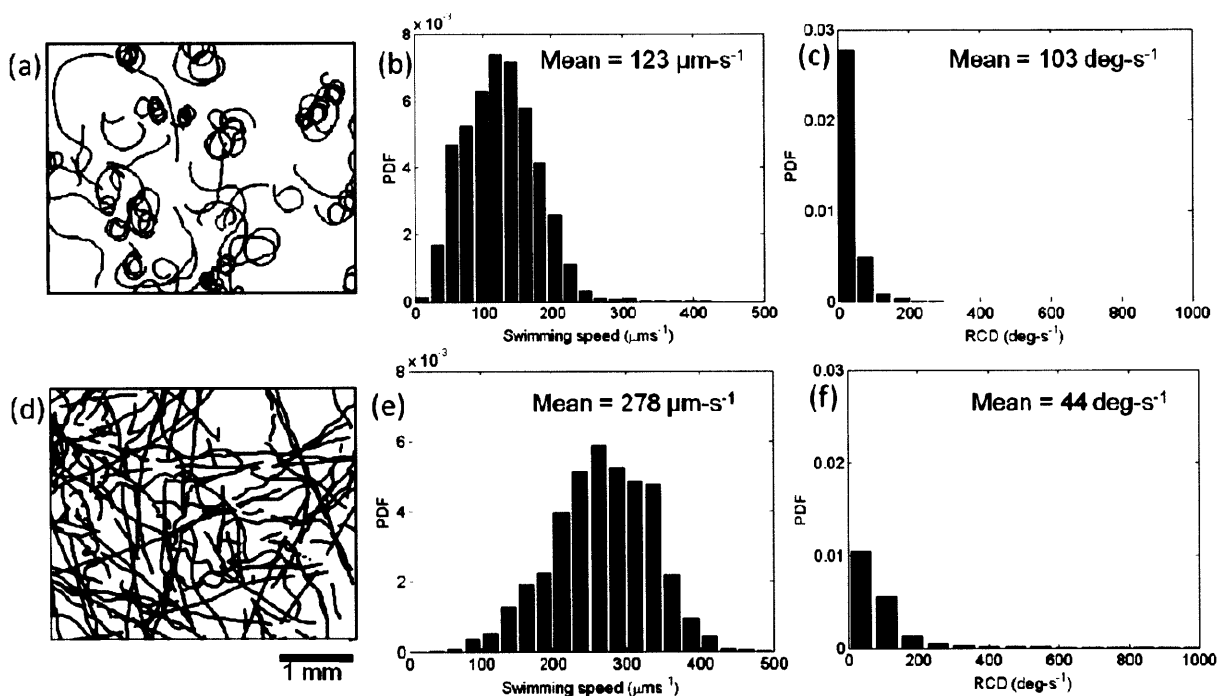
Figure 5.1 Swimming behavior of *Tetrahymena pyriformis* in different physiological conditions. (a) Tracks of *T. pyriformis* cells in the presence of bacterial cells show curvy trajectories having an average swimming speed of 123 μm s^{-1} and an average rate of change of direction (RCD) of 103 deg s^{-1}. The tracks were constructed from a 20 s movie captured at 10 frames/s under a 2× objective. (b,c) The probability density function (PDF) of the swimming speed and RCD for the trajectories shown in (a). (d) Tracks of *T. pyriformis* cells in the absence of bacterial cells show relatively straight trajectories having an average swimming speed of 278 μm s^{-1} and an average RCD of 44 deg s^{-1}. (e,f) The PDF of the swimming speed and RCD for the trajectories shown in (d).

Tetrahymena pyriformis is a ~40×20μm, pear-shaped, ciliated protist [210, 211] [Fig. 5.2 (a)], which occupies diverse ecological niches throughout the world's freshwater habitats [211]. It has

fast generation times (2.5–7 hr), with optimal growth at 30–35 °C [212, 213]. It can be cultured on a liquid diet, but preferentially feeds on bacteria like *E. coli* [203-205, 208, 209], which it detects through chemical signals (primarily amino acids [214, 215]) and ingests via a 10×6 μm pyriformal buccal aperture [211]. The ingestion rate, ~100–1000 bacteria/hr [216],varies with both the ciliate and the bacterial population densities in a known fashion [217]. *T. pyriformis* has a monomorphic life cycle that facilitates detection and size measurements. It can adjust its shape owing to its substantial morphological plasticity [211] and it shrinks in volume by ~50% after 4 hours of starvation due to the shedding of cytoplasmic reserves [213]. Starvation also induces division, causing an increase in cell numbers and a decrease in size [216]. *T. pyriformis* swims in smooth trajectories [Figs. 5.1(a,d)] at 100–250 μm s^{-1} using 19 rows of cilia [211]. The speed and tortuosity of trajectories varies with the availability of prey cells in the culture. Preliminary experiments yielded a mean swimming speed of 278 μm s^{-1} and a rate of change of direction (RCD) of 44 deg s^{-1} for cells swimming in a culture devoid of bacteria [Figs. 5.1(d-f)]. But a lower swimming speed (123 μm s^{-1}) and a higher turning rate (mean RCD 103 deg s^{-1}) were measured for the same culture when bacterial cells were added [Figs. 5.1 (a-c)]. The former scenario results from starvation and favors dispersal.

(a)

Tetrahymena pyriformis

50 μm

(b)

T. pyriformis (predator)

E. coli (prey, bright dots)

100 μm
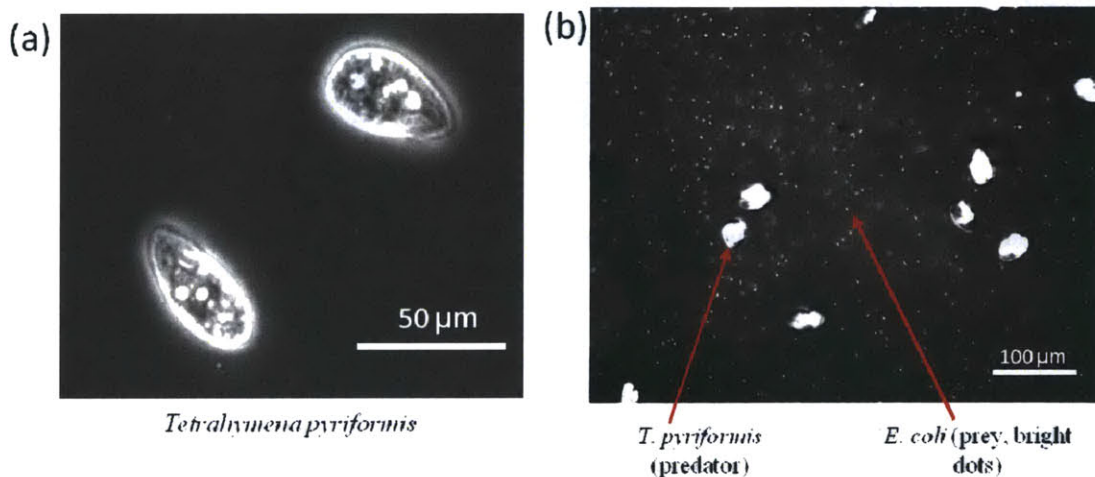
Figure 5.2 Phase contrast and fluorescent images of the predator and prey. (a) Phase contrast image of *Tetrahymena pyriformis* cells. Food vacuoles can be seen inside the cell body as white circular spots. (b) Fluorescent image of both *T. pyriformis* and *E. coli* taken with a 20× objective. Bacterial cells appear as small dots while the larger bright spots are the protists. The number of cells can be counted automatically through image analysis.

5.3 Materials and methods

5.3.1 Organism cultures and growth protocols

Escherichia coli cells (AW405 strain, a gift from Howard Berg, Harvard University, transformed with GFP (Green Fluorescent Protein) plasmid in the Laub lab at MIT) were grown in a culture growth medium in an orbital shaker at 34°C at 220 rpm and harvested at exponential growth phase (OD_{600}~0.5), which took approximately 5 hours. The growth medium was Tryptone Broth (1% Tryptone, 0.5% Sodium Chloride) supplemented with the inducer anhydrotetracycline (IBA Biotagnology, Olivette, MO, USA), which was added to the culture media to a final concentration of 12 μg/ml.

Axenic cultures of *Tetrahymena pyriformis* (CCAP 1630/1W) were grown in low-light conditions at room temperature (25°C) in PPY (Proteose Peptone Yeast Extract) medium (2% Proteose peptone, 0.25% Yeast extract). The cultures were incubated in 12 ml volumes for at least two weeks before they were used for experiments. Before the start of experiments, a 2 ml volume of the culture was concentrated 10 times by centrifuging at 2000g for 5 minutes. A 10-15 μL of dense *E. coli* culture (concentrated 10 times by centrifuging at 2000g for 5 minutes) was resuspended in the concentrated *Tetrahymena* culture to make the mixed culture, which was used in the experiments.

5.3.2 Experimental setup

The predator-prey microcosm was studied in a series of "microfluidic lattice" channels designed using CAD (Computer Aided Design) software (Autodesk Inc., CA, USA), which enables one to effortlessly produce multiple variations. Channels were fabricated using soft lithography [64] and rapid prototyping using Polydimethylsiloxane (PDMS, Sylgard 184; Dow Corning, MI, USA), a polymer that is transparent, inert, biocompatible, and permeable to gases. Inlet and outlet holes were punched in the PDMS using a 20 gauge sharpened luer tip (BD, NJ, USA), and tubing attached to a syringe was used to inoculate the organisms.

Two different categories of lattice structures were fabricated. The first type consisted of a set of three separate 3 mm long, 0.6 mm wide rectangular habitats arranged parallel to each other [Fig.

5.3(a)]. The other one comprised several sub-millimeter rectangular patches (600 μm × 450 μm) connected by corridors of length 100 μm and variable width, s [Fig. 5.4(a)]. The degree of spatial restriction can then be denoted by s/L, where L is the largest dimension of an individual patch (in this case, the width $L = 600$ μm). s/L was varied from 0.025 to 1.0 for different experiments, where $s/L = 1.0$ refers to an un-constricted environment, the same used in the first category. The depth of the lattice structure was 100 μm in all cases.
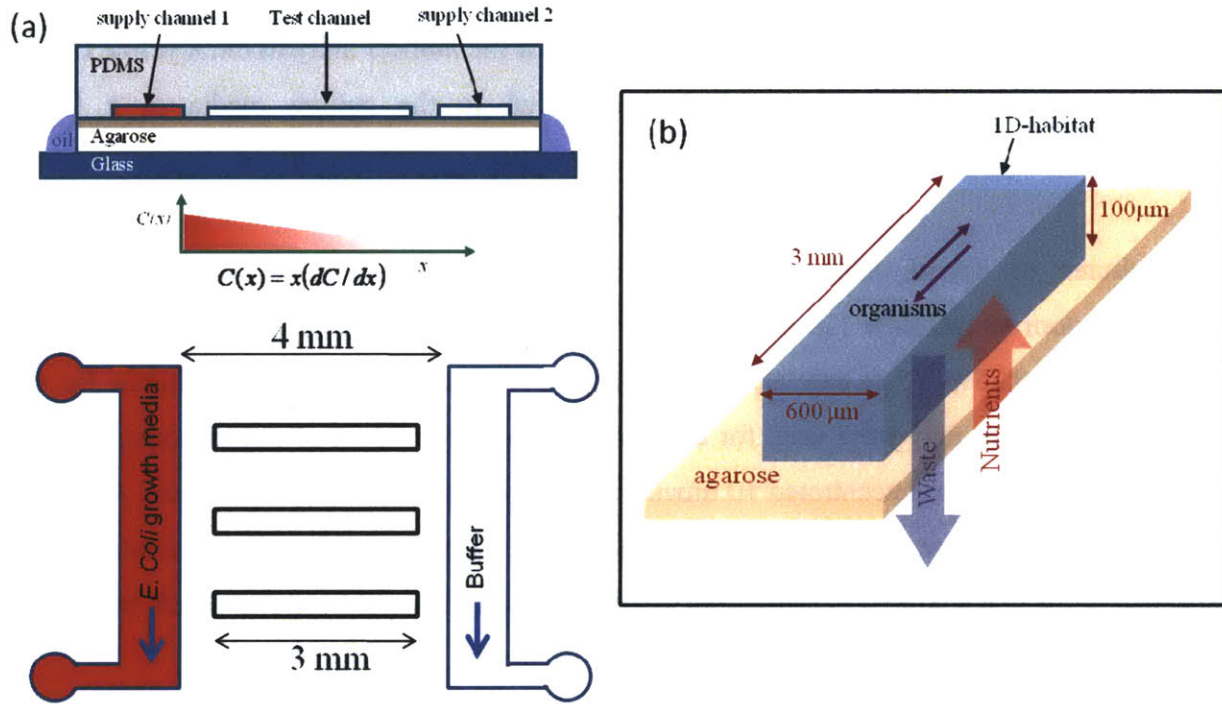
Figure 5.3 Schematic of the microfluidic device used to generate a simple heterogeneous resource landscape. (a) Schematic of a 1D microfluidic lattice with single, spatially homogenous habitats. Three parallel habitats, each 3 mm long and 0.6 mm wide, are placed in between the two supply channels. Nutrients and buffer are flown in the two supply channels creating a linear concentration profile, $C(x) = x\,dC/dx$, in the agarose. **(b)** Schematic of a single habitat. Nutrients are supplied to and wastes are removed from the habitat by diffusion through the porous agarose layer underneath, which in turn is fed by the supply channels.

To supply solutes (nutrients and/or chemoattractants) to the patches, a hydrogel-based technique, which was recently developed and applied to deliver chemoattractants to *E. coli* by diffusion (Chapter 3)[71], was adopted. The method is based on two supply channels in the PDMS, one on either side of the lattice but neither connected to it [Figs. 5.3(a), 5. 4(a)]. A syringe pump (PHD 2000, Harvard Apparatus, MA, USA) maintains a small flow rate (5 μl/min) in each supply

channel. Underneath the PDMS is a 1 mm thick agarose layer (3% w/v), a porous hydrogel, which serves as the bottom of both the lattice and the two supply channels. Solutes from the supply channels diffuse into the agarose layer and from there into the patches. A thin film of mineral oil was used to cover the exposed regions around the agarose to prevent fluid loss due to evaporation and drying.
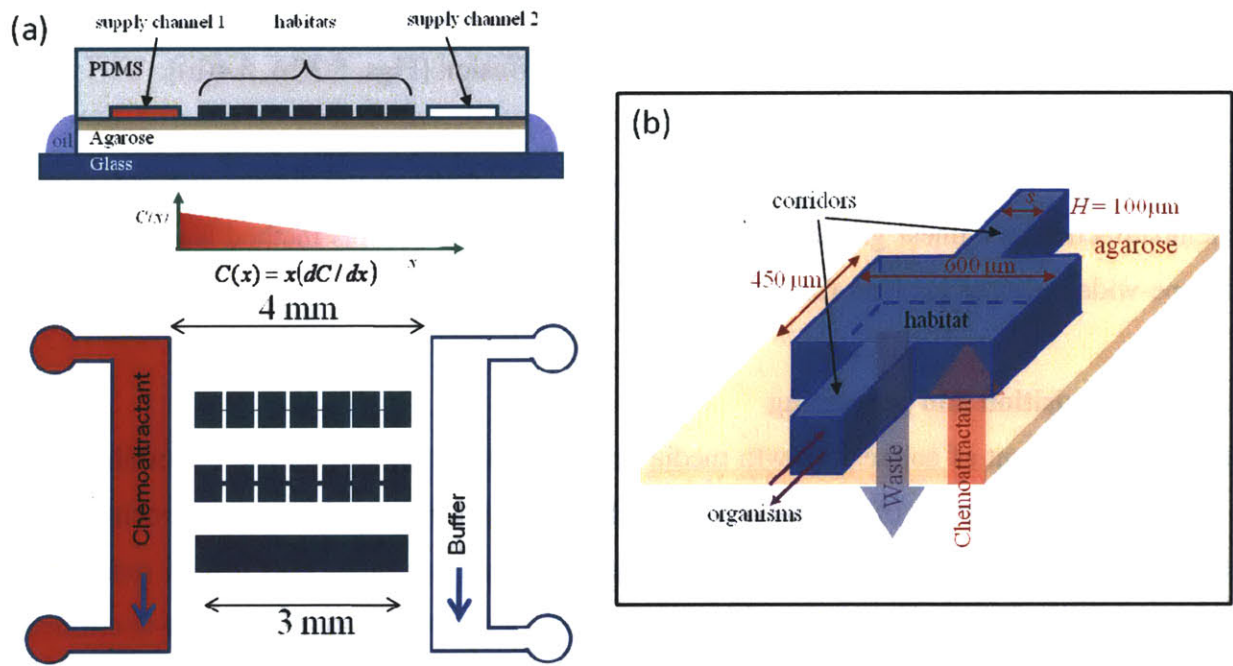
Figure 5.4 Schematic of a microfluidic device to generate spatially structured habitats. (a) Schematic of a microfluidic lattice with three habitats made of rectangular patches with various degrees of connectivity. Each of the patches is 600μm × 450μm large, has corridors of length 450 μm and widths 15, 50 and 600 μm (the third one is in fact a single, large rectangular habitat). Nutrients and buffer are flown in the two supply channels creating a linear concentration profile, $C(x) = x\, dC/dx$, in the agarose. **(b)** Schematic of a single rectangular patch, with corridors of width s that allow dispersal of organisms. Nutrients are supplied to and wastes are removed from the habitat by diffusion through the porous agarose layer underneath, which in turn is fed by the supply channels.

A steady, linear solute concentration profile, $C(x) = x\, dC/dx$ (the solution to the one-dimensional diffusion equation) in the agarose can be generated by using one of the supply channels to flow solutes while the other one flows buffer. This process requires a time (set by diffusion) $T_S \sim W^2/D \approx 5$ hr, where $W \approx 4$ mm is the distance between the supply channels and $D \approx 10^{-9}$ m^2 s^{-1} is the nutrient diffusivity in agarose. The solute concentration inside each patch mirrors that in the underlying agarose and lasts indefinitely because the channels are continuously replenished, creating a steady linear solute concentration profile across the patches (the concentration is

113

uniform parallel to the supply channels). Actual gradients deviate slightly from linear, as discussed in detail in Chapter 3.

The organisms were inoculated after the gradient was formed in the patches. The injection of the organisms momentarily disrupts the concentration, but the disruption only lasts a time $H^2/D \approx 10$ s, the time for nutrients to diffuse from the agarose into each patch and across its height H (= 100 μm). The agarose layer also removes waste products by diffusion [Figs. 5.3(b), 5.4(b)].

Previous experiments showed that the distribution of *E. coli* peaks at the highest concentrations of chemoattractant in a linear gradient [71], hence it is expected that this method would create a landscape-wide resource gradient for the predator.

5.3.3 Data acquisition and processing

After a linear gradient of solutes (growth media or chemoattractant) was allowed to establish in the agarose, mixed cultures of *T. pyriformis* and *E. coli* were injected into the microchannels. Thereafter, the inlets were sealed with a cover slip to prevent any flow. This instant represents the start of the experiment (time $t = 0$). Experiments were performed using a computer-controlled inverted microscope (TE2000-E, Nikon, Japan), equipped with a 1600×1200 pixel, 14-bit CCD camera (PCO 1600, Cooke, MI, USA). Data collection was fully automated, with a script programmed to move a computer-controlled stage at previously defined spatial coordinates to acquire either single epifluorescent images (using a FITC filter) or record movies (in phase-contrast). The motion of the stage, although rapid, produces no disturbance in the lattice (because of the shallowness of the channels).

Data on the swimming of *T. pyriformis* was acquired using phase-contrast movies with a 2× objective. Each movie was a 300-frame sequence of images, acquired at 10 frames/s. The field of view under a 2× objective was 6 mm × 4.5 mm and typically covered all the patches in a habitat with a single shot. *E. coli* was too small to appear in the 2× movies, making for clean counting and tracking of *T. pyriformis*. Predator trajectories were obtained from 2× movies with an in-house, Java-based tracking software (BacTrack) and were used to compute swimming velocities and fluxes of organisms among patches.

Data on the bacterial distribution were collected in two different ways, for the two types of habitats shown in Figs. 5.3(a) and 5.4(a). For the patches shown in Fig. 5.3(a), three subsequent phase-contrast movies, each of them consisting of 40 frames taken at 10 frames/s using a 10× objective, were captured to span the 3 mm length of the patch. Bacterial distributions were obtained by automatic size-based segmentation performed in IPLAB (BD, MD, USA). For the patches shown in Fig. 5.4(a), one epifluorescent image (FITC filter) with a 20× objective was captured for each of the patches and eventually bacterial distributions were obtained by an image analysis routine using MATLAB (Mathworks, MA, USA). The bacterial distribution data were collected at 10 min intervals starting from t = 10 min, a delay which accounts for the time taken to setup the device for image acquisition.

5.4 Results

5.4.1 Effect of predation in a heterogeneous resource landscape

A steady linear gradient of Tryptone Broth (*E. coli*'s growth medium) was maintained along a 3 mm long, 0.6 mm wide and 0.1 mm deep microchannel [Fig. 5.3] and the mixed culture of T. *pyriformis* and *E. coli* was injected in the channel. The natural affinity for *E. coli* towards its growth medium triggered a chemotactic response, resulting in a spatial distribution of cells skewed in the direction of the 'source channel'. This, in turn, would provide a heterogeneous prey landscape for the predators to forage on. Since the growth medium will also allow the bacteria to continue growing, whether or not the bacterial population goes extinct would depend on the competition between growth and predation. It was confirmed that Tryptone Broth did not elicit a chemotactic response in T. *pyriformis*.

Fig. 5.5 shows the time series of the bacterial abundance in the channel for two different predation pressures (i.e. concentrations of predators), along with a control case (no predators). These curves are obtained by plotting, over time, the total cell count in the channel, B, normalized by the total cell count at t =10 min, B_0. As expected, in the absence of predation *E. coli* continues to grow. The average doubling time over the first 100 minutes was 50 min, which is quite typical for *E. coli* at room temperature (e.g. a doubling time of 56 min was reported at 26°C [218]).

On the other hand, when predators are present the increase in cell numbers due to growth is balanced by predation, which results in different dynamics depending on the prey to predator ratio, B_0/T_0, where T_0 is the number of *Tetrahymena* at the start of the experiments (i.e. at $t = 10$ min). For a low B_0/T_0 ratio, the bacterial numbers decrease and reach a steady state where growth is compensated by predation. For higher B_0/T_0, somewhat different dynamics emerge: an initial slight increase in prey cell numbers is followed by a dip, which indicates increased predation, after which growth overcomes predation and bacterial cell numbers begin to rise. These results show, as expected, that the fate of the bacterial population depends on the predator to prey ratio.
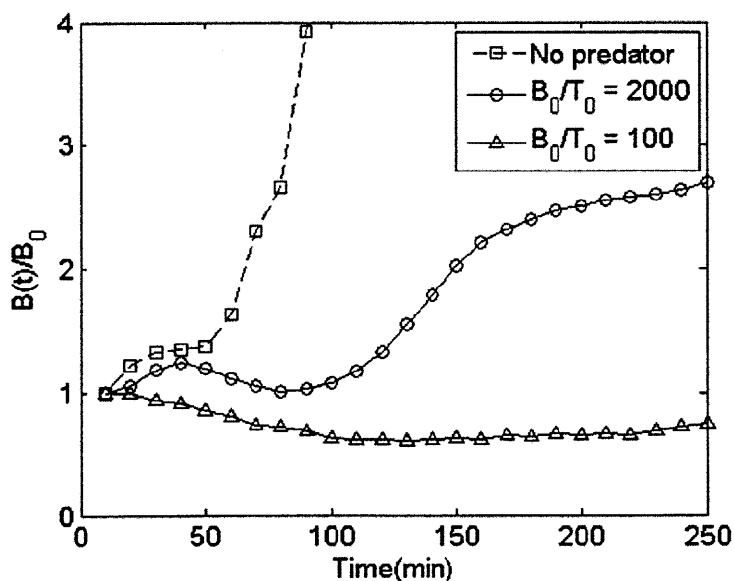
Figure 5.5 Bacterial abundance (relative to initial abundance) at different levels of predation pressure. The total cell count results from the competition between predation and growth. When no predators are present, bacterial growth continues unabated, while the presence of predators may generate oscillatory behavior (B_0/T_0 = 2000) or drive the population towards a low abundance (B_0/T_0 = 100).

Bacterial distributions inside the chamber showed markedly different characteristics in the two predation pressure regimes. Fig. 5.6 shows the time series of the Chemotactic Migration Coefficient (CMC), for the two regimes. The CMC is a dimensionless measure of the degree of departure from symmetry in a non-uniform distribution and can be defined as:

116

$$CMC = \frac{1}{L/2} \frac{\int_{-L/2}^{L/2} x'B(x')dx'}{\int_{-L/2}^{L/2} B(x')dx'}$$

where, x' is the direction across the channel (i.e. along the gradient), with $x' = 0$ at mid-width, and the integral extends over the entire width of the channel, L. A uniform spatial distribution of cells corresponds to CMC = 0, while aggregation of cells towards $x' > 0$ corresponds to CMC > 0. For both regimes, the bacterial distribution along the channel is initially nearly uniform, resulting in CMC values ~0. For the lower predation pressure regime ($B_0/T_0 = 2000$) the distribution becomes gradually skewed in the direction of the nutrient gradient (towards the right, in the image), reaching a minimum of CMC = 0.23 at $t = 110$ min. After this time, growth starts to overcome predation, the number of bacterial cells increases, though some degree of chemotactic aggregation persists up to $t = 200$ min. For the high predation pressure regime ($B_0/T_0 = 100$), the distribution becomes only marginally skewed in the direction of the nutrient gradient and chemotactic aggregation is almost non-existent over the entire period, with a minimum CMC = 0.1 at $t = 100$ min.

In contrast, if there is no predation pressure, extremely strong chemotactic aggregation towards the high growth media concentration can be observed for the duration of the experiments [Fig. 5.7], with a minimum CMC of 0.65 at $t = 90$ min. These results indicate that predation has a significant impact on the degree of chemotactic aggregation and that the latter, while representing a fitness benefit in terms of nutrient uptake for a motile species of bacteria, can also represent a hazard because of enhanced predation. Predation tends to minimize the heterogeneity of the bacterial distribution ('eat the winner') and the higher the predation pressure, the higher will be the probability that an initially patchy distribution of bacteria will become homogeneous. There was no visible difference in swimming behavior of *T. pyriformis* cells between the two different regimes nor was there any indication that they were clustering near the regions of high concentrations of bacteria. Therefore, it is likely that in these experiments the predation pressure acted uniformly over the entire bacterial population and the resulting bacterial distribution was not a result of preferential predation.
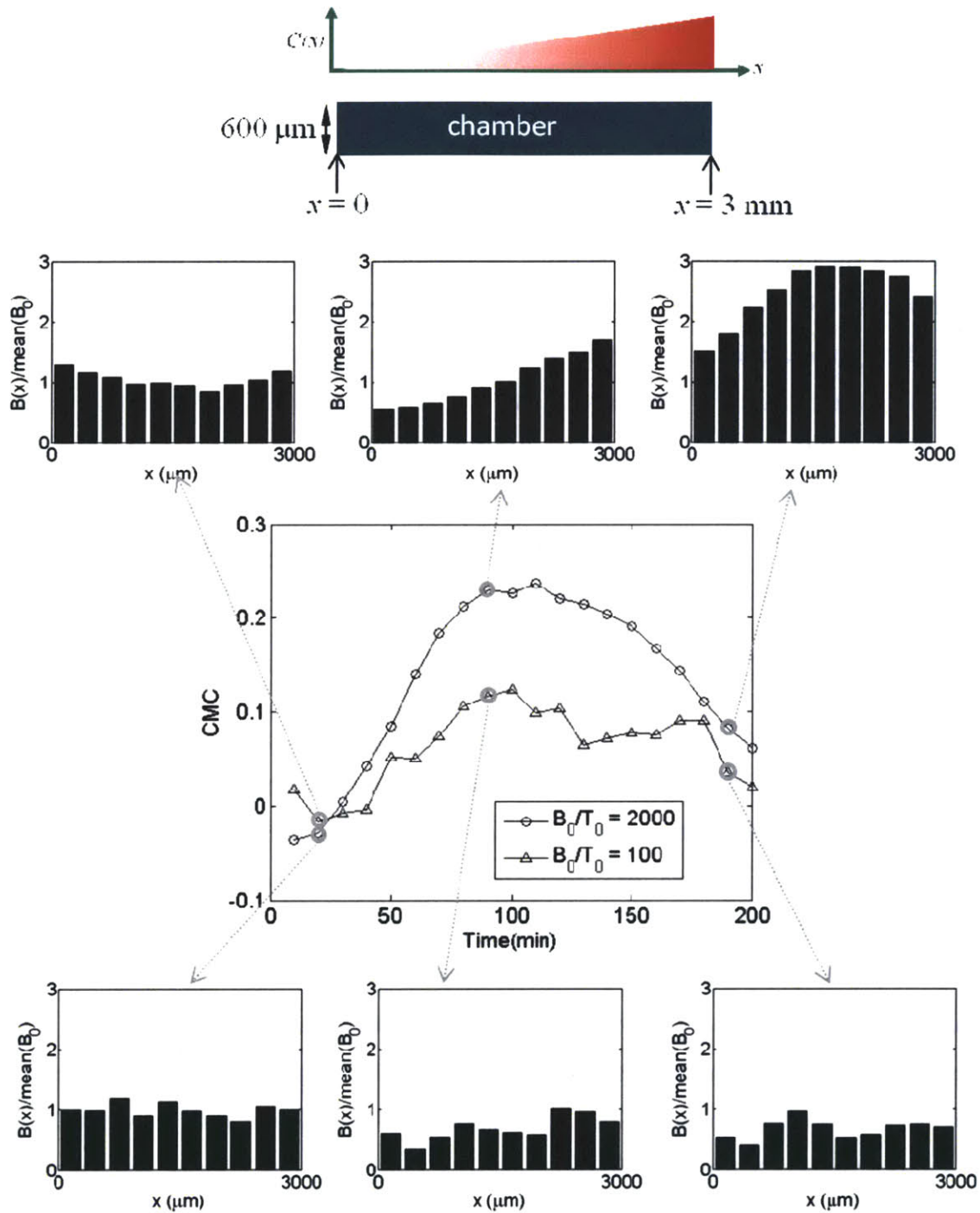
Figure 5.6 Time series of the Chemotactic Migration Coefficient (CMC) for the two different predation pressure regimes. CMC measures the distribution asymmetry of *E.coli* and is computed from the bacterial distribution $B(x)$ along the 3 mm long microfluidic chamber. The low predation pressure regime ($B_0/T_0 = 2000$) shows markedly higher asymmetry in the distribution throughout the experiment, compared with the high predation pressure regime ($B_0/T_0 = 100$). This is also evident in the bacterial distribution, $B(x)$, shown for the two regimes at t = 20, 90 and 190 minutes. The bacterial distribution is normalized by the mean initial cell density, B_0. The direction of the gradient is towards the right.
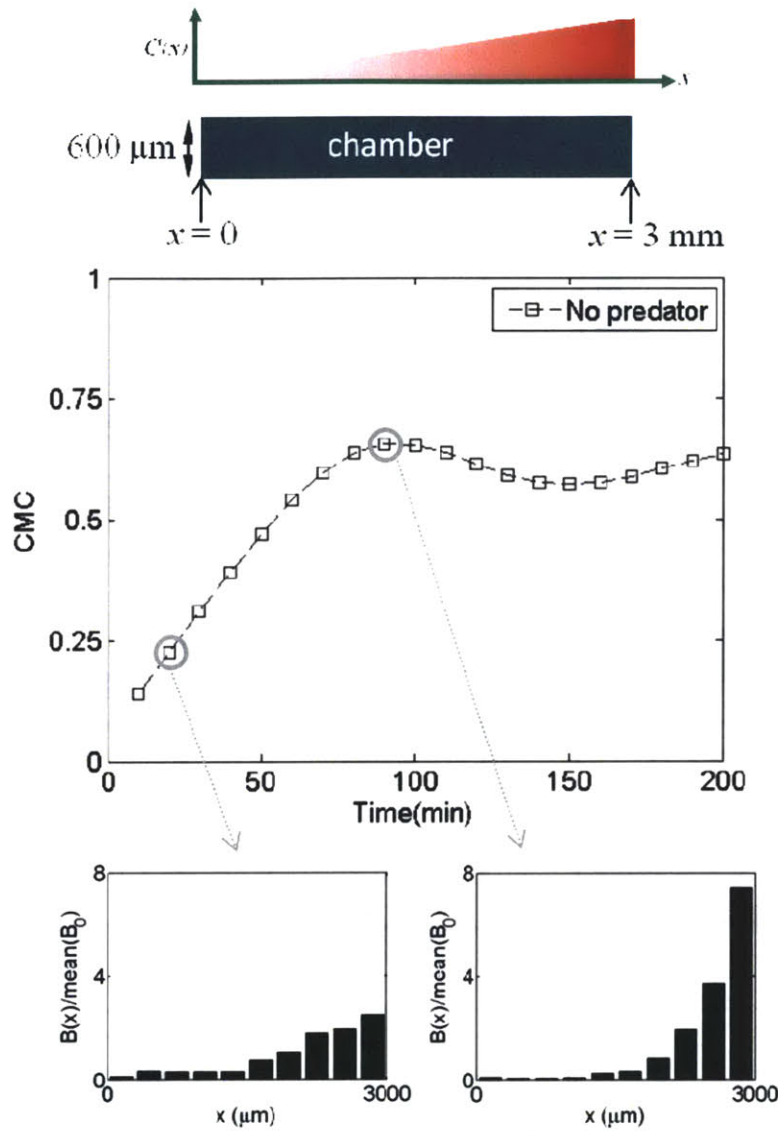
Figure 5.7 Time series of the Chemotactic Migration Coefficient (CMC) for the case of no predation.
CMC values indicate markedly higher chemotactic aggregation compared to both predation pressure regimes [Fig. 5.5]. This is also evident in the bacterial distribution, $B(x)$, shown at $t = 20$ and 90 min. The bacterial distribution is normalized by the mean initial cell density, B_0. The direction of the gradient is towards the right.

5.4.2 Effect of predation in a spatially structured, heterogeneous resource landscape

A mixed culture of T. *pyriformis* and E. *coli* was injected in the channels shown in Fig. 5.4, after a solute gradient in the agarose was established (see below for information on the solute). The series of channels consisted of seven 600 μm × 450 μm rectangular patches, connected by 100 μm long corridors of variable width, s. The entire habitat spanned a length of 3.75 mm. Instead

119
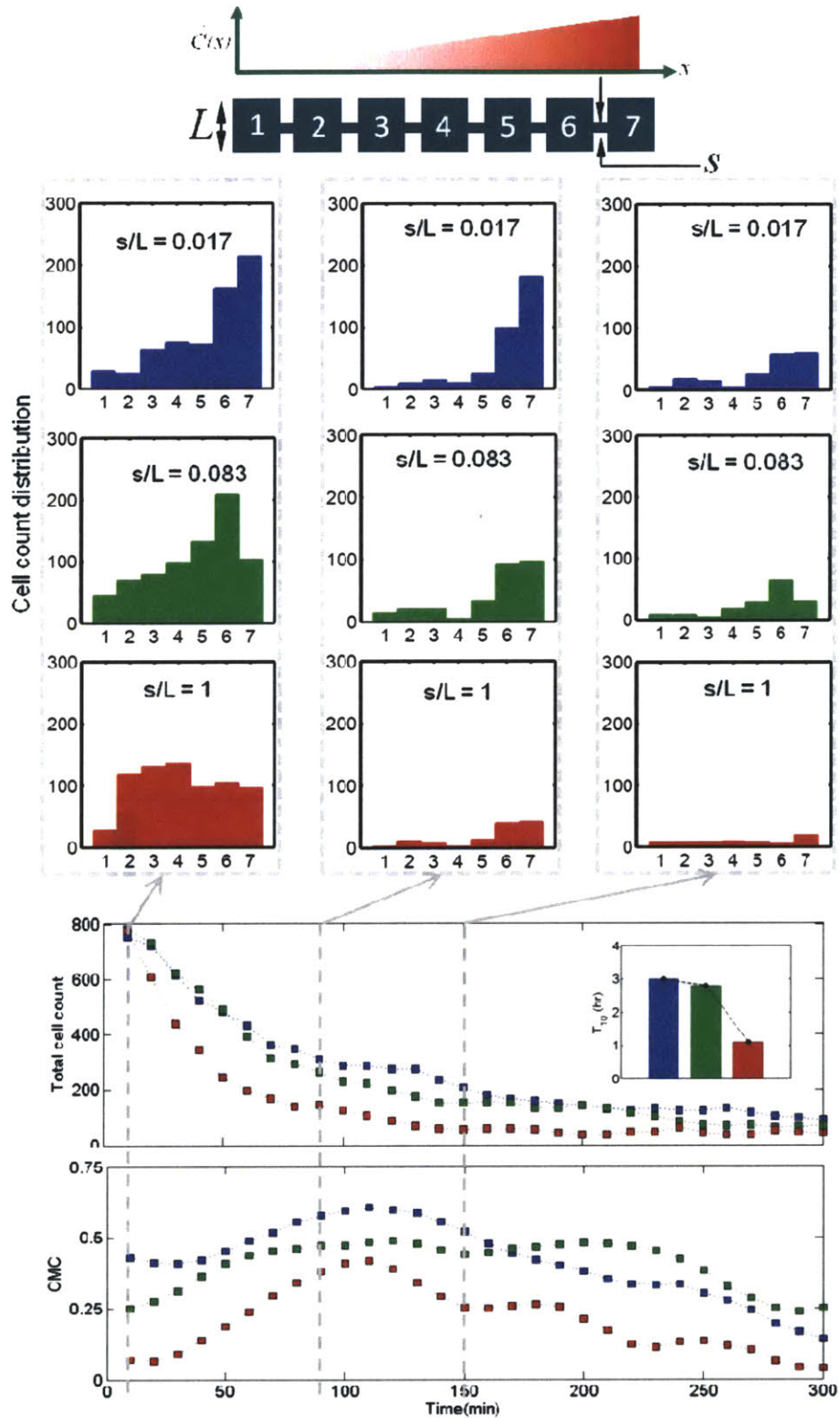
Figure 5.8 Time series of the total bacterial cell count and distribution asymmetry (CMC) for the three different cases of spatial heterogeneity. The habitats having restrictions ($s/L = 0.017$ and 0.083) show higher persistence times and greater degree of distribution asymmetry. This is also evident in the bacterial distribution at t = 10, 90 and 150 minutes. The direction of the gradient is towards the right.

of bacterial growth media, used in the unstructured environments described in section 5.4.1, here 1 mM alphamethylaspartate was used in the source channel, to establish a MeAsp gradient and drive chemotactic aggregation of bacteria in the direction of the source channel, thereby creating a heterogeneous resource landscape for the predator. Since MeAsp is a non-metabolizable analogue of aspartate, it will not support bacterial growth. The basic aim was to observe the effect of spatial restrictions in the habitat on the predation rate without the confounding effect of bacterial growth. It was separately confirmed that MeAsp does not elicit a chemotactic response by *T. pyriformis*.

Fig. 5.8 shows the bacterial population dynamics and distribution asymmetry for the experiments performed with three different spatial restrictions, $s = 10$, 50 and 600 μm (where the $s = 600$ μm represents an unrestricted environment). The initial bacterial concentration and number of predators were nearly the same in each case, giving a prey-to-predator ratio of $B_0/T_0 = 40$. Due to the high predation pressure, the bacterial populations in all three cases tended towards extinction within hours. However, there was a significant difference in the rate of decline, depending on the degree of the geometric constriction. The time taken for the bacterial population to reach 10% of their initial density, $T_{10\%}$, was used as a metric to compare the relative persistence times for the three cases. It was observed that the unrestricted case ($s/L = 1$) had the lowest persistence time ($T_{10\%} = 1$ hr), while the restricted habitats showed three times higher persistence times ($T_{10\%} = 3$ hr for $s/L = 0.017$ and $T_{10\%} = 2.8$ hr for $s/L = 0.083$). It remains unclear why the two restricted geometries did not exhibit any marked difference.

Chemotactic aggregation in a linear MeAsp gradient generates a skewed bacterial distribution along the habitats. As time progresses and cell numbers decrease due to predation, the distribution asymmetry became more pronounced, with the CMC reaching a maximum at $t = 90$ min for all three cases [Fig. 5.8]. From $t = 90$ min until the end of the experiment, the cell distribution gradually became more uniform.

Two further observations were made. First, the CMC value for the unrestricted habitat ($s/L = 1$) was in general lower than those for the restricted habitats. Second, the population distribution for the unrestricted case ($s/L = 1$) became uniform relatively quickly compared to the other two

cases. Both observations are likely due to the fact that the predators could more freely roam across the entire habitat in the unrestricted environment.
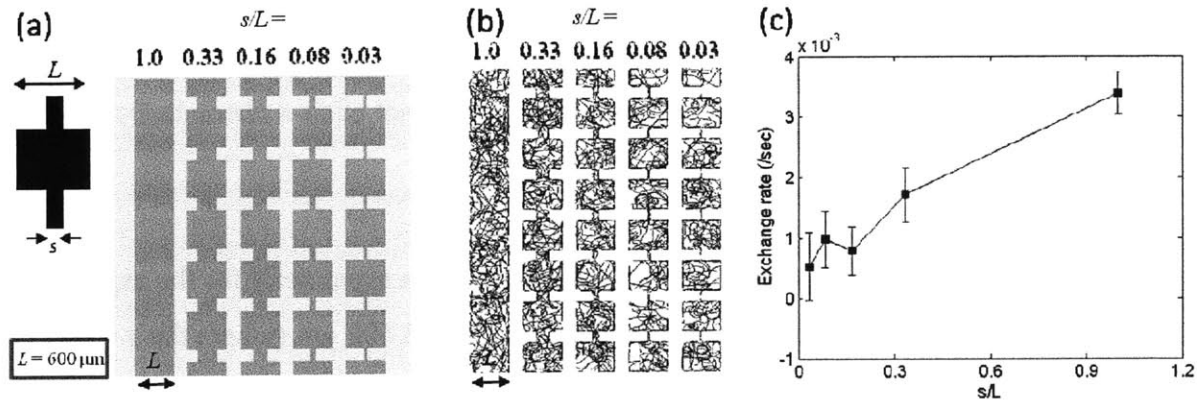
Figure 5.9 One-dimensional habitat arrays for different connectivities, s/L to measure predator dispersal. (a) Schematic of five arrays with s/L ranging from 0.03 to 1. (b) Experimental realization of the five arrays, showing trajectories of *T. pyriformis* obtained using tracking software (Bactrack). (c) Exchange rate of *T. pyriformis* (mean fraction of cells moving to a neighboring habitat per unit time) as a function of s/L. As expected, the exchange rate and hence the dispersal increase as habitats become more connected.

This is supported by a quantification of the dispersal characteristics of *T. pyriformis* in these spatially structured habitats. In a separate experiment, *T. pyriformis* cells were injected in a series of parallel habitats of different degrees of spatial restrictions, with s/L varying from 0.03 to 1 [Fig. 5.9]. The trajectories of *T. pyriformis* were analyzed and the average exchange rate (defined by the flux of cells across the corridors) was quantified for corridors of different width, s. It was observed that there is a marked increase in the exchange rate with the increase in the width of corridors, with an approximately 7-fold increase in exchange rate from $s/L = 0.03$ to $s/L = 1$ [Fig. 5.9]. In a spatially structured habitat with corridor restrictions, the dispersal rate of predators becomes limited and this affects the predation rate. Compared to an unrestricted habitat case ($s/L = 1$), the predator has to travel a more tortuous path to explore different patches in search of prey. In the limit of very strong constriction, predation may become limited to a few patches only, as some of the predators may get trapped and unable to disperse. This may be the cause of the delay in predation in the restricted habitats. The increased skewness in bacterial distribution in the spatially restricted patches cannot be fully explained but may be an indirect effect of the delay in

predation in those patches where a time lag can allow more time for chemotaxis. Some fraction of the prey population that escapes predation from predators along different patches gets more time to accumulate in the patches closer to the source channel which might increase the skewness of the bacterial distribution (hence higher CMC values). However, as time progresses, predators will eventually reach these dense patches and cause the overall population to go extinct.

5.5 Discussion

By generating a heterogeneous resource landscape for predators using microfluidics, it was shown that the demographic dynamics of the prey population was governed by the initial prey to predator ratio. A higher predation pressure will inevitably drive the prey population towards extinction, while at some intermediate regime of predation pressure, the prey populations will be allowed to grow and also maintain some degree of chemotactic spatial organization. The ultimate spatial demographic pattern will be dictated by a balance between predation, chemotaxis and growth.

By generating a heterogeneous resource landscape in spatially heterogeneous habitats, it was shown that the fate of the prey population can be further governed by the spatial heterogeneity, which in turn affects the dispersal capabilities of the predator. These experiments are an indication that the persistence time of the prey population can be influenced by spatial heterogeneity in the habitat structure. This approach could provide an ideal platform for metapopulation studies. Metapopulations emerge when different habitats are weakly linked by dispersal [160] and introduction of spatial restrictions is one way of implementing a weak dispersal.

One of the advantages of the microfluidic lattice microcosm is the possibility of directly visualizing not only the prey population dynamics, but also the predator movement and dispersal, which enabled us to link the spatial dynamics of the prey with the movement behavior of the predator. Here this was done to a limited degree, to provide a proof-of-concept demonstration, but microfluidics allows one to do this in considerable depth.

123

These measurements were non-invasive, did not require counting, and can be performed at high spatial and temporal resolution with little or no additional investment in time on the part of the experimenter. In addition, replication was effortless, in contrast to most existing studies which forgo it in view of the large effort involved in each experiment [219]. On the other hand, the results presented in this chapter are not conclusive, and significant work is yet to be done in the field of microbial predator-prey interactions under the metapopulation framework. Nevertheless, the development and assessment of this microfluidic lattice microcosm represent a first step in the direction of a predator-prey microcosm and illustrate the great potential of this approach, which enables the simultaneous quantification of population dynamics, movement behavior, and organism physiology.

This system provides an unprecedented flexibility in experimental design. The landscape topology (number, size and arrangement of the habitats and corridors) can be easily manipulated; the habitats can also be designed to provide spatial refuges for prey and patches with variable resource quality. This versatile, quantitative approach at the interface between population dynamics and behavioral ecology could contribute to bridge the gap between mathematical modeling and field studies, as it merges the ability to manipulate experimental conditions over a wide range of parameter space with the use of real organisms and the opportunity to directly quantify their behavior. At the same time, it will contribute to move towards a behavioral ecology of ecological landscapes [220]. While the spatial scale of ecological landscapes versus local movement ultimately depends on the species under consideration [220], it is possible that a microcosm – where the two scales can be comparable – provides an ideal starting point to address the fundamental role of movement in predator-prey dynamics.

Chapter 6

Summary and Future Work

In this thesis, I investigated different aspects of bacterial chemotaxis using microfluidic technology. In so doing, I demonstrated that microfluidics can be a powerful tool to study a diverse range of processes in microbial ecology, from the microscale quantification of chemotaxis and chemotactic migration parameters, to the study of sensing properties (FCD), to the investigation of trophic interactions.

In Chapter 2, by measuring swimming speed and bias in swimming direction of single cells for a range of chemoattractant concentrations and concentration gradients, the chemotactic sensitivity coefficient, χ_0, was directly computed using microfluidics and videomicroscopy. It was also shown how the random motility coefficient, μ can be readily determined using microfluidics, but that a population-scale microfluidic approach was experimentally more convenient than a single-cell analysis in that case. Measured values of both χ_0 [$(12.4\pm2.0)\times10^{-4}$ cm^2 s^{-1}] and μ [$(3.3\pm0.8)\times10^{-6}$ cm^2 s^{-1}] were found to be comparable to literature results. This microscale approach to bacterial chemotaxis lends experimental support to theoretical derivations of population-scale transport parameters from single-cell behavior. Furthermore, this study showed that microfluidic platforms can go beyond traditional chemotaxis assays and enable the quantification of bacterial transport parameters. One important aspect of this study was the ability to measure the chemotactic velocity of bacteria in a quiescent environment, under a wide range of gradient conditions (gradient magnitude and absolute concentration). These measurements showed that the chemotactic velocity of E. coli can reach up to 35% of its swimming speed, when E. coli is exposed to a suitable concentration field, markedly higher than the 5-15% traditionally observed [48]. Recent studies found marine bacteria to exhibit similarly high chemotactic velocities (40% for Pseudoalteromonas haloplanktis [137] and 35% for Vibrio alginolyticus [47]). Mathematical modeling has shown that the persistence parameter, α, which measures the mean of the cosine of angles between two successive runs of a bacteria, can be an important determinant in its chemotactic performance [221] where in general, the chemotactic velocity increases as α increases. Recently discovered hybrid locomotion in Vibrio aloginolyticus consisting of runs, flicks and reversals suggests that the mean persistence α ~ -0.5 for some of these marine bacterial species, significantly higher than what would have been based on a swimming strategy based on pure run and reversals [47, 48]. E. coli's tumbles are biased forward, with a mean angle of 68° and α = 0.33 [23] and according to Locsei [221], its

chemotactic velocity can only be higher than that of these marine bacteria if not comparable. Therefore, an observed chemotactic velocity of 35% for *E. coli* (with a theoretically maximum value of 67% according to Rivero *et al.*'s model [83]) agrees with Locsei's mathematical analysis. Previous chemotaxis studies presumably may not have been done in the optimum regime of the gradient spectrum where the chemotactic velocity is maximal. The versatility of this microfluidic device to explore a wide variety of spatial gradients can be used to significantly expand the limits of the observable range of chemotactic velocities, which was not possible in traditional chemotaxis assays. This promises to help expand the breadth of our knowledge of bacterial biophysics.

In chapter 3, three diffusion-based gradient generators were characterized and compared by confocal microscopy and numerical simulation, from which an optimal design was selected and applied to chemotaxis experiments with *Escherichia coli* in both linear and nonlinear gradients. Comparison of the observed cell distribution along the gradients with predictions from an established mathematical model showed very good agreement, providing the first quantification of chemotaxis of free-swimming cells in steady nonlinear microfluidic gradients and opening the door to bacterial chemotaxis studies in gradients of arbitrary shape. Diffusion-based steady gradient generators that use hydrogels to mediate chemoeffector diffusion while preventing flow represent the most promising and versatile approach to study bacterial chemotaxis. The steadiness of the gradient is a very favorable feature, enabling chemotaxis studies over long timescales and observation of steady-state behavior and cell distributions. Although a rather long time (minutes to hours, depending on the dimensions of the device and the diffusivity of the chemoeffector) is required to establish the gradient in the hydrogel, chemotaxis experiments can be conveniently performed after gradient setup [71]. In this respect, gradient generation becomes another step of the fabrication and setup process, rather than an integral part of the experiment itself. This feature can be useful to probe the behavior of microorganisms whose response timescale are not known a priori, including natural bacterial communities. Many species of bacteria residing in the marine or aquatic environment are slow to respond or may undergo a period of dormancy before their chemotactic behavior is triggered. These devices, which can conveniently decouple the gradient generation timescale from the timescale of the biological response, can be used to investigate their chemotactic responses. In recent years, a number of

microfluidic studies on the motility and chemotaxis of bacterial species other than *E. coli* have appeared [13, 14, 133, 136, 137, 148]. Yet much of the diversity in the swimming strategies and response timescales among bacteria remains only roughly characterized. Quantitative studies of such less well-characterized species enabled by these devices can considerably enrich the portfolio of model organisms for studies of bacterial chemotactic motility.

The quantitative control over spatial chemoeffector gradients made possible by microfluidic devices holds great promise for probing a vast range of fundamental questions regarding the design of cellular signaling circuits and the molecular underpinnings of bacterial chemotaxis. Kalinin *et al.* [68] applied the steady linear gradient generation principle to create two opposing chemoeffector gradients and showed that the chemotactic preference of bacteria towards one or the other depended on the ratio of the respective active chemoreceptors during particular stages of their growth. The same group also experimentally demonstrated logarithmic tracking in *E. coli* [67], the phenomenon where the bacterium senses and responds to the relative gradient of the ligand concentration, instead the gradient itself. Open questions still remain as to how this logarithmic tracking would affect the spatial organization of bacteria. A recent mathematical model by Jiang *et al.* [38] found that in a linear gradient, *E. coli* cells would swim towards higher attractant with a continuously decreasing chemotactic velocity, while in an exponential gradient, the chemotactic velocity would remain constant. The novel technique to generate stationary linear and nonlinear gradients described in Chapter 3, along with measurements of chemotactic velocity (Chapter 2), can be used to directly test the predictions of Jiang *et al.* [38] and contribute to the understanding of spatial organization of bacteria demonstrating logarithmic sensing behavior.

Chapter 4 described experiments to demonstrate fold-change detection in bacterial chemotaxis, a remarkable behavioral property analogous to Weber's law, but more general and exhibited by a number of adaptive sensory systems. Using microfluidic devices to generate a variety of scaled steady and unsteady gradients, it was shown that the transient population-scale response of *E. coli* remains invariant over a ~87 fold change in ambient chemoattractant concentration, which confirmed the observations of previous FRET measurements. Since the chemotaxis signaling pathway is a highly conserved feature in prokaryotes, it is possible that other bacterial species

exhibit this response rescaling property. In this respect, an ecologically relevant species can be the marine bacterium *Pseudoalteromonas haloplanktis*, which chemotaxes towards dissolved organic compounds, potentially affecting carbon transfer rates in the ocean. However, studying their signaling network using FRET measurements will require genetic manipulations which may not be readily possibly, because of the lack of knowledge of the molecular architecture of bacterial species other than *E. coli*. The microfluidic approach described in this chapter will allow one to bypass the need for molecular manipulations and directly quantify the response properties of other prokaryotes by directly observing their swimming behavior. It will further be interesting to investigate what features of the two-component signal transduction system of the bacterial chemotaxis pathway enable a bacterium to exhibit the property of fold change detection and what ecological advantages this property confers. Recently, an agent-based model built within the framework of the two-component signaling system has been extensively used to study bacterial chemotaxis in spatial domains [38, 67]. The synergy of such modeling approaches with experiments of the kind described here can be a powerful tool to further explore sensing and chemotaxis.

Finally, in Chapter 5, the fate of bacterial population undergoing chemotactic aggregation was studied under the effect of predation pressure by a protist, by designing and applying a microfluidic lattice microcosm. It was observed that the grazing by the protist significantly alters the demographic landscape of bacteria and that the population dynamics depended on bacterial growth, bacteria to protist ratio, and the spatial configuration of the habitat. These experiments pave the way to future studies in predator-prey dynamics in a metapopulation context. For example, habitat structure can be designed so that weak dispersal exists among habitat patches and one could then directly observe in real-time how metapopulations evolve. Microfluidics has already been used to study metapopulations of single bacterial species [200] and competing bacterial species [201]: applying similar tools to address questions in predator-prey metapopulations appears to be the next logical step. For example, one of the most interesting concepts in landscape ecology is the presence of 'spatial refugia' for prey, spatial domains not accessible to the predators due to their limited connectivity with the rest of the habitat, which can act as consistent sources of emigrants and thus increase regional persistence [156]. It would be interesting to determine how the population dynamics in a microbial microcosm depend on the

presence of spatial refugia, which can be easily constructed using microfluidic devices. These ideas can have practical implications in mimicking the fate of bacterial demographics in realistic natural microenvironments, where such restrictive structures exist (e.g. flow in subsurface porous media). The flexibility of the microfabrication process offers immense possibilities for recreating salient features of natural bacterial environments.

In the field of bacterial chemotaxis, like in many other research areas, the use of microfluidics is becoming commonplace not only in engineering and physics laboratories, but also in the hands of biologists and ecologists. The microfluidic toolbox for bacterial chemotaxis studies will continue to grow, as novel approaches for gradient generation emerge. While technological innovations are increasingly being driven by the scientific questions at hand, a fundamental understanding of the technology is also required so that the best approach can be selected once a scientific question has been defined. The motivation is to strive for a deeper and more widespread integration of technology and biology, so that each innovation can go beyond being merely an engineering marvel to become an enabling technology of new scientific discovery. This thesis is hopefully a step in that direction.

Appendix A

Theoretical framework for determining chemotactic velocity

Derivation of the expression for chemotactic velocity V_C is provided, focusing on the 1D case for simplicity. The extension to bacteria swimming in 3D is given in Chen *et al.* [96] and results in Eq. 9. Rivero *et al.* [83] derived an expression for V_C in terms of cell speed and tumbling probability:

$$V_C = v_{1D} \frac{p^- - p^+}{p^+ + p^-} .$$

(A1)

Brown and Berg [142] observed an exponential increase in run times (T) with the time rate of change in the number of bound receptors (N), relative to run times measured in the absence of chemical gradients (T_0). This led them to propose the empirical relation

$$T = T_0 \exp\left(\sigma \frac{dN}{dt} \right),$$

(A2)

where σ is a proportionality constant describing the fractional change in mean run time per unit rate of change in bound receptors. For a single homogeneous cell receptor population, at receptor/ligand binding equilibrium N is given by

$$N = N_T \frac{C}{K_D + C},$$

(A3)

where N_T is the total number of receptors for that ligand. Since the mean run time is the reciprocal of the tumbling probability, Eq. A2 can also be written in terms of the tumbling probability:

$$p^{+/-} = p_0 \exp\left(-\sigma \frac{DN^{+/-}}{Dt} \right).$$

(A4)

Here the cases of cells swimming up ($p^+=1/T^+$) and down ($p^-=1/T^-$) the gradient were separated, and p_0 ($=1/T_0$) is the tumbling probability in the absence of chemical gradients. The material derivative D/Dt is necessary to account for both temporal and spatial changes in attractant concentrations experienced by cells swimming at speed v_{1D}, and is defined as

$$\frac{DN^{+/-}}{Dt} = \left[\frac{\partial}{\partial t} \pm v_{1D}\frac{\partial}{\partial x} \right]N .$$ (A5)

Substituting Eqs. A4 and A5 into Eq. A1 yields, after some algebra,

$$V_C = v_{1D}\tanh\left(\sigma v_{1D}\frac{dN}{dC}\frac{dC}{dx} \right).$$ (A6)

From Eq. A3 it can be further obtained

$$\frac{dN}{dC} = N_T\frac{K_D}{\left(K_D+C\right)^2} = \frac{\chi_0}{v_{1D}^2\sigma}\frac{K_D}{\left(K_D+C\right)^2},$$ (A7)

where $\chi_0 = N_T v_{1D}^2\sigma$ represents a fractional change in dispersal capability per unit fractional change in receptor occupancy [61]. Substituting Eq. A7 in Eq. A6 gives

$$V_C = v_{1D}\tanh\left(\frac{\chi_0}{v_{1D}}\frac{K_D}{\left(K_D+C\right)^2}\frac{dC}{dx} \right).$$ (A8)

This relation expresses the dependence of the chemotactic velocity on the time rate of change of bound receptors. The case of bacteria swimming in 3D is treated in Chen *et al.* [96] and results in Eq. 2.9, which expresses the same relation, only with different numerical prefactors to account for the dimensionality of the problem.

Appendix B

Theoretical basis for Fold Change Detection

In contrast to the more mechanistically detailed approach in previous work [30, 222, 223], Tu *et al.* [33] developed a mean-field approach in which the *E. coli* chemosensory system and its environment can be described by three dynamic variables: (1) the ligand concentration [L](t) (the input); (2) the average methylation level of the receptors $m(t)$ (the feedback signal); and (3) the average kinase activity a(t) (the output). At this coarse-grained level, receptor responses are represented as an equilibrium process, as their state transitions occur on time scales much faster than the downstream adaptation reactions. The dynamics of the pathway can be captured by just two equations,

$$\frac{dm}{dt} = F(a) \tag{B1}$$

which describes the rate of change of the average receptor methylation level, m, as a function of the activity of the receptor-kinase complex, a, and

$$a = G([L], m) \tag{B2}$$

which determines the receptor-kinase activity at every moment in time, given the current level of ligand input, [L], and methylation feedback, m. The functions $F(a)$ and $G([L], m)$ can be viewed as transfer functions within this feedback circuit [Fig. A1], and their specific forms depend upon the underlying molecular mechanisms. Whereas $F(a)$ expresses the relatively slow changes in the receptor methylation level, $G([L], m)$ expresses the much faster response of the receptor-kinase complex. Because of this separation of timescales, the feedback signal, m, serves as a memory for the system, which is compared at every moment in time with the current input, [L].

Within the MWC framework [224], the entire receptor-kinase, complex comprising N clustered receptor units, is treated as a system with two microscopic states that differ in kinase activity and ligand affinity: an "active" conformation, with low ligand affinity and high kinase activity, and an "inactive" conformation with high ligand affinity and zero kinase activity. The kinase activity,

$a = G([L],m)$, then corresponds to the probability of finding the receptor-kinase complex in the active state,

$$G([L],m) = G(f_t([L],m)) = (1 + e^{f_t([L],m)})^{-1},$$

where $f_t([L],m) = N(f_L([L]) + f_m(m))$ is the total free-energy difference (in $k_B T$ units) between the active and inactive states, consisting of a ligand-dependent part, $f_L([L])$, and a methylation-dependent part, $f_m(m)$, the sum of which is scaled by the size of the cooperatively coupled receptor cluster, N.
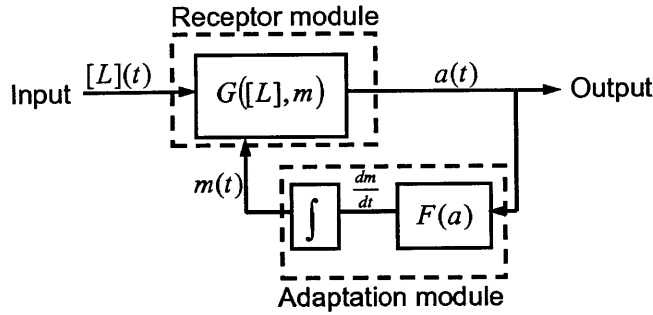
Figure B1. Modular view of the bacterial chemotaxis network proposed by Tu *et al.* The input–output relation of the receptor module is described by the function G, which takes [L] and m as inputs to produce an output a, which connects to the downstream linear pathway toward motor output. The adaptation module constitutes the feedback loop of the network, in which the output a is converted through $F(a)$ to dm/dt and integrated over time.

Within the MWC model, the ligand effect on free energy is due to the two microscopic states of the receptor-kinase complex having distinct affinities for ligand, and is described by the expression $f_L([L]) = \ln(1 + [L]/K_I) - \ln(1 + [L]/K_A)$, where K_I and K_A are the dissociation constants for the inactive and active receptor states having values of 18 μM and 2.9 mM for Tar receptor (in response to MeAsp), respectively. For ligand concentrations in the range $K_I \ll [L] \ll K_A$,

$$f_L([L]) \approx \ln([L]/K_I)$$

The term $f_m(m)$, which determines the kinase activity in the absence of ligand, depends linearly on methylation, $f_m(m) = \alpha(m_0 - m)$ with $\alpha \approx 2$ and $m_0 \approx 0.5$ [32]. Rewriting Eq. B2,

134

$$a = (1 + ([L]/K_I)^N e^{Nf_m})^{-1}$$

<div align="right">(B3)</div>

Assuming an internal variable, $x = K_I exp(-f_m)$, Eq. B3 can be written as

$$a = (1 + ([L]/x)^N)^{-1}$$

<div align="right">(B4)</div>

Taking the temporal derivative of x and using Eq. B1 yields

$$dx/dt = \alpha x F(y)$$

<div align="right">(B5)</div>

Replacing the variables $[L]$ and a with u and y respectively in Eq. B4 and B5

$$y = (1 + (u/x)^N)^{-1}$$
$$dx/dt = \alpha x F(a)$$

<div align="right">(B6)</div>

Eq. B6 satisfies Eq. 4.1, the necessary conditions for Fold Change Detection (FCD).

BIBLIOGRAPHY

[1] T. Ahmed, T.S. Shimizu, R. Stocker, Microfluidics for bacterial chemotaxis, Integrative Biology, 2 (2010) 604-629.

[2] G. Drews, Contributions of Theodor Wilhelm Engelmann on phototaxis, chemotaxis, and photosynthesis, Photosynthesis Research, 83 (2005) 25-34.

[3] M.S. Pittman, M. Goodwin, D.J. Kelly, Chemotaxis in the human gastric pathogen *Helicobacter pylori*: different roles for CheW and the three CheV paralogues, and evidence for CheV2 phosphorylation, Microbiology, 147 (2001) 2493-2504.

[4] M.B. Hugdahl, J.T. Beery, M.P. Doyle, Chemotactic behavior of *Campylobacter jejuni*, Infection and Immunity, 56 (1988) 1560-1566.

[5] R. Freter, P.C.M. Obrien, Role of chemotaxis in the association of motile bacteria with intestinal mucosa - chemotactic responses of *Vibrio cholerae* and description of motile non-chemotactic mutants, Infection and Immunity, 34 (1981) 215-221.

[6] D.L. Englert, M.D. Manson, A. Jayaraman, Flow-based microfluidic device for quantifying bacterial chemotaxis in stable, competing gradients, Applied and Environmental Microbiology, 75 (2009) 4557-4564.

[7] R. O'Toole, S. Lundberg, S.A. Fredriksson, A. Jansson, B. Nilsson, H. Wolf-Watz, The chemotactic response of *Vibrio anguillarum* to fish intestinal mucus is mediated by a combination of multiple mucus components, Journal of Bacteriology, 181 (1999) 4308-4317.

[8] A.M. Ashby, M.D. Watson, C.H. Shaw, A Ti-plasmid determined function is responsible for chemotaxis of *Agrobacterium tumefaciens* towards the plant wound product acetosyringone, Fems Microbiology Letters, 41 (1987) 189-192.

[9] S. Pandya, P. Iyer, V. Gaitonde, T. Parekh, A. Desai, Chemotaxis of rhizobium SP.S2 towards Cajanus cajan root exudate and its major components, Current Microbiology, 38 (1999) 205-209.

[10] G. Pandey, R.K. Jain, Bacterial chemotaxis toward environmental pollutants: Role in bioremediation, Applied and Environmental Microbiology, 68 (2002) 5789-5795.

[11] F. Azam, T. Fenchel, J.G. Field, J.S. Gray, L.A. Meyerreil, F. Thingstad, The ecological role of water column microbes in the sea, Marine Ecology Progress Series, 10 (1983) 257-263.

[12] N. Blackburn, F. Azam, A. Hagstrom, Spatially explicit simulations of a microbial food web, Limnology and Oceanography, 42 (1997) 613-622.

[13] J.R. Seymour, R. Simo, T. Ahmed, R. Stocker, Chemoattraction to Dimethylsulfoniopropionate Throughout the Marine Microbial Food Web, Science, 329 (2010) 342-345.

[14] R. Stocker, J.R. Seymour, A. Samadani, D.E. Hunt, M.F. Polz, Rapid chemotactic response enables marine bacteria to exploit ephemeral microscale nutrient patches, Proceedings of the National Academy of Sciences of the United States of America, 105 (2008) 4209-4214.

[15] F. Azam, Microbial control of oceanic carbon flux: The plot thickens, Science, 280 (1998) 694-696.

[16] T. Fenchel, N. Blackburn, Motile chemosensory behavior of phagotrophic protists: Mechanisms for and efficiency in congregating at food patches, Protist, 150 (1999) 325-336.

[17] F. Azam, R.A. Long, Oceanography - Sea snow microcosms, Nature, 414 (2001) 495-498.

[18] W.K. Pilgram, F.D. Williams, Survival value of chemotaxis in mixed cultures, Canadian Journal of Microbiology, 22 (1976) 1771-1773.

[19] F.X. Kelly, K.J. Dapsis, D.A. Lauffenburger, Effect of bacterial chemotaxis on dynamics of microbial competition, Microbial Ecology, 16 (1988) 115-131.

[20] H.C. Berg, D.A. Brown, Chemotaxis in *Escherichia coli* analysed by three-dimensional tracking, Nature, 239 (1972) 500-504.

[21] H. Szurmant, G.W. Ordal, Diversity in chemotaxis mechanisms among the bacteria and archaea, Microbiology and Molecular Biology Reviews, 68 (2004) 301-319.

[22] G.H. Wadhams, J.P. Armitage, Making sense of it all: Bacterial chemotaxis, Nature Reviews Molecular Cell Biology, 5 (2004) 1024-1037.

[23] H.C. Berg, *E. coli* in motion, Springer-Verlag, 2003.

[24] J.E. Segall, M.D. Manson, H.C. Berg, Signal processing times in bacterial chemotaxis, Nature, 296 (1982) 855-857.

[25] V. Sourjik, H.C. Berg, Binding of the *Escherichia coli* response regulator CheY to its target measured in vivo by fluorescence resonance energy transfer, Proceedings of the National Academy of Sciences of the United States of America, 99 (2002) 12669-12674.

[26] J.E. Segall, S.M. Block, H.C. Berg, Temporal comparisons in bacterial chemotaxis, Proceedings of the National Academy of Sciences of the United States of America, 83 (1986) 8987-8991.

[27] V. Sourjik, J.P. Armitage, Spatial organization in bacterial chemotaxis, EMBO Journal, 29 (2010) 2724-2733.

[28] U. Alon, M.G. Surette, N. Barkai, S. Leibler, Robustness in bacterial chemotaxis, Nature, 397 (1999) 168-171.

[29] N. Barkai, S. Leibler, Robustness in simple biochemical networks, Nature, 387 (1997) 913-917.

[30] D. Bray, M.D. Levin, C.J. Morton-Firth, Receptor clustering as a cellular mechanism to control sensitivity, Nature, 393 (1998) 85-88.

[31] V. Sourjik, H.C. Berg, Receptor sensitivity in bacterial chemotaxis, Proceedings of the National Academy of Sciences of the United States of America, 99 (2002) 123-127.

[32] T.S. Shimizu, Y.H. Tu, H.C. Berg, A modular gradient-sensing network for chemotaxis in *Escherichia coli* revealed by responses to time-varying stimuli, Molecular Systems Biology, 6 (2010).

[33] Y.H. Tu, T.S. Shimizu, H.C. Berg, Modeling the chemotactic response of *Escherichia coli* to time-varying stimuli, Proceedings of the National Academy of Sciences of the United States of America, 105 (2008) 14855-14860.

[34] M.J. Schnitzer, Theory of continuum random walks and application to chemotaxis, Physical Review E, 48 (1993) 2553-2568.

[35] M.J. Schnitzer, S.M. Block, H.C. Berg, E.M. Purcell, Strategies for chemotaxis, Symp. Soc. Gen. Microbiol., 46 (1990) 15-33.

[36] D.A. Clark, L.C. Grant, The bacterial chemotactic response reflects a compromise between transient and steady-state behavior, Proceedings of the National Academy of Sciences of the United States of America, 102 (2005) 9150-9155.

[37] A. Celani, M. Vergassola, Bacterial strategies for chemotaxis response, Proceedings of the National Academy of Sciences of the United States of America, 107 (2010) 1391-1396.

[38] L. Jiang, Q. Ouyang, Y. Tu, Quantitative modeling of *Escherichia coli* chemotactic motion in environments varying in space and time, PLoS Computational Biology, 6 (2010) e1000735.

[39] D. Bray, M.D. Levin, K. Lipkow, The chemotactic behavior of computer-based surrogate bacteria, Current Biology, 17 (2007) 12-19.

[40] P.G. de Gennes, Chemotaxis: the role of internal delays, European Biophysics Journal with Biophysics Letters, 33 (2004) 691-693.

[41] N. Vladimirov, L. Lovdok, D. Lebiedz, V. Sourjik, Dependence of Bacterial Chemotaxis on Gradient Shape and Adaptation Rate, PloS Computational Biology, 4 (2008) e1000242.

[42] J. Shioi, S. Matsuura, Y. Imae, Quantitative measurements of proton motive force and motility in *Bacillus subtilis.*, Journal of Bacteriology, 144 (1980) 891-897.

[43] Y. Magariyama, S. Sugiyama, S. Kudo, Bacterial swimming speed and rotation rate of bundled flagella, FEMS Microbiology Letters, 199 (2001) 125-129.

[44] M.L. Worku, R.L. Sidebotham, J.H. Baron, J.J. Misiewicz, R.P.H. Logan, T. Keshavarz, Q.N. Karim, Motility of *Helicobacter pylori* in a viscous environment, European Journal of Gastroenterology & Hepatology, 11 (1999) 1143-1150.

[45] J.G. Mitchell, L. Pearson, S. Dillon, Clustering of marine bacteria in seawater enrichments, Applied and Environmental Microbiology, 62 (1996) 3716-3721.

[46] J.E. Johansen, J. Pinhassi, N. Blackburn, U.L. Zweifel, A. Hagstrom, Variability in motility characteristics among marine bacteria, Aquatic Microbial Ecology, 28 (2002) 229-237.

[47] T. Altindal, L. Xie, X.L. Wu, Implications of Three-Step Swimming Patterns in Bacterial Chemotaxis, Biophysical Journal, 100 (2011) 32-41.

[48] R. Stocker, Reverse and flick: Hybrid locomotion in bacteria, Proceedings of the National Academy of Sciences of the United States of America, 108 (2011) 2635-2636.

[49] J.G. Mitchell, L. Pearson, A. Bonazinga, S. Dillon, H. Khouri, R. Paxinos, Long lag times and high velocities in the motility of natural assemblages of marine bacteria, Applied and Environmental Microbiology, 61 (1995) 877-882.

[50] T. Fenchel, R. Thar, "Candidatus Ovobacter propellens": a large conspicuous prokaryote with an unusual motility behavior, FEMS Microbiology Ecology, 48 (2004) 231-238.

[51] T. Fenchel, Motility and chemosensory behavior of the sulfur bacterium *Thiovulum majus*, Microbiology, 140 (1994) 3109-3116.

[52] J.P. Armitage, R.M. Macnab, Unidirectional, intermittent rotation of the flagellum of *Rhodobacter sphaeroides*, Journal of Bacteriology, 169 (1987) 514-518.

[53] J. Adler, Chemoreceptors in bacteria., Science, 166 (1969) 1588-1597.

[54] R.M. Ford, B.R. Phillips, J.A. Quinn, D.A. Lauffenburger, Measurement of bacterial random motility and chemotaxis coefficients I: Stopped Flow Diffusion Chamber assay, Biotechnology and Bioengineering, 37 (1991) 647-660.

[55] A.M.J. Law, M.D. Aitken, Continuous-flow capillary assay for measuring bacterial chemotaxis, Applied and Environmental Microbiology, 71 (2005) 3137-3143.

[56] H.C. Berg, L. Turner, Chemotaxis of bacteria in glass-capillary arrays, Biophysical Journal, 58 (1990) 919-930.

[57] J. Adler, Chemotaxis in bacteria, Science, 153 (1966) 708-716.

[58] M. Silverman, M. Simon, Flagellar rotation and mechanism of bacterial motility, Nature, 249 (1974) 73-74.

[59] R.K. Jain, J. Pandey, Handbook of Hydrocarbon and Lipid Microbiology, 1st ed., Springer Berlin Heidelberg, 2010.

[60] D.L. Englert, A. Jayaraman, M.D. Manson, Microfluidic techniques for the analysis of bacterial chemotaxis, Methods Mol Biol, 571 (2009) 1-23.

[61] R.M. Ford, D.A. Lauffenburger, Measurement of bacterial random motility and chemotaxis coefficients II: Application of single-cell-based mathematical model, Biotechnology and Bioengineering, 37 (1991) 661-672.

[62] M.G. Vicker, Ideal and nonideal concentration gradient propagation in chemotaxis studies, Experimental Cell Research, 136 (1981) 91-100.

[63] S. Saleh-Lakha, J.T. Trevors, Perspective: Microfluidic applications in microbiology, Journal of Microbiological Methods, 82 (2010) 108-111.

[64] G.M. Whitesides, E. Ostuni, S. Takayama, X.Y. Jiang, D.E. Ingber, Soft lithography in biology and biochemistry, Annual Review of Biomedical Engineering, 3 (2001) 335-373.

[65] C.T. Culbertson, S.C. Jacobson, J.M. Ramsey, Diffusion coefficient measurements in microfluidic devices, Talanta, 56 (2002) 365-373.

[66] P. Lewus, R.M. Ford, Quantification of random motility and chemotaxis bacterial transport coefficients using individual-cell and population-scale assays, Biotechnology and Bioengineering, 75 (2001) 292-304.

[67] Y.V. Kalinin, L.L. Jiang, Y.H. Tu, M.M. Wu, Logarithmic Sensing in *Escherichia coli* Bacterial Chemotaxis, Biophysical Journal, 96 (2009) 2439-2448.

[68] Y. Kalinin, S. Neumann, V. Sourjik, M.M. Wu, Responses of *Escherichia coli* Bacteria to Two Opposing Chemoattractant Gradients Depend on the Chemoreceptor Ratio, Journal of Bacteriology, 192 (2010) 1796-1800.

[69] T. Long, R.M. Ford, Enhanced Transverse Migration of Bacteria by Chemotaxis in a Porous T-Sensor, Environmental Science & Technology, 43 (2009) 1546-1552.

[70] T. Ahmed, R. Stocker, Experimental verification of the behavioral foundation of bacterial transport parameters using microfluidics, Biophysical Journal, 95 (2008) 4481-4493.

[71] T. Ahmed, T.S. Shimizu, R. Stocker, Bacterial chemotaxis in linear and nonlinear steady microfluidic gradients, Nano Letters, 10 (2010) 3379-3385.

[72] O. Shoval, L. Goentoro, Y. Hart, A. Mayo, E. Sontag, U. Alon, Fold-change detection and scalar symmetry of sensory input fields, Proceedings of the National Academy of Sciences of the United States of America, 107 (2010) 15995-16000.

[73] J.R. Seymour, T. Ahmed, Marcos, R. Stocker, A microfluidic chemotaxis assay to study microbial behavior in diffusing nutrient patches, Limnology and Oceanography: Methods, 6 (2008) 477-488.

[74] F. Azam, R.A. Long, Sea snow microcosms, Nature, 414 (2001) 495-498.

[75] R.M. Macnab, D.E. Koshland, Gradient sensing mechanism in bacterial chemotaxis, Proceedings of the National Academy of Sciences of the United States of America, 69 (1972) 2509-2512.

[76] E.F. Keller, L.A. Segel, Model for chemotaxis, Journal of Theoretical Biology, 30 (1971) 225-234.

[77] J. Adler, Method for measuring chemotaxis and use of method to determine optimum conditions for chemotaxis by *Escherichia coli*, Journal of General Microbiology, 74 (1973) 77-91.

[78] R.B. Marx, M.D. Aitken, Quantification of chemotaxis to naphthalene by *Pseudomonas putida* G7, Applied and Environmental Microbiology, 65 (1999) 2847-2852.

[79] P. Lewus, R.M. Ford, Temperature-sensitive motility of *Sulfolobus acidocaldarius* influences population distribution in extreme environments, Journal of Bacteriology, 181 (1999) 4020-4025.

[80] M. Holz, S.H. Chen, Spatio-temporal structure of migrating chemotactic band of *Escherichia coli*. I. Traveling band profile, Biophysical Journal, 26 (1979) 243-261.

[81] L.Y. Zaval'skii, A.I. Marchenko, R.V. Borovik, The study of bacterial chemotaxis to naphthalene, Microbiology, 72 (2003) 363-368.

[82] B.E. Farrell, R.P. Daniele, D.A. Lauffenburger, Quantitative relationships between single-cell and cell-population model parameters for chemosensory migration responses of alveolar macrophages to C5a, Cell Motility and the Cytoskeleton, 16 (1990) 279-293.

[83] M.A. Rivero, R.T. Tranquillo, H.M. Buettner, D.A. Lauffenburger, Transport models for chemotactic cell-populations based on individual cell behavior, Chemical Engineering Science, 44 (1989) 2881-2897.

[84] H.G. Othmer, S.R. Dunbar, W. Alt, Models of dispersal in biological systems, Journal of Mathematical Biology, 26 (1988) 263-298.

[85] D.B. Weibel, W.R. DiLuzio, G.M. Whitesides, Microfabrication meets microbiology, Nature Reviews Microbiology, 5 (2007) 209-218.

[86] W. Saadi, S.J. Wang, F. Lin, N.L. Jeon, A parallel-gradient microfluidic chamber for quantitative analysis of breast cancer cell chemotaxis, Biomedical Microdevices, 8 (2006) 109-118.

[87] S. Koyama, D. Amarie, H.A. Soini, M.V. Novotny, S.C. Jacobson, Chemotaxis assays of mouse sperm on microfluidic devices, Analytical Chemistry, 78 (2006) 3354-3359.

[88] G.M. Walker, J.Q. Sai, A. Richmond, M. Stremler, C.Y. Chung, J.P. Wikswo, Effects of flow and diffusion on chemotaxis studies in a microfabricated gradient generator, Lab on a Chip, 5 (2005) 611-618.

[89] H.B. Mao, P.S. Cremer, M.D. Manson, A sensitive, versatile microfluidic assay for bacterial chemotaxis, Proceedings of the National Academy of Sciences of the United States of America, 100 (2003) 5449-5454.

[90] N.L. Jeon, H. Baskaran, S.K.W. Dertinger, G.M. Whitesides, L. Van de Water, M. Toner, Neutrophil chemotaxis in linear and complex gradients of interleukin-8 formed in a microfabricated device, Nature Biotechnology, 20 (2002) 826-830.

[91] B.G. Chung, F. Lin, N.L. Jeon, A microfluidic multi-injector for gradient generation, Lab on a Chip, 6 (2006) 764-768.

[92] D. Irimia, M. Toner, Cell handling using microstructured membranes, Lab on a Chip, 6 (2006) 345-352.

[93] S.Y. Cheng, S. Heilman, M. Wasserman, S. Archer, M.L. Shuler, M.M. Wu, A hydrogel-based microfluidic device for the studies of directed cell migration, Lab on a Chip, 7 (2007) 763-769.

[94] J.P. Diao, L. Young, S. Kim, E.A. Fogarty, S.M. Heilman, P. Zhou, M.L. Shuler, M.M. Wu, M.P. DeLisa, A three-channel microfluidic device for generating static linear gradients and its application to the quantitative analysis of bacterial chemotaxis, Lab on a Chip, 6 (2006) 381-388.

[95] L.M. Lanning, R.M. Ford, T. Long, Bacterial chemotaxis transverse to axial flow in a microfluidic channel, Biotechnology and Bioengineering, 100 (2008) 653-663.

[96] K.C. Chen, R.M. Ford, P.T. Cummings, Perturbation expansion of Alt's cell balance equations reduces to Segel's one-dimensional equations for shallow chemoattractant gradients, SIAM Journal on Applied Mathematics, 59 (1998) 35-57.

[97] R.M. Ford, P.T. Cummings, On the relationship between cell balance-equations for chemotactic cell-populations, SIAM Journal on Applied Mathematics, 52 (1992) 1426-1441.

[98] R. Mesibov, G.W. Ordal, J. Adler, Range of attractant concentrations for bacterial chemotaxis and threshold and size of response over this range - Weber law and related phenomena, Journal of General Physiology, 62 (1973) 203-223.

[99] H.C. Berg, P.M. Tedesco, Transient response to chemotactic stimuli in *Escherichia coli*, Proceedings of the National Academy of Sciences of the United States of America, 72 (1975) 3235-3239.

[100] S. Wright, B. Walia, J.S. Parkinson, S. Khan, Differential activation of *Escherichia coli* chemoreceptors by blue-light stimuli, Journal of Bacteriology, 188 (2006) 3962-3971.

[101] F.W. Dahlquist, R.A. Elwell, P.S. Lovely, Studies of bacterial chemotaxis in defined concentration gradients - model for chemotaxis toward L-serine, Journal of Supramolecular Structure, 4 (1976) 329-342.

[102] F. Dahlquist, P. Lovely, D. Koshland, Quantitative analysis of bacterial migration in chemotaxis, Nature: New Biology, 236 (1972) 120-123.

[103] I. Strauss, P.D. Frymier, C.M. Hahn, R.M. Ford, Analysis of bacterial migration: II. Studies with multiple attractant gradients, Aiche Journal, 41 (1995) 402-414.

[104] S.M. Block, J.E. Segall, H.C. Berg, Adaptation kinetics in bacterial chemotaxis, Journal of Bacteriology, 154 (1983) 312-323.

[105] S.M. Block, J.E. Segall, H.C. Berg, Impulse responses in bacterial chemotaxis, Cell, 31 (1982) 215-226.

[106] H.L. Packer, J.P. Armitage, The chemokinetic and chemotactic behavior of *Rhodobacter sphaeroides* - 2 independent responses, Journal of Bacteriology, 176 (1994) 206-212.

[107] I.B. Zhulin, J.P. Armitage, Motility, chemokinesis, and methylation-independent chemotaxis in *Azospirillum brasilense*, Journal of Bacteriology, 175 (1993) 952-958.

[108] M.M. Wu, J.W. Roberts, S. Kim, D.L. Koch, M.P. DeLisa, Collective bacterial dynamics revealed using a three-dimensional population-scale defocused particle tracking technique, Applied and Environmental Microbiology, 72 (2006) 4987-4994.

[109] J. Sheng, E. Malkiel, J. Katz, J. Adolf, R. Belas, A.R. Place, Digital holographic microscopy reveals prey-induced changes in swimming behavior of predatory dinoflagellates, Proceedings of the National Academy of Sciences of the United States of America, 104 (2007) 17512-17517.

[110] B. Zhao, J.S. Moore, D.J. Beebe, Surface-directed liquid flow inside microchannels, Science, 291 (2001) 1023-1026.

[111] J.P. Armitage, Behavioral responses of bacteria to light and oxygen, Archives of Microbiology, 168 (1997) 249-261.

[112] A.M. Wellman, H.W. Paerl, Rapid chemotaxis assay using radioactively labeled bacterial cells, Applied and Environmental Microbiology, 42 (1981) 216-221.

[113] R.B. Marx, M.D. Aitken, A material-balance approach for modeling bacterial chemotaxis to a consumable substrate in the capillary assay, Biotechnology and Bioengineering, 68 (2000) 308-315.

[114] L.M. Lanning, R.M. Ford, Glass micromodel study of bacterial dispersion in spatially periodic porous networks, Biotechnology and Bioengineering, 78 (2002) 556-566.

[115] Marcos, R. Stocker, Microorganisms in vortices: a microfluidic setup, Limnology and Oceanography-Methods, 4 (2006) 392-398.

[116] G.B. Jeffery, The motion of ellipsoidal particles immersed in a viscous fluid, Proceedings of the Royal Society of London, 120 (1922) 161-179.

[117] L. Wu, G.P. Li, W. Xu, M. Bachman, Droplet formation in microchannels under static conditions, Applied Physics Letters, 89 (2006) 3.

[118] Z.W. Liu, K.D. Papadopoulos, Unidirectional motility of *Escherichia coli* in restrictive capillaries, Applied and Environmental Microbiology, 61 (1995) 3567-3572.

[119] S.A. Biondi, J.A. Quinn, H. Goldfine, Random motility of swimming bacteria in restricted geometries, AIChE Journal, 44 (1998) 1923-1929.

[120] E. Lauga, W.R. DiLuzio, G.M. Whitesides, H.A. Stone, Swimming in circles: Motion of bacteria near solid boundaries, Biophysical Journal, 90 (2006) 400-412.

[121] W.R. DiLuzio, L. Turner, M. Mayer, P. Garstecki, D.B. Weibel, H.C. Berg, G.M. Whitesides, *Escherichia coli* swim on the right-hand side, Nature, 435 (2005) 1271-1274.

[122] P.D. Frymier, R.M. Ford, Analysis of bacterial swimming speed approaching a solid-liquid interface, AIChE Journal, 43 (1997) 1341-1347.

[123] P.D. Frymier, R.M. Ford, H.C. Berg, P.T. Cummings, 3-Dimensional tracking of motile bacteria near a solid planar surface, Proceedings of the National Academy of Sciences of the United States of America, 92 (1995) 6195-6199.

[124] J. Hill, O. Kalkanci, J.L. McMurry, H. Koser, Hydrodynamic surface interactions enable *Escherichia coli* to seek efficient routes to swim upstream, Physical Review Letters, 98 (2007) 4.

[125] M. Ramia, D.L. Tullock, N. Phanthien, The role of hydrodynamic interaction in the locomotion of microorganisms, Biophysical Journal, 65 (1993) 755-778.

[126] H.C. Berg, Random Walks in Biology, Princeton University Press, 1983.

[127] E. Korobkova, T. Emonet, J.M.G. Vilar, T.S. Shimizu, P. Cluzel, From molecular noise to behavioral variability in a single bacterium, Nature, 428 (2004) 574-578.

[128] J.H. Nilson, Editorial - A growing partnership between structural biology and molecular endocrinology, Molecular Endocrinology, 15 (2001) 351-352.

[129] G.M. Barbara, J.G. Mitchell, Bacterial tracking of motile algae, Fems Microbiology Ecology, 44 (2003) 79-87.

[130] J. Adler, Method for measuring chemotaxis and use of method to determine optimum conditions for chemotaxis by *Escherichia coli*, Journal of General Microbiology, 74 (1973) 77-91.

[131] J.T. Locsei, T.J. Pedley, Run and tumble chemotaxis in a shear flow: the effect of temporal comparisons, persistence, rotational diffusion, and cell shape, Bulletin of Mathematical Biology, 71 (2009) 1089-1116.

[132] H. Jeon, Y. Lee, S. Jin, S. Koo, C.S. Lee, J.Y. Yoo, Quantitative analysis of single bacterial chemotaxis using a linear concentration gradient microchannel, Biomedical Microdevices, 11 (2009) 1135-1143.

[133] J. Atencia, J. Morrow, L.E. Locascio, The microfluidic palette: A diffusive gradient generator with spatio-temporal control, Lab on a Chip, 9 (2009) 2707-2714.

[134] U. Haessler, Y. Kalinin, M.A. Swartz, M. Wu, An agarose-based microfluidic platform with a gradient buffer for 3D chemotaxis studies, Biomed Microdevices, 11 (2009) 827-835.

[135] H.K. Wu, B. Huang, R.N. Zare, Generation of complex, static solution gradients in microfluidic channels, Journal of the American Chemical Society, 128 (2006) 4194-4195.

[136] J.R. Seymour, T. Ahmed, R. Stocker, Bacterial chemotaxis towards the extracellular products of the toxic phytoplankton *Heterosigma akashiwo*, Journal of Plankton Research, 31 (2009) 1557-1561.

[137] J.R. Seymour, Marcos, R. Stocker, Resource Patch Formation and Exploitation throughout the Marine Microbial Food Web, American Naturalist, 173 (2009) E15-E29.

[138] N. Blackburn, T. Fenchel, J. Mitchell, Microscale nutrient patches in planktonic habitats shown by chemotactic bacteria, Science, 282 (1998) 2254-2256.

[139] V.V. Abhyankar, M.W. Toepke, C.L. Cortesio, M.A. Lokuta, A. Huttenlocher, D.J. Beebe, A platform for assessing chemotactic migration within a spatiotemporally defined 3D microenvironment, Lab on a Chip, 8 (2008) 1507-1515.

[140] H.C. Berg, *E. coli* in motion, Springer-Verlag, 2003.

[141] W.H. Press, B.P. Flannery, S.A. Teukolsk, W.T. Vetterling, Numerical Recipes in C: The Art of Scientific Computing, Cambridge University Press, Cambridge, 1992.

[142] D.A. Brown, H.C. Berg, Temporal stimulation of chemotaxis in *Escherichia coli*, Proceedings of the National Academy of Sciences of the United States of America, 71 (1974) 1388-1392.

[143] J. Adler, Hazelbau.Gl, M.M. Dahl, Chemotaxis toward sugars in *Escherichia coli*, Journal of Bacteriology, 115 (1973) 824-847.

[144] W. Saadi, S.W. Rhee, F. Lin, B. Vahidi, B.G. Chung, N.L. Jeon, Generation of stable concentration gradients in 2D and 3D environments using a microfluidic ladder chamber, Biomedical Microdevices, 9 (2007) 627-635.

[145] T. Kim, M. Pinelis, M.M. Maharbiz, Generating steep, shear-free gradients of small molecules for cell culture, Biomedical Microdevices, 11 (2009) 65-73.

[146] L. Goentoro, O. Shoval, M.W. Kirschner, U. Alon, The incoherent feedforward loop can provide fold-change detection in gene regulation, Mol Cell, 36 (2009) 894-899.

[147] C. Cohen-Saidon, A.A. Cohen, A. Sigal, Y. Liron, U. Alon, Dynamics and variability of ERK2 response to EGF in individual living cells, Mol Cell, 36 (2009) 885-893.

[148] J.R. Seymour, T. Ahmed, W.M. Durham, R. Stocker, Chemotactic response of marine bacteria to the extracellular products of Synechococcus and Prochlorococcus, Aquatic Microbial Ecology, 59 (2010) 161-168.

[149] J.T. Lehman, D. Scavia, Microscale nutrient patches produced by zooplankton, Proceedings of the National Academy of Sciences of the United States of America, 79 (1982) 5001-5005.

[150] J.G. Mitchell, A. Okubo, J.A. Fuhrman, Microzones surrounding phytoplankton form the basis for a stratified marine microbial ecosystem, Nature, 316 (1985) 58-59.

[151] T. Kiorboe, G.A. Jackson, Marine snow, organic solute plumes, and optimal chemosensory behavior of bacteria, Limnology and Oceanography, 46 (2001) 1309-1318.

[152] L. Goentoro, M.W. Kirschner, Evidence that fold-change, and not absolute level, of beta-catenin dictates Wnt signaling, Mol Cell, 36 (2009) 872-884.

[153] L.L. Rockwood, Introduction to Population Ecology, Wiley-Blackwell, 2006.

[154] G. Gause, Experimental studies on the struggle for existence. I. Mixed populations of two species of yeast., Journal of Experimental Biology, 9 (1932) 399-402.

[155] C.B. Huffaker, Experimental studies on predation: dispersion factors and predator-prey oscillations, Hilgardia, 27 (1958) 343-383.

[156] R. Gols, T. Bukovinszky, L. Hemerik, J.A. Harvey, J.C. Van Lenteren, L.E.M. Vet, Reduced foraging efficiency of a parasitoid under habitat complexity: implications for population stability and species coexistence, Journal of Animal Ecology, 74 (2005) 1059-1068.

[157] I.A. Hanski, M.E. Gilpin, Metapopulation Biology: Ecology, Genetics and Evolution, Academic, San Diego, 1997.

[158] D. Tilman, P. Kareiva, Spatial ecology: the role of space in population dynamics and interspecific interactions, Princeton University Press, Princeton, 1997.

[159] S.A. Levin, B. Grenfell, A. Hastings, A.S. Perelson, Mathematical and computational challenges in population biology and ecosystems science, Science, 275 (1997) 334-343.

[160] R. Levins, Extinction, Lectures on Mathematics in the Life Sciences, Vol. 2. Some Mathematical Questions in Biology (1970) 75-107.

[161] R. Levins, Some demographic and genetic consequences of environmental heterogeneity for biological control, Bulletin of the Entomological Society of America, 15 (1969) 237-240.

[162] S. Harrison, Local extinction in a metapopulation context - an empirical-evaluation, Biological Journal of the Linnean Society, 42 (1991) 73-88.

[163] I. Hanski, Habitat connectivity, habitat continuity, and metapopulations in dynamic landscapes, Oikos, 87 (1999) 209-219.

[164] J.H. Brown, A. Kodric-Brown, Turnover rates in insular biogeography - effect of immigration on extinction, Ecology, 58 (1977) 445-449.

[165] R.D. Holt, M.P. Hassell, Environmental heterogeneity and the stability of host parasitoid interactions, Journal of Animal Ecology, 62 (1993) 89-100.

[166] R.D. Holt, Ecology at the mesoscale: The influence of regional processes on local communities, Species diversity in ecological communities: Historical and geographical perspectives, (1993) 77-88.

[167] J. Bascompte, R.V. Sole, Effects of habitat destruction in a prey-predator metapopulation model, Journal of Theoretical Biology, 195 (1998) 383-393.

[168] M. Bevers, C.H. Flather, Numerically exploring habitat fragmentation effects on populations using cell-based coupled map lattices, Theoretical Population Biology, 55 (1999) 61-76.

[169] D. Tilman, Competition and biodiversity in spatially structured habitats, Ecology, 75 (1994) 2-16.

[170] G.R. Huxel, A. Hastings, Population size dependence, competitive coexistence and habitat destruction, Journal of Animal Ecology, 67 (1998) 446-453.

[171] E.J. Maly, Stability of interaction between Didinium and Paramecium - effects of dispersal and predator time lag, Ecology, 59 (1978) 733-741.

[172] C.B. Huffaker, S.G. Herman, K.P. Shea, Experimental studies on predation, complex dispersion and levels of food in an acarine predator-prey interaction, Berkeley, University of California, 1963.

[173] J.D. Reeve, Environmental variability, migration, and persistence in host-parasitoid systems, American Naturalist, 132 (1988) 810-836.

147

[174] J.T. Cronin, J.D. Reeve, Host-parasitoid spatial ecology: a plea for a landscape-level synthesis, Proceedings of the Royal Society B-Biological Sciences, 272 (2005) 2225-2235.

[175] M.B. Bonsall, D.R. French, M.P. Hassell, Metapopulation structures affect persistence of predator-prey interactions, Journal of Animal Ecology, 71 (2002) 1075-1084.

[176] G. Nachman, Systems-analysis of acarine predator prey interactions. 2. The role of spatial processes in system stability, Journal of Animal Ecology, 56 (1987) 267-281.

[177] G. Nachman, Systems analysis of acarine predator prey interactions.1. A stochastic simulation-model of spatial processes, Journal of Animal Ecology, 56 (1987) 247-265.

[178] M. Holyoak, Habitat subdivision causes changes in food web structure, Ecology Letters, 3 (2000) 509-515.

[179] M. Holyoak, S.P. Lawler, The role of dispersal in predator-prey metapopulation dynamics, Journal of Animal Ecology, 65 (1996) 640-652.

[180] A.B. Amezcua, M. Holyoak, Empirical evidence for predator-prey source-sink dynamics, Ecology, 81 (2000) 3087-3098.

[181] I. Hanski, Metapopulation dynamics, Nature, 396 (1998) 41-49.

[182] T.V. Burkey, Metapopulation extinction in fragmented landscapes: Using bacteria and protozoa communities as model ecosystems, American Naturalist, 150 (1997) 568-591.

[183] P. Kareiva, Habitat fragmentation and the stability of predator prey interactions, Nature, 326 (1987) 388-390.

[184] E. McCauley, R.M. Nisbet, W.W. Murdoch, A.M. de Roos, W.S.C. Gurney, Large-amplitude cycles of Daphnia and its algal prey in enriched environments, Nature, 402 (1999) 653-656.

[185] V.A.A. Jansen, The dynamics of two diffusively coupled predator-prey populations, Theoretical Population Biology, 59 (2001) 119-131.

[186] P.H. Crowley, Dispersal and the stability of predator-prey interactions, American Naturalist, 118 (1981) 673-701.

[187] F.R. Adler, Migration alone can produce persistence of host-parasitoid models, American Naturalist, 141 (1993) 642-650.

[188] G.W. Salt, Density, starvation, and swimming rate in Didinium populations, American Naturalist, 113 (1979) 135-143.

[189] C.B. Huffaker, Experimental studies on predation: Complex dispersion and levels of food in an acarine predator-prey interaction, 1963.

[190] M. Holyoak, Habitat patch arrangement and metapopulation persistence of predators and prey, American Naturalist, 156 (2000) 378-389.

[191] R. Nathan, W.M. Getz, E. Revilla, M. Holyoak, R. Kadmon, D. Saltz, P.E. Smouse, A movement ecology paradigm for unifying organismal movement research, Proceedings of the National Academy of Sciences of the United States of America, 105 (2008) 19052-19059.

[192] C.M. Jessup, S.E. Forde, B.J.M. Bohannan, Microbial experimental systems in ecology, Advances in Ecological Research, Vol. 37: Population Dynamics and Laboratory Ecology, 37 (2005) 273-307.

[193] C.M. Jessup, R. Kassen, S.E. Forde, B. Kerr, A. Buckling, P.B. Rainey, B.J.M. Bohannan, Big questions, small worlds: microbial model systems in ecology, Trends in Ecology & Evolution, 19 (2004) 189-197.

[194] T.G. Benton, M. Solan, J.M.J. Travis, S.M. Sait, Microcosm experiments can inform global ecological problems, Trends in Ecology & Evolution, 22 (2007) 516-521.

[195] B.J.M. Bohannan, R.E. Lenski, The relative importance of competition and predation varies with productivity in a model community, American Naturalist, 156 (2000) 329-340.

[196] J.H. Lawton, W.J. Resetarits, Jr., J. Bernardo, Ecological experiments with model systems: The Ecotron Facility in context, Experimental ecology: Issues and perspectives, (1998) 170-182.

[197] S. Park, P.M. Wolanin, E.A. Yuzbashyan, P. Silberzan, J.B. Stock, R.H. Austin, Motion to form a quorum, Science, 301 (2003) 188-188.

[198] H.J. Cho, H. Jonsson, K. Campbell, P. Melke, J.W. Williams, B. Jedynak, A.M. Stevens, A. Groisman, A. Levchenko, Self-organization in high-density bacterial colonies: Efficient crowd control, Plos Biology, 5 (2007) 2614-2623.

[199] W. Wang, L.M. Shor, E.J. LeBoeuf, J.P. Wikswo, D.S. Kosson, Mobility of protozoa through narrow channels, Applied and Environmental Microbiology, 71 (2005) 4628-4637.

[200] J.E. Keymer, P. Galajda, C. Muldoon, S. Park, R.H. Austin, Bacterial metapopulations in nanofabricated landscapes, Proceedings of the National Academy of Sciences of the United States of America, 103 (2006) 17290-17295.

[201] J.E. Keymer, P. Galajda, G. Lambert, D. Liao, R.H. Austin, Computation of mutual fitness by competing bacteria, Proceedings of the National Academy of Sciences of the United States of America, 105 (2008) 20269-20273.

[202] H.J. Kim, J.Q. Boedicker, J.W. Choi, R.F. Ismagilov, Defined spatial structure stabilizes a synthetic multispecies bacterial community, Proceedings of the National Academy of Sciences of the United States of America, 105 (2008) 18188-18193.

[203] D.A. Ratnam, S. Pavlou, A.G. Fredrickson, Effects of attachment of bacteria to chemostat walls in a microbial predator-prey relationship, Biotechnology and Bioengineering, 24 (1982) 2675-2694.

[204] J.L. Jost, J.F. Drake, Fredrick.Ag, H.M. Tsuchiya, Interaction of *Tetrahymena pyriformis*, *Escherichia coli*, *Azotobacter vinelandii* and glucose in a minimal medium, Journal of Bacteriology, 113 (1973) 834-840.

[205] S.T. Swift, I.Y. Najita, K. Ohtaguchi, A.G. Fredrickson, Continuous culture of the ciliate *Tetrahymena pyriformis* on *Escherichia coli*, Biotechnology and Bioengineering, 24 (1982) 1953-1964.

[206] J.S. Jaworska, T.G. Hallam, T.W. Schultz, A community model of ciliate *Tetrahymena* and bacteria *E. coli*:1. Individual-based models of *Tetrahymena* and *E. coli* populations, Bulletin of Mathematical Biology, 58 (1996) 247-264.

[207] A.M. Elliot, Biology of Tetrahymena, Dowden, Hutchinson & Ross, 1973.

[208] P.J. Watson, K. Ohtaguchi, A.G. Fredrickson, Kinetics of growth of the ciliate *Tetrahymena pyriformis* on *Escherichia coli*, Journal of General Microbiology, 122 (1981) 323-333.

[209] M. Habte, M. Alexander, Mechanisms of persistence of low numbers of bacteria preyed upon by protozoa, Soil Biology & Biochemistry, 10 (1978) 1-6.

[210] A.M. Elliot, Life cycle and distribution of Tetrahymena, in: A.M. Elliot (Ed.) Biology of Tetrahymena, Dowden, Hutchinson and Ross, 1973.

[211] J.O. Corliss, History, taxonomy, ecology and evolution of species of Tetrahymena, in: A.M. Elliot (Ed.) Biology of Tetrahymena, Dowden, Hutchinson and Ross, 1973, pp. 1-55.

[212] M.R. Levy, Effects of some environmental factors on the biochemistry, physiology and metabolism of Tetrahymena, in: A.M. Elliot (Ed.) Biology of Tetrahymena, Dowden, Hutchinson and Ross, 1973, pp. 227258.

[213] I.L. Cameron, Growth characteristics of Tetrahymena, in: A.M. Elliot (Ed.) Biology of Tetrahymena, Dowden, Hutchinson and Ross, 1973, pp. 199-257.

[214] M.P. Sauvant, D. Pepin, E. Piccinni, *Tetrahymena pyriformis*: A tool for toxicological studies, Chemosphere, 38 (1999) 1631-1669.

[215] S.W. Nam, D. van Noort, Y. Yang, S.H. Kim, S. Park, Use of a microvalve-controlled microfluidic device in a chemotaxis assay of *Tetrahymena pyriformis* in response to amino acids released from bacteria, Biochip Journal, 1 (2007) 111-116.

[216] C. Hatzis, F. Srienc, A.G. Fredrickson, Feeding heterogeneity in ciliate populations - effects of culture age and nutritional state, Biotechnology and Bioengineering, 43 (1994) 371-380.

[217] C.R. Curds, A. Cockburn, Studies of the growth and feeding of *Tetrahymena pyriformis* in axenic and monoxenic culture *Klebsiella aerogenes*, Journal of General Microbiology, 54 (1969) 343-358.

[218] J.L. Ingraham, Growth of psychrophilic bacteria, Journal of Bacteriology, 76 (1958) 75-80.

[219] A.D. Taylor, Metapopulations, dispersal, and predator prey dynamics - an overview, Ecology, 71 (1990) 429-433.

[220] S.L. Lima, P.A. Zollner, Towards a behavioral ecology of ecological landscapes, Trends in Ecology & Evolution, 11 (1996) 131-135.

[221] J.T. Locsei, Persistence of direction increases the drift velocity of run and tumble chemotaxis, Journal of Mathematical Biology, 55 (2007) 41-60.

[222] C.J. Morton-Firth, T.S. Shimizu, D. Bray, A free-energy-based stochastic simulation of the Tar receptor complex, Journal of Molecular Biology, 286 (1999) 1059-1074.

[223] T.S. Shimizu, S.V. Aksenov, D. Bray, A spatially extended stochastic model of the bacterial chemotaxis signalling pathway, Journal of Molecular Biology, 329 (2003) 291-309.

[224] J. Monod, J. Wyman, J.P. Changeux, On nature of allosteric transitions - a plausible model, Journal of Molecular Biology, 12 (1965) 88-118.

151